You have downloaded a document from
RE-BUŚ
repository of the University of Silesia in Katowice

Title: Niobium and tantalum oxides as model materials for resistive switching effect

Author: Anna Nowak

Citation style: Nowak Anna. (2019). Niobium and tantalum oxides as model materials for resistive switching effect. Praca doktorska. Katowice : Uniwersytet Śląski

© Korzystanie z tego materiału jest możliwe zgodnie z właściwymi przepisami o dozwolonym użytku lub o innych wyjątkach przewidzianych w przepisach prawa, a korzystanie w szerszym zakresie wymaga uzyskania zgody uprawnionego.

UNIWERSYTET ŚLĄSKI
W KATOWICACH

Biblioteka
Uniwersytetu Śląskiego

Ministerstwo Nauki
i Szkolnictwa Wyższego

Niobium and tantalum oxides as model materials for resistive switching effect

ANNA NOWAK

A.Chełkowki Institute of Physics, Department of Solid State Physics,
University of Silesia

A thesis submitted for the degree of

Doctor of Philosophy

Work done under the supervision of:

prof. dr hab. Jacek Szade and prof. dr hab. Krzysztof Szot

Chorzów, January 2019

“Ineffable difficult is to create something that is new, but it consists of everything we knew before.”

Richard Feynman

„Niewymowną trudnością jest tworzenie czegoś, co jest nowe, ale składa się z wszystkiego, co wiedzieliśmy wcześniej. “

Richard Feynman

Abstract

The aim of modern science is to find new solutions for a changing world. One current challenge for scientists face is to identify new materials for non-volatile memory with high recording density on a nanoscale, which will allow recording much more data than is presently possible. Transition metal oxides seem to be the most suitable materials for this purpose. Modifications of their properties which are necessary for recording data are based on redox reactions which can lead to changes of the resistance under the influence of an applied electric field. However, knowledge of the physical basis of this phenomenon which is often called resistive switching is still limited. The lack of a full explanation of the nature of resistive switching causes its application in electronic devices to still be problematic.

This Ph.D. thesis is devoted to transition metal oxides, i.e. niobium and tantalum oxides. Although it is often emphasized in literature that these materials have been studied for many years and knowledge of them seems to be complete, there still remain hidden areas where these materials may surprise us. This work is divided into two parts. The first part is dedicated to the single crystal of Nb_2O_5, while the second focuses on the thin films of Nb-O and Ta-O. The study concentrates on the fundamental physical and chemical properties of the material before and after thermal reduction. These experiments have shown that the effect of reducing conditions on a single crystal of Nb_2O_5 is limited to temperatures as high as 800 - 1000°C. Other behavior was observed for amorphous thin films of Nb-O or Ta-O systems which had a complex internal with pentoxides layers in the most external part of the films in the Nb-O system or in the bulk of the film as it was for Ta-O. Our results showed that for the film of Nb-O, thermal reduction in vacuum at temperatures as low as 300°C was enough to start the process of Nb valence changes while for the Ta-O system it started at about 600°C. Moreover, this process caused significant variation of the local conductivity of thin films due to the formation of NbO_2 and Ta_2O on their surface. We observed a bipolar type of switching and high dynamics of resistance for both types of films. On the other hand, conductivity of the Nb_2O_5 single crystal surface appeared to be much lower even after reduction in-situ at 600°C, however, it was possible to modify it with the use of an electrically biased atomic force microscope tip which opens the way to record information.

The presented results of the studies of transition metal oxides (Nb,Ta) in single crystal and thin film forms have permitted gaining new knowledge particularly concerning the relation between chemical and structural instability of the studied oxides with other properties. This especially surrounds knowledge about conductivity, which can be locally controlled and its relation to structure and thermal history, permits more straightforward application of these materials.

Streszczenie

Celem współczesnej nauki jest znalezienie nowych rozwiązań dla wciąż zmieniającego się świata. Jednym z wyzwań jakie stawiają sobie naukowcy jest znalezienie nowego materiału dla pamięci nieulotnych o dużej gęstości zapisu, który w coraz to mniejszej scali, nanoskali, pozwoli na zapisanie coraz większej ilości danych. Takimi materiałami mogą być tlenki metali przejściowych, które bazując na reakcji redoks, wykazują zdolność do zmiany oporu pod wpływem przyłożonego pola elektrycznego. Jednakże wiedza o fizycznych podstawach tego zjawiska jest wciąż ograniczona. Do tej pory nie zostało jasno i klarownie przedstawione wyjaśnienie natury zjawiska przełączania rezystywnego, a co za tym idzie jego aplikacja w urządzeniach elektronicznych, może być nadal problematyczna.

Niniejsza praca doktorska została poświęcona tlenkom metali przejściowych jakim są tlenki niobu i tantalu. Chociaż jak się często podkreśla są to materiały wciąż badane od wielu lat i wydaje się, że posiadamy już duży zasób wiedzy na ich temat, to nadal są miejsca, gdzie materiały te potrafią nas zaskoczyć. Praca ta została podzielona na dwie części. Pierwsza została poświęcona monokryształowi Nb_2O_5 natomiast w drugiej badania były skoncentrowane na cienkich warstwach Nb-O i Ta-O. W pracy przedstawiono wyniki badań podstawowych właściwości fizyko-chemicznych materiału przed oraz po redukcji termicznej. Temperatury od 800°C -1000°C znacząco redukują monokryształ Nb_2O_5. Natomiast w cienkich warstwach amorficznych Nb-O czy Ta-O o złożonej strukturze wewnętrznej, w której skład wchodzą warstwy pięciotlenków, zaobserwowano ten efekt w znacznie niższych temperaturach. Nawet niewielka zmiana temperatury (300°C dla Nb-O i 600°C dla Ta-O) wpływa na stopień redukcji warstwy. Wpływ temperatury ma również silenie znaczenia na przewodnictwo. W cienkich warstwach zaobserwowano przełączanie oporności typu bipolarnego. Natomiast w krysztale ten sam efekt również był zauważalny, lecz znacznie słabszy. Można było, podobnie jak w cienkich warstwach, zmodyfikować jego powierzchnie w celu zapisania informacji przy pomocy igły z mikroskopu sił atomowych.

Reasumując przedstawione wyniki badań w tej pracy pozwalają w szerszy sposób spojrzeć na problem chemicznej i strukturalnej niestabilności tlenków metali przejściowych (Nb, Ta) w krysztale jak i cienkich warstwach. Pokazują wpływ tych zmian na ich przewodnictwo, które może być lokalnie kontrolowane, pozwalając na łatwiejszą aplikacje tych materiałów.

Acknowledgements

This dissertation would never have been published if it had not been for two wonderful people who showed me how interesting oxide materials could be.

First, I would like to express my deepest gratitude to Professor Jacek Szade who allowed me to become a part of his research team and showed me how fun work as a researcher can be. Thanks to this, I had the opportunity not only to solve the research questions and problems of assisted transition metal oxide, but also to participate in many new and interesting studies, not only related with nanotechnology, but find answers to questions related to the 'real' world. Thank you for all the long hours spent on scientific discussion, for your help and all your valuable advice and comments and thank you for allowing me to spread my wings.

I want to thank Professor Krzysztof Szot for the idea and the opportunity to explore the highly interesting, yet not fully explained behaviors of transition metals oxides such as niobium and tantalum. I would also like to thank you for each and every conversation and the many valuable comments and good advice.

I am also grateful to Jörg Perßon and Sebastian Schmelzer who took the time and their experience to grow the single crystal and thin films, without this samples, my thesis would never be born.

I would also like to express my gratitude to Professor Alain Bulou and Professor Gwenel Corbel for their time, advice and discussions during my internship at University du Main, Le Mans, France.

At this point I would like to emphasize that my life would not be so wonderful and would not bring me so much joy if it were not for my friends. After my Ph.D. studies, I met wonderful people and experienced wonderful moments, besides those in the laboratory. If it had not been for your support, long conversations, and time spent together, this time would not have brought me so much satisfaction and the experience of many wonderful moments. Thank you for everything, please do not change! In particular I would like to thank Dr. Katarzyna Balin, who was my guide as I meandered through the vacuum techniques while she patiently and persistently showed and explained where my mistakes were made and how to correct them. I would also like to thank Dr. Mateusz Dulski for pointing the way and showing how fascinating crystal vibrations can be and how much news they carry. Thank you, for all your support and every word of 'don't give up'. The last thanks goes to Dr Marcin

Wojtyniak for spending long hours with me at the microscope and consistently answering the 'wise' questions that came to my mind.

Finally, I would like to thank all employees of the Institute of Physics, for whom I could always count on for their help.

Special thanks belong to the support given to me by three scholarship programs: TWING, DoktoRIS and PIN funded by the European Union through the European Social Funds (ESF)

This work would not have been so easy nor such a fantastic adventure if it had not been for the heartfelt support of my parents. Thank you for listening to my complaints each day, always supporting me with good advice and for not letting me stray off my chosen path.

Contents

1. Introduction ... *1*

2. Fundamentals ... *4*

2.1 Crystal growth ... **5**

2.2 Thin film preparation by sputtering technique ... **8**

2.3 Niobium - oxygen system ... **9**

2.3.1 Niobium monoxide (NbO) ... 10
2.3.2 Niobium dioxide (NbO_2) ... 10
2.3.3 Niobium pentoxide (Nb_2O_5) ... 11
2.3.4 Other niobium oxides ... 13

2.4 Electronic structure of Nb-O system ... **14**

2.5 Tantalum – oxide system ... **18**

2.5.1 Tantalum dioxide ... 19
2.5.2 Tantalum pentoxide ... 19
2.5.3 Other Tantalum oxides ... 22

2.6 Electronic structure of Ta-O system ... **22**

2.7 Defects in the Nb-O and Ta-O system ... **26**

2.7.1 Point defects ... 26
2.7.2 One-dimension defects ... 29
2.7.3 Two- dimensional defects ... 30

2.8 Electronic transport ... **33**

2.8.1 Electronic transport in niobium oxides ... 33
2.8.2 Electronic transport in tantalum oxides ... 35

2.9 Resistive switching ... **36**

2.9.1 Resistive switching in Nb-O system ... 38
2.9.2 Resistivity switching in the Ta-O system ... 41

2.10 Application of Nb-O and Ta-O systems ... **42**

3. Experimental methods ... *43*

3.1 X-ray photoemission spectroscopy ... **43**

3.2 X-ray diffraction method ... **45**

3.3 X-ray reflectivity method ... **46**

3.4 Atomic Force Microscopy ... **49**

3.5 Raman spectroscopy ... **53**

3.6 Time of flight secondary ion mass spectroscopy ... **55**

4. Results and discussion ... *57*

4.1 Basic properties of Nb_2O_5 single crystals ... **57**

4.1.1 Crystallographic structure ... 57
4.1.2 Raman spectroscopy ... 64
4.1.3 Surface composition and electronic structure ... 75
4.1.4 LC-AFM measurements ... 78

4.2 Niobium and tantalum oxide thin film ... **84**

4.2.1 Nb-O thin film basic properties ... 84
4.2.2 Tantalum – oxide system ... 96

5. Conclusions ... *108*

Bibliography ... *111*

List of Figures

FIGURE 1.1 SCHEME OF INVESTIGATION OF NIOBIUM AND TANTALUM OXIDES 3
FIGURE 2.1 PHASE DIAGRAM OF NB-O SYSTEM 4
FIGURE 2.2 SCHEME OF VERNEUIL PROCESS 5
FIGURE 2.3 SCHEMATIC DIAGRAM OF A VERTICAL BRIDGMAN (VB) CRYSTAL GROWTH PROCESS IN A SINGLE-ZONE FURNACE (A) AT THE BEGINNING OF THE EXPERIMENT AND (B) WITH PARTIALLY GROWN CRYSTAL 6
FIGURE 2.4 SCHEMATIC DRAWING OF THE OPTICAL FLOATING ZONE. (17) 7
FIGURE 2.5 DIAGRAM OF RF- SPUTTERING PROCESS (ADAPTED FROM (21)) 8
FIGURE 2.6 THE NIOBIUM-OXYGEN SYSTEM: MAIN OXIDES AND SOME OF THEIR STRUCTURAL AND ELECTRICAL PROPERTIES (CONDUCTIVITY Σ GIVEN AT ~ 0°-25°C) AS A FUNCTION OF THE FORMAL NB- OXIDATION STATE (ADAPTED FROM (24)) 9
FIGURE 2.7 TEMPERATURE MODIFICATION OF NB_2O_5 (ADAPTED FROM (36)) 13
FIGURE 2.8 MOLECULAR ORBITALS (MO) DIAGRAMS IN SPIN-RESTRICTED (LEFT) SPIN- POLARIZED (CENTER) SELF-CONSISTENT AND (RIGHT) CALCULATION WITH USE OF DISCRETE VARIATIONAL METHOD (DVM) OF NBO_6^{10-} CLUSTER (ADAPTED FROM (55)) 14
FIGURE 2.9 TOTAL AND PARTIAL DOS OF (A) NBO_2 AND (B) NB_2O_5. THE THIRD PANE FROM THE TOP PRESENTS COMPARISON OF EXPERIMENTAL (DOTS) AND DOS CALCULATIONS (41). 15
FIGURE 2.10 THE ELECTRONIC BAND STRUCTURE FOR DIFFERENT NIOBIUM OXIDE: (A) NBO_2 (B) NB_2O_5 (56) 16
FIGURE 2.11 DOS CALCULATION OF (A) NB_2O_5 AND (B) NBO_2 (33) 17
FIGURE 2.12 CALCULATED DISPERSION RELATION ALONG THE HIGH SYMMETRY DIRECTIONS IN THE IRREDUCIBLE BRILLOUIN ZONE FOR (A) B-NB_2O_5 WITH PBESOL, (B) HSE06, AND B-TA_2O_5 WITH (C) PBESOL AND (D) HSE06 AND CALCULATED TOTAL AND SITE-PROJECTED DOS FOR B-NB2O5 WITH (A) PBESOL, (B) HSE06, AND B-TA_2O_5 WITH (C) PBESOL, (D) HSE06. THE BLACK LINES CORRESPOND TO TOTAL DOS; THE GREEN-SHADED AREAS CORRESPOND TO NB (TA) D-STATES, THE BLUE-SHADED AREAS, RED LINES AND CYAN LINES CORRESPOND TO O_1, O_2, AND O_3 P-STATES, RESPECTIVELY. THE ENERGY IS SHIFTED TO THE VBM. (57) 18
FIGURE 2.13 PHASE DIAGRAM OF TA-O SYSTEM 18
FIGURE 2.14 REPRESENTATIVE POLYHEDRA CUT FROM SOME OF THE RELAXED CRYSTAL STRUCTURES OF TA_2O_5. (A) DISTORTED OCTAHEDRA TAO_6, (B) PENTAGONAL BIPYRAMID TAO_7, (C) HEXAGONAL BIPYRAMID TAO_8 AND (D) MONO-CAPPED TRIGONAL PRISM TAO_7. (69) 20
FIGURE 2.15 TEMPERATURE MODIFICATION OF TA_2O_5 20
FIGURE 2.16 PARTIAL DENSITY OF THE STATES OF TA AND O ATOMS CLOSET TO THE VACANCY. SOLID CURVE IS MARKED IDEAL Δ- TA_2O_5; DASHED CURVE Δ- TA_2O_5 WITH OXYGEN VACANCY. ADAPTED FROM (83) 23
FIGURE 2.17 BAND STRUCTURE OF Δ-TA_2O_5 ALONG A FEW HIGH SYMMETRY DIRECTIONS IN THE IRREDUCIBLE BRILLOUIN ZONE. (83) 24
FIGURE 2.18 CALCULATED DISPERSION RELATION ALONG THE HIGH SYMMETRY DIRECTIONS OF THE IRREDUCIBLE BRILLOUIN ZONE FOR Λ-TA2O5 WITH (A) PBESOL (B) HSEO6 WITH (C) PBESOL (D) HSEO6 FOR B-TA_2O_5. THE DATA WAS ADAPTED FROM (84) 25
FIGURE 2.19 CLASSIFICATION OF DEFECTS. - CLASSIFICATION OF DEFECTS BASED ON THE TOPOLOGICAL CRITERIA. THE POINT DEFECTS ARE CONSIDERED ZERO-DIMENSIONAL (6) 26
FIGURE 2.20 SCHEMATIC TWO-DIMENSIONAL REPRESENTATION OF SOME OF THE DEFECTS PRESENT IN A SOLID OF THIS TYPE METAL OXIDE(88) 29
FIGURE 2.21 SIMPLIFIED REPRESENTATION OF (A) AN EDGE DISLOCATION WITH $\ell \perp B$ AND (B) A SCREW DISLOCATION WITH $\ell \| B$. (88) 30
FIGURE 2.22 IN CONTRAST TO TIO_2 THE ACCUMULATION OF OXIDASE VACANCIES FOR NB_2O_5 HAVE BEEN OBSERVED IN THREE ORTHOGONAL DIRECTIONS. ALONG THE PLANE IN THREE ORTHOGONAL DIRECTIONS MEANS THESE PLANAR DEFECTS (WADSLEY DEFECTS) UPPER CROSSING, TOGETHER CREATE A BLOCK STRUCTURE. 31
FIGURE 2.23 TWO-DIMENSIONAL LATTICE IMAGE SHOWING AN INTERACTION BETWEEN THE DEFECT OF A AND C (44) 31
FIGURE 2.24 TWO-DIMENSIONAL LATTICE IMAGE OF H-NB_2O_5 SHOWING THE DEFECT OF TYPE A PARALLEL TO THE C AXIS. INSERT CORRESPOND TO THE ENCLOSED AREA. (44) 32
FIGURE 2.25 HIGH-MAGNIFICATION LATTICE IMAGE SHOWING THE $NB_{12}O_{29}$-TYPE WADSLEY DEFECT (INDICATED BY ARROW). SOME OF THE TETRAHEDRAL SITES SHOW DARKER CONTRAST THAN OTHERS, SUGGESTING METAL-ATOM VACANCIES (97). 32

FIGURE 2.26 AN ORDERED INTERGROWTH O THE $NB_{29}O_{62}$ –TYPE WADSLEY DEFECTS (INDICATED BY ARROWS) INTO THE HOST STRUCTURE. THE REGION FORMS A SUPERSTRUCTURE HAVING A COMPOSITION OF $NB_{47}O_{116}$. THE UNIT CELL IS OUTLINED. (97) 32
FIGURE 2.27 THE LOGARITHMIC OF ELECTRICAL RESISTANCE OF A-NB_2O_5 AS A FUNCTION OF RECIPROCAL TEMPERATURE (A) AT 1ATM ($pO2 - 1/4$ REGION); (B) $pO2 = 10 - 13\ atm$ ($pO2 - 1/6$ REGION) (92) 33
FIGURE 2.28 FOUR PROBE CONDUCTIVITY DATA ON NBO_2 (29) 34
FIGURE 2.29 TEMPERATURE DEPENDENCE OF ELECTRON DRIFT MOBILITY FOR A-NB_2O_5 AT $pO2 = 10 - 13\ atm$ (92) 34
FIGURE 2.30 RESISTIVITY AS A FUNCTION OF TEMPERATURE FOR CURRENT PARALLEL TO THE CRYSTALLOGRAPHIC AXIS A AND C (PROJECTION OF STRUCTURE LEFT CORNER OF PICTURE) (100). 35
FIGURE 2.31 SEEBECK COEFFICIENT OBTAINED IN VARIOUS OXYGEN PRESSURES AT $968°C, 1000°C, 1240°C$ (102) 36
FIGURE 2.32 TWO BASIC TYPE OF RESISTIVITY SWITCHING PHENOMENA (A)BIPOLAR SWITCHING – THERE IS A DIFFERENCE IN POLARITY, THE SET VOLTAGE IS ONE POLARITY OF VOLTAGE WHILE RESET OPERATION REQUEST THE OPPOSITE POLARITY AND (B) UNIPOLAR SWITCHING – THERE IS NO DIFFERENCE IN POLARITY, THE SET VOLTAGE IS ALWAYS HIGHER THAN THE RESET (105) 37
FIGURE 2.33 THE PART OF SRTIO3 SINGLE CRYSTAL. ADAPTED FROM SZOT ET AL.(3). 38
FIGURE 2.34 SUMMARY OF THE RESISTIVE SWITCHING MECHANISM. CLASSIFICATION OF THE MOST COMMON RS DRIVING MECHANISM. THE CLASSES IN THE CENTER ARE ESPECIALLY INTERESTING, SINCE THOSE ARE RELATED TO THE REDOX CHEMICAL EFFECT (105) 38
FIGURE 2.35 TWO TYPES OF CONDUCTIVE PATHS RESPONSIBLE FOR RESISTIVITY SWITCHING ACCORDING TO SAWA (12,104). LEFT FILAMENT TYPE, RIGHT INTERFACIAL TYPE(12,118) 39
FIGURE 3.1 PHOTOEXCITATION FROM THE ENERGY LEVEL. 43
FIGURE 3.2 SCHEMATIC OF THE XPS SPECTROMETER. ADAPTED FROM (12) 44
FIGURE 3.3 SCHEMATIC DIAGRAM OF THE DIFFRACTOMETER CONFIGURATION OF BRAGG—BRENTANO GEOMETRY USED IN PANALYTICAL DIFFRACTOMETER. SCHEMATIC ILLUSTRATION OF BRAGG LAW WHICH IS SHOWN MORE CLOSELY. 46
FIGURE 3.4 ILLUSTRATION OF THE PLANE OF INCIDENCE FOR A STRATIFIED MEDIUM 48
FIGURE 3.5 EXAMPLE OF TA_2O_5 THIN LAYER. THE BLUE LINE IS AN EXPERIMENTAL RESULT AND THE RED ONE IS DERIVED FROM THE CALCULATION. 49
FIGURE 3.6 A SIMPLE SKETCH OF INTERACTION FORCE F AS A FUNCTION OF SEPARATION DISTANCE D BETWEEN THE TIP AND THE SPECIMEN. THE POSITIVE INTERACTION FORCE STANDS FOR A REPULSIVE FORCE PUSHING THE TIP AWAY FROM THE SAMPLE. THIS IMPOSES A POSITIVE DEFLECTION OF THE CANTILEVER IN A VERTICAL DIRECTION. A NEGATIVE INTEGRATION FORCE STANDS FOR ATTRACTIVE FORCE PULLING THE TIP TOWARDS THE SAMPLE, WHICH LEADS TO A NEGATIVE DEFLECTION OF THE CANTILEVER. THE SKETCH CAN BE DIVEDED INTO THREE ZONES ACCORDING TO THE PRESENTENCE OF ATTRACTIVE AND REPULSIVE FORCES. THE ATTRACTIVE FORCES PLAY CRUCIAL ROLE IN THE NON-CONTACT (DYNAMIC) OPERATION MODE. 50
FIGURE 3.7 THE SCHEME OF AFM MEASUREMENT ADAPTED FROM RODENBÜCHNER THESIS (12) 51
FIGURE 3.8 CONTACT (STATIC) OPERATION MODE 52
FIGURE 3.9 NON-CONTACT (DYNAMIC) OPERATION MODE 52
FIGURE 3.10 TAPPING OPERATION MODE 53
FIGURE 3.11 CRYSTAL ORIENTED AMONG THE (001) (MAIN AXIS) INVESTIGATED BY RAMAN. THE GREEN DOT SHOWS WHERE THE LASER BEAM WAS ON THE CRYSTAL. 54
FIGURE 3.12 SCHEMATIC IDENTIFYING LIGHT SCATTERING AFTER LASER EXPOSURE ON A SAMPLE SURFACE. PHOTONS OF LIGHT ARE FOCUSED ON THE SAMPLE THROUGH THE MICROSCOPE OBJECTIVE AT A DEFINED MAGNIFICATION. WHEN THEY INTERACT WITH CHEMICAL BONDS WITHIN THE MATERIAL ELECTRONS ARE EXCITED TO VIRTUAL ENERGY LEVELS. THESE MOLECULES RETURN TO THE ORIGINAL ENERGY LEVEL BY EMITTING A PHOTON OF LIGHT, KNOWN AS ELASTIC OR RAYLEIGH SCATTERING, OR IT CAN UNDERGO AN ENERGY SHIFT AND RETURN AT LOWER (STOKES) OR HIGHER (ANTI-STOKES) ENERGY LEVELS, KNOWN AS RAMAN SCATTERING. RAMAN SCATTERING IS A LOW-PROBABILITY PROCESS WITH AROUND 1 IN 108 PHOTONS INELASTICALLY SCATTERED (ARROW WIDTHS ARE NOT REPRESENTATIVE); STOKES RAMAN SCATTERING IS MORE INTENSE THAN ANTI-STOKES SCATTERING BECAUSE OF THE INCREASED PROBABILITY OF A MOLECULE BEING IN THE GROUND VIBRATIONAL STATE. FLUORESCENCE CAN OCCUR WHEN ELECTRONS ARE EXCITED TO ELECTRONIC ENERGY LEVELS AND RETURN TO THE GROUND ENERGY LEVEL BY EMITTING A PHOTON OF LIGHT AT A LONGER WAVELENGTH. ADAPTED FROM 55
FIGURE 3.13 SCHEMATIC DIAGRAM OF TOF-SIMS INSTRUMENT. THE SURFACE BOMBARDED BY BI IONS GENERATE THE DIFFERENT TYPES OF SECONDARY IONS AND CLUSTER IONS. 56
FIGURE 4.1 STRUCTURE TWO OBTAINED FROM FITTING THE DIFFRACTION STUDIES COMPARED TO THE H-NB_2O_5 FROM LITERATURE (37). 58
FIGURE 4.2 THE LAUE DIFFRACTION PATTERN OF SINGLE CRYSTAL NB_2O_5 COLLECTED ON CRYSTAL AS-GROWN. 59
FIGURE 4.3 POWDER DIFFRACTION PATTERN OF THE PULVERIZED CRYSTAL IN THE BEFORE AND AFTER ANNEALING. THE DATA WERE COLLECTED IN BOTH CASES AT ROOM TEMPERATURE 60
FIGURE 4.4 TEMPERATURE DEPENDENCE OF THE CELL PARAMETERS OF H-NB_2O_5 POWDER PLACED IN AIR 60

Figure 4.5 Powder diffraction pattern of the pulverized crystal in diluated hydrogen before and after annealing. In both cases, the data were collected at room temperature. 62
Figure 4.6 Temperature dependence of the cell parameters of H-Nb_2O_5 powder placed in a diluted hydrogen environment........ 62
Figure 4.7 Difference between crystal non- and pulverized after reducing in H_2 and RH_4 atmosphere, respectively. 63
Figure 4.8 Crystal structure of a) H-Nb_2O_5 with various niobium-oxygen b) polyhedra: edge-shared $(NbO_6)_{ES}$ and corner-shared $(NbO_6)_{CS}$ octahedra as well as NbO_4 tetrahedra. Oxygen is marked as small red dots. 64
Figure 4.9 Acoustic mode presented in the 6Å part of H-Nb2O5 crystal oriented towards lattice parameter b 65
Figure 4.10 Polarized Raman spectra of the H-Nb_2O_5 single crystal oriented along the z-axis and rotated in the XY plane. The band fitting analysis were performed using Grams Software package. The different polyhedra were color-highlighted: dark gray means corner-shared, gray - slightly deformed edge-shared and light gray - highly distorted niobia octahedra. Acoustic modes were described by the red-arrow in the range below 100 cm^{-1} while the optical modes were illustrated in the 100 - 1100 cm^{-1} range. 68
Figure 4.11 Temperature-dependent in situ polarized Raman spectra of the H-Nb_2O_5 single crystal oriented along the z-axis and measured at z(xx)z polarization. The band fitting analysis were performed using Grams Software package. The different polyhedra were color-highlighted: dark gray means corner-shared, gray - slightly deformed edge-shared and light gray - highly distorted niobia octahedra. Acoustic and optical modes were described, respectively by red- and blue-arrows in the range below 100 $cm^{-1}$and in the 100 - 1100 cm^{-1} range. 70
Figure 4.12 The temperature evolution of the band position of a) terminal Nb=O, b) Nb–O–Nb bridging bond in NbO_6,and c,d) O-Nb-O bridging bond in NbO_6 for the H-Nb_2O_5phase. The data are presented for z(xx)z polarization. The expected behavior by theory of phonon anharmonicity are red-line highlighted. 73
Figure 4.13 Temperature evolution of the integral intensity of bands assigned to different niobia polyhedra a) terminal Nb=O, b) edge-shared $(NbO_6)_{ES}$ (620 - 680 cm^{-1}), c) corner-shared $(NbO_6)_{CS}$ (560 - 620 cm^{-1}) as well as d) correlation between integrated intensity analysis for niobia polyhedra presented in the form of the ratio: $(NbO_6)_{CS}$ / $(NbO_6)_{ES}$ (green line) and (O-Nb-O) / $(NbO_6)_{SD}$ (red line).The data are presented for z(xx)z polarization 74
Figure 4.14 Overview spectrum of H-Nb_2O_5 obtained in the room temperature........ 76
Figure 4.15 XPS selected temperature data for Nb3d and O1s lines 77
Figure 4.16 Temperature Valence Band dependence in the single crystal 77
Figure 4.17 The chemical composition as a function of reduction temperature in Nb_2O_5, the O/Nb and valences ratios. 78
Figure 4.18 Topography and local conductivity of cleaved H-Nb2O5 obtained at room temperature. 79
Figure 4.19 The following 1500x1500nm area were collected before the reduction process. The parament changes are observed on the crystal surface. The oxygen ion was extracted from the surface by the tip and the scan area was decomposed. 79
Figure 4.20 The ON/OFF state revealed by different voltage bias applied after crystal reduction at 600° C. The forming process was obtained for two different tips: diamond (above part of the figure) and Pt/Ir (bottom part of figure). 81
Figure 4.21 The topography and conductive map obtained at (a)25°C, (b)100°C and (c) 600°C reduction temperature. A diamond and Pt/Ir tip were used. The I-V curves were collected before and after annealing at room temperature (left and right corner, respectively). The forming process presented in the left corner start in the area of 1000x1000 nm with applying positive potential on the tip, then the area was reduced to 750x750nm and the applied potential was negative. The last area was 500x500nm and again the applied potential was negative. 82
Figure 4.22 Local conductivity map collected before and after annealing at the room temperature for the crystal. 83
Figure 4.23 Result for XRR data with electron density profile. 84
Figure 4.24 Result for fitting the XPS spectra for Nb-O thin film obtained for selected temperature. 86
Figure 4.25 Temperature dependence of the photoemission spectra for the Nb-O thin film: (a) Nb3d doublet (b) valence band (c) O1s and (d) oxygen and niobium ratio derived from XPS spetra. 87
Figure 4.26 Valence ratios as a function of reduction temperature in Nb-O thin film 87
Figure 4.27 Depth profile obtained in positive polarity. 90

FIGURE 4.28 DISTRIBUTION MAPS FOR SELECTED IONS MEASURED IN POSITIVE POLARITY FOR Nb_2O_5 FILM GROWN ON SI. THE GRAPH REPRESENTS THREE MAIN COLUMNS: (A) WHERE PROJECTION TYPE HAS BEEN SPECIFIED, (B) WITH RESPECTIVE PROJECTIONS OF PARTICULAR IONS, (C) 3D OVERLAY OF SELECTED IONS 91
FIGURE 4.29 DISTRIBUTION MAPS FOR SELECTED IONS MEASURED IN NEGATIVE POLARITY FOR Nb_2O_5 FILM GROWN ON SI. THE GRAPH REPRESENTS THREE MAIN COLUMNS: (A) WHERE PROJECTION TYPE HAS BEEN SPECIFIED, (B) WITH RESPECTIVE PROJECTIONS OF PARTICULAR IONS, (C) 3D OVERLAY OF SELECTED IONS. 92
FIGURE 4.30 DEPTH PROFILE OBTAINED FROM MEASUREMENTS IN NEGATIVE POLARITY; (A) PROFILE AS MEASURED, (B) PROFILE AFTER POINT BY POINT NORMALIZATION TO THE O^{2-} LINE. 93
FIGURE 4.31TOPOGRAPHY AND LOCAL CONDUCTIVITY MAP OBTAINED AT 300°C, 450°C AND 600°C. THE I-V CURVE WITH THE CONDUCTIVE AREA WITH DIFFERENT CURRENT LOAD. 95
FIGURE 4.32 THE PICTURE PRESENTS (A) CURRENT MAP, WHERE IN THE MIDDEL AREA ARE PRESENTED SWITCHED TO THE LOW RESISTANCE STATE (B). ROUGHNESS (RMS) OBTEINED FROM THE PICTURE MEASURED IN THE DIFFERENT TEMPERATURE RANGE. 95
FIGURE 4.33 POWDER DIFFRACTION RESULT FOR TA-O THIN FILM 97
FIGURE 4.34 RESULT FOR XRR DATA WITH ELECTRON DENSITY PROFILE. 97
FIGURE 4.35 RESULT FOR TA4F AND O1S LINE DERIVED FROM TA-O THIN FILM AFTER ANNEALING PROCESS UP TO 900° C 99
FIGURE 4.36 TEMPERATURE DEPENDENCE OF THE PHOTOEMISSION SPECTRA FOR THE TA-O THIN FILM: (A) TA4F DOUBLET (B) VALENCE BAND (C) O1S AND (D) OXYGEN AND TANTALUM RATIO DERIVED FROM XPS SPECTRA 100
FIGURE 4.37 VALENCE RATIO AS A FUNCTION OF REDUCTION OF THE TA-O THIN FILM 101
FIGURE 4.38 DISTRIBUTION MAPS FOR SELECTED IONS MEASURED IN POSITIVE POLARITY FOR Ta_2O_5 FILM GROWN ON SI. THE GRAPH REPRESENTS THREE MAIN COLUMNS: (A) WHERE PROJECTION TYPE HAS BEEN SPECIFIED, (B) WITH RESPECTIVE PROJECTIONS OF PARTICULAR IONS, (C) 3D OVERLAY OF SELECTED IONS 103
FIGURE 4.39 DISTRIBUTION MAPS FOR SELECTED IONS MEASURED IN NEGATIVE POLARITY FOR Ta_2O_5 FILM GROWN ON SI. THE GRAPH REPRESENTS THREE MAIN COLUMNS: (A) WHERE PROJECTION TYPE HAS BEEN SPECIFIED, (B) WITH RESPECTIVE PROJECTIONS OF PARTICULAR IONS, (C) 3D OVERLAY OF SELECTED IONS. 104
FIGURE 4.40 PROFILE OBTAINED FROM POSITIVE POLARITY FOR TA-O THIN FILM 105
FIGURE 4.41 DEPTH PROFILE OBTAINED FROM MEASUREMENTS IN NEGATIVE POLARITY; (A) PROFILE AS MEASURED, (B) PROFILE AFTER POINT BY POINT NORMALIZATION TO THE O^{2-} LINE. 106
FIGURE 4.42 AFM TOPOGRAPHY AND LOCAL CONDUCTIVITY (LC) MAPS OF THE TA-O FILM REDUCED AT 220°C FOR 8 HOURS; A) AFM CONTACT MODE TOPOGRAPHY WITH THE RANGE UP TO 1.76 NM; B) LC MAP OBTAINED WITH THE BIAS VOLTAGE OF 2 V, CURRENT RANGE WAS 1.8 TO 31.7 NA; C) I-V CURVE OBTAINED AT ONE OF THE LOW RESISTANCE POINTS; D) CURRENT MAP SHOWING IN THE MIDDLE THE AREA SWITCHED TO THE LOW RESISTANCE STATE, CURRENT RANGE 0.03 TO 1243.4 NA AT THE BIAS VOLTAGE OF 0.05 V. 107

List of Tables

TABLE 1 CRYSTAL STRUCTURE OF NB_2O_5 12
TABLE 2 CRYSTAL STRUCTURE OF TA_2O_5 21
TABLE 3 LEAKAGE CONDUCTION MECHANISMS IN METAL/OXIDE/METAL STRUCTURES WHERE J: CURRENT DENSITY, A^*: EFFECTIVE RICHARDSON CONSTANT, Φ_B: POTENTIAL BARRIER HEIGHT, E: ELECTRIC FIELD, E: ELECTRON CHARGE, ε_I: OXIDE PERMITTIVITY, D: OXIDE THICKNESS, ΔE_{AE}: ACTIVATION ENERGY OF ELECTRONS, $A \equiv E/(4\pi\varepsilon_I D)$. (122) 40
TABLE 4 THE RESULT FOR STRUCTURE REFINEMENT ON THE TWINNING STRUCTURE OF NB_2O_5 SINGLE CRYSTAL 59
TABLE 5 THE CELL PARAMETERS OBTAINED FROM RIETVELD REFINEMENT TO H-NB2O5 POWDER AFTER HEAT PROCESS IN AIR 61
TABLE 6 THE CELL PARAMETERS OBTAINED FROM RIETVELD REFINEMENT TO H-NB2O5 POWDER AFTER HEAT PROCESS IN DILUTED HYDROGEN. 61
TABLE 7 THE X-RAY REFLECTIVITY RESULT FOR NB-O THIN FILM 85
TABLE 8 THE X-RAY REFLECTIVITY RESULT FOR TA-O THIN FILM 98

1. Introduction

In an increasingly information dominated society, electronic devices have become an integral part of today's world and our daily lives. This trend has brought with it an increasing demand to make devices more efficient, more powerful and increasingly more miniaturized. Storage sizes of a GB or TB are no longer sufficient to meet consumer's demands and expectations related to devices' size, speed, flexibility and energy consumption. Modern silicon based technological solutions seem to have reached certain limitations which has brought about an intense search for new materials to satisfy this need. CMOS (Complementary metal-oxide-semiconductor) technology now requires both a larger capacity and smaller size of MOSFET's (p-type and n-type metal oxide semiconductor field effect transistors). However, below 22nm MOSFET transistors suffer from severe leakage of current and dynamic power. Hence, the new kinds of materials to be searched for must be compatible with silicon technology and capable of writing information on 2 nm x 2 nm areas.

In line with Moor's law, doubling the number of transistors placed on a single square inch of an integrated circuit chip every two years should result in further miniaturization of electronic devices. However, current production of efficiently operating transistors or capacitors will soon reach physical size limits and thus further scaling will be impossible to implement – as of yet.

Therefore, over the past decades, many scientific groups have been searching for solutions to bypass this problem.

A promising solution which researchers have noticed in almost all oxide materials is the phenomenon of resistive switching (RS). It was first observed in the early 1960s (1) then 'rediscovered' almost 20 years ago. The most intense research on the resistive switching effect concerning potential applications did not start until the work of Bednorz et al (2). However, until now, no clear model of this phenomenon has been formulated.

The RS phenomenon can be defined as a reversible change of the resistance in/of the material under external gradients. This feature gives the opportunity to use the different resistance states of a particular material for storing information. One of the most ideal models are perovskite materials which show the RS phenomena is activated by $SrTiO_3$.

This material exhibits that an approximate 2nm dislocation could be individually addressed and act as bistable nanowires (3) .

Moreover, the advantages associated with the RS phenomenon has caught the attention of the scientific society and industry, especially the three most promising candidates for further application: the metal oxides – titanium, niobium and tantalum

The binary oxide, TiO_2 is the most studied model material for applications and the number of publications on it continues to grow significantly year by year. According to Web of Science, there are currently 536 works describing the resistive switching phenomena in TiO_2. For Ta_2O_5 and Nb_2O_5 the amounts are about 72% less. Hence, the small amount of research of Nb_2O_5 and Ta_2O_5 and the corresponding understanding of the RS mechanism inside these oxides suggest the need for further study.

In late 2011 Lee et al. (4) showed a promising system based Basically, the idea assumes that once the resistance state is written, no further power supply is needed to retain the state. Therefore, in early 2013, Panasonic company offered on the market 8bit microcontrollers in which the conventional volatile random-access memories were replaced with redox-based random memories (ReRAM) based on 180 nm TaO_x/Ta_2O_5 (5). Their other report also showed promising properties had been observed in the NbO_2/Nb_2O_5 systems (6,7) .

The general idea of this dissertation is to compare the fundamental physical-chemical properties of the two adjacent metal oxides systems: Nb-O and Ta-O in connection with the study of the RS phenomenon. The main aim of this work was to perform an investigation dependent on the reduction condition (oxygen partial pressure or critical electric potential difference in electro-degradation processes) on a single crystal in macro and nano scale and to find the relation of those results to those obtained for thin films (Figure 1.1). The studies were performed on a Nb_2O_5 single crystal. Additional studies of Nb_2O_5 and Ta_2O_5 in thin film form were also conducted.

The fundamental properties were characterized using many techniques such as: X-ray Powder Diffraction, X-ray Photoelectron Spectroscopy, Time of Flight Secondary Ion Mass Spectroscopy, Raman Spectroscopy and Scanning Probe Microscopy.

This work is divided into five chapters. The following chapter gives a brief overview of fundamental physical and chemical properties of transition metal oxide of Nb-O and Ta-O systems as well as the defect dimension and resistivity switching. In the chapter, the three most important experimental methods are described. This includes various techniques of

samples prepared as well as characterization methods of the particular properties of the investigated system. Results and discussion are presented in chapter four. Chapter five is the summary of the presented work.

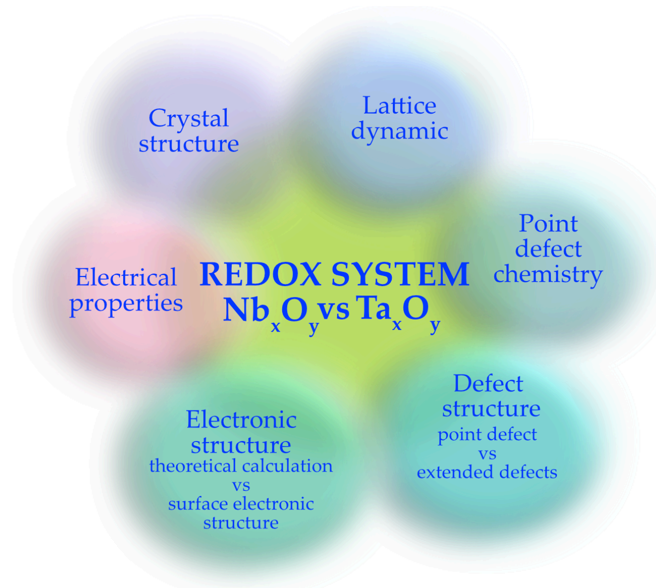

Figure 1.1 Scheme of investigation of niobium and tantalum oxides

2. Fundamentals

Knowledge and literature items about niobium–oxygen and tantalum – oxygen system are particularly complex. Since the 1940s, these systems, especially those of niobium have been extensively investigated (8), nevertheless many questions remain unanswered. One is the resistivity switching phenomenon found in both metals oxides (9,10). Until today, no coherent model is available which describes the switching mechanism. According the Web of Science database, from 2003 to 2018 only 36 work have been published describing the resistivity switching phenomena (RS) in the niobium oxides system and the 154 in tantalum oxide system. Below are presented fundamental properties of niobium and tantalum oxides which are related to the redox process and resistivity switching phenomena.

First, as can be seen in the phase diagram of the Nb - O system (Figure 2.1) the most stable oxide is Nb_2O_5. Hence, an underlying oxide, niobium pentoxide, especially in the form of a single crystal is most considered in this thesis and was compared with a thin film. The methods of preparing a single crystal of Nb_2O_5 are few, and all are described briefly below. Although there are several fabrication methods of the thin film, only the sputtering technique for growing thin film is presented below.

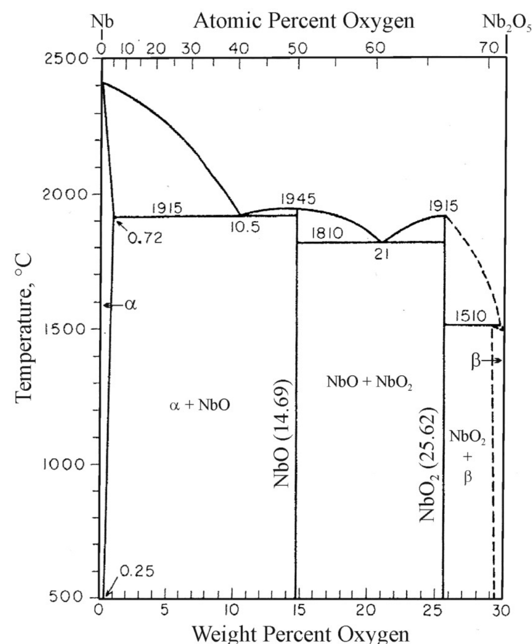

Figure 2.1 Phase diagram of Nb-O system

2.1 Crystal growth

Through the centuries scientists have searched for methods, to copy and reconstruct the beauty of crystals. Consequently, their features can be reconstituted by several growth techniques, utilizing different phases of materials - solid, liquid or gas. The first and the most popular is the Czochralski method or its modification which is currently used to obtain suitable quality semiconductors on an industrial scale. In this process, the crystal growth begins from molten materials. Other techniques for semiconductor preparation of metal, oxide or halides crystals are: Floating Zone, Verneuil, Bridgman–Stockbarger or their modifications. Only Optical Floating Zone (OFZ) is commonly used to manufacture niobium oxide crystals and described in detail, below.

From a historical point of view it would be inconsiderate to omit flame-fusion Verneuil method (Figure 2.2), the base technique for crystal growth, especially for the growth of ruby and sapphire. This relatively uncomplicated process starts with pure powdered base material being applied into a furnace. Next, when the furnace bottom is opened, the powder falls into a small tube filled with oxygen and the powder and gas are mixed. Then a second large tube close to the first one is filled with hydrogen. The process is started after temperature up to 2200°C is applied. The materials then fall in the form of small droplets onto a place situated below and form the cone with the liquid top. The cantilever with the cone is slowly moved away from the flame which results in crystallisation of the colder part of the cone. The new small droplets are added to the top and formed into the shape of a cylindrical crystal (11,12,13,14).

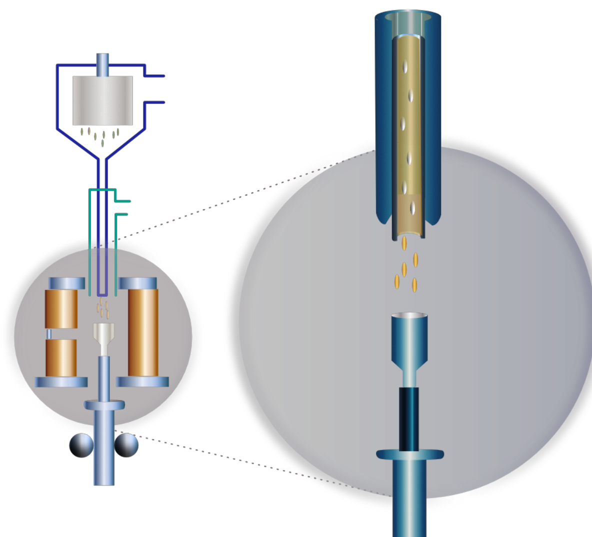

Figure 2.2 Scheme of Verneuil process (14)

Another melting technique used to obtain niobium oxide crystal is the Bridgman-Stockbarger process. This method was first applied in the 1970s by Ko et al. (15) to obtain H-Nb_2O_5 single crystal. A characteristic of this process is the fact that single crystal growth is realized along specific crystallographic orientation. The growth process of the single crystal is started by melting polycrystalline material in the hot zone and transporting it towards the seed situated at the bottom of the crucible (Figure 2.3). Then the part of the seed is re-melted through touching the melted material. In the next step, the crucible is moved slowly to a cooler section of the furnace. At the end, the temperature at the bottom of the crucible falls below the solidification temperature, and the crystal growth started from the seed at the melt-seed interface, is realized. After this, the whole crucible is transported to the cold zone, below the melting point of the material and the complete molten charge converts to a solid single-crystalline ingot. (13,16)

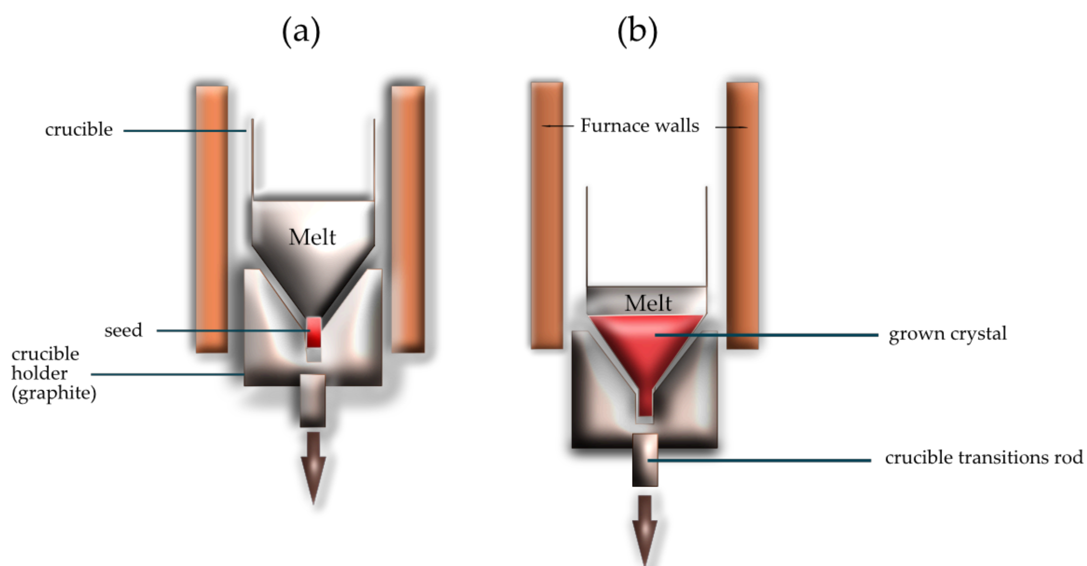

Figure 2.3 Schematic diagram of a vertical Bridgman (VB) crystal growth process in a single-zone furnace (a) at the beginning of the experiment and (b) with partially grown crystal

The last described fabrication method of oxide crystals is the Floating Zone (FZ) technique. Through this process, suitable quality niobium pentoxide crystals can be obtained. Since the 1950s, FZ has been used to manufacture ultra-pure silicon crystals (13) and currently it is usually used to manufacture materials that are difficult to synthesize in a crystalline form. Since the 1980s, when halogen lamps and the ellipsoidal mirror were applied, it was used to obtain magnetic materials and superconductors. Since this implementation, it has often been called Optical Floating Zone (OFZ) (17) and this

process has also been used in this work to manufacture Nb_2O_5 single crystal. Figure 2.4 shows the process of growing the single crystal. A ceramic feed rod is suspended in the furnace above a polycrystalline or single crystal seed. The OFZ starts after melting the tip of the polycrystalline rod connecting the ceramic rods through a liquid zone formed from the melted polycrystalline material called a floating zone. When the zone is created, the material starts moving upward, by moving the seed and feed setups downward or moving the mirror upward. After this process, the melted material is cooled, and the crystallization processes begin on top of the seed rod. When crystal growth is rotated from 0 to 50 rpm in the same or opposite direction, the crystal growth can be optimized. Rotation is responsible for the mixing of the material and the shape of crystallisation font and crystal defects. In the case of crystal presented in this dissertation, it was grown at a temperature of 1450° C with a speed of 1 mm for 1hour and rotation equal to 32 rpm.

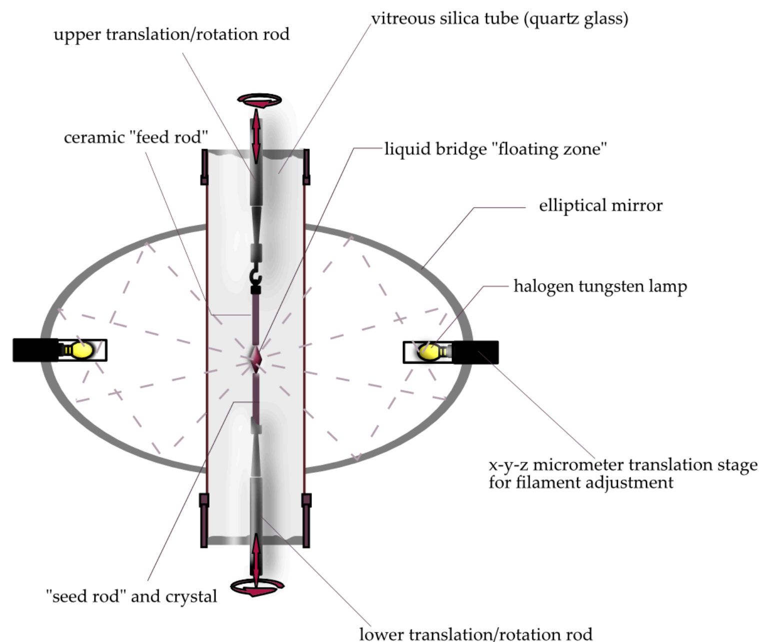

Figure 2.4 Schematic drawing of the optical floating zone. (17)

2.2 Thin film preparation by sputtering technique

From the first observation by Grove in 1852, deposition of thin films by sputtering has been defined as the process of the ejection of the particle from a condensed matter target due to the impingement of energetic projective particles(19). The process is shown in detail in Figure 2.5. The atoms which form a layer on the substrate are obtained by bombardment of the target surface via energetic ions in a partially ionized rare gas (plasma), e.g. Ar^+, Kr^+, Xe^+ composed of ions and electrons. Sputtering can also be a result of bombardment of other energetic ions, neutrals, electrons and even photons. The ions are produced in a high vacuum chamber by applying a high voltage between electrodes at low pressure. Pressure of 10^{-3} to 10^{-1} mbar is necessary to obtain non-thermal plasma using low ignition power. The system usually consists of high vacuum chambers equipped with a two-stage vacuum pumping system. Inside the chamber, the target and substrate are mounted opposite to each other on the same axis at a distance between a few millimeters to several centimeters. Using an appropriate generator, an electric potential is applied to the target.

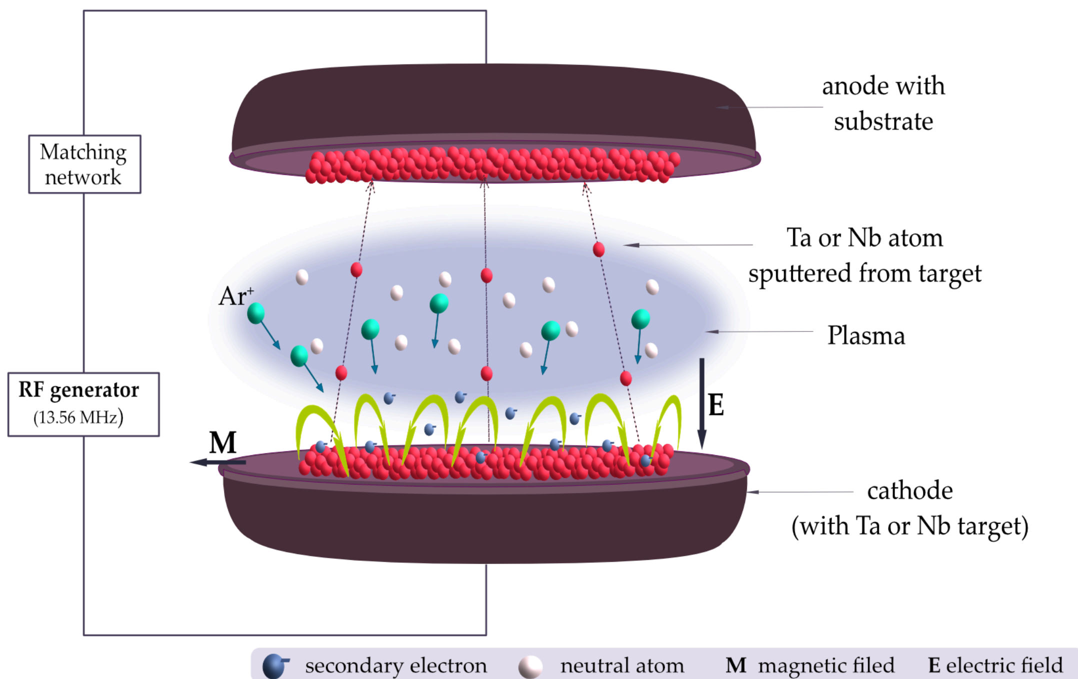

Figure 2.5 Diagram of RF- sputtering process (adapted from (21))

For particular target material and the requested process, the deposition can be induced using pulsed DC voltage at pulse frequencies up to 100kHz, RF voltage at a frequency of 13.56MHz or pulsed RF voltage (20). The ion is usually neutralized by pulling an electron from the near-surface region just before impact and impacts the surface as a neutral. Because it is quite easy to generate large fluxes of ions at controlled energies, all applications of sputtering use ions as the bombarding particles. Thin film investigated in this thesis was made by RF sputtering technique. Experimental details for the growth of both oxides have been prepared as described by S. Schmelzer dissertation (20).

2.3 Niobium - oxygen system

To begin, it is worth mentioning that since its discovery by Charles Hatchett in 1801, Niobium (Nb) was also called Columbium (Cb) (22,23). The names was used in parallel until 1950. This element does not occur in nature in a free metallic state but usually together with Fe or Mn in the form of crystal named columbite $(Fe,Mn)Nb_2O_6$.

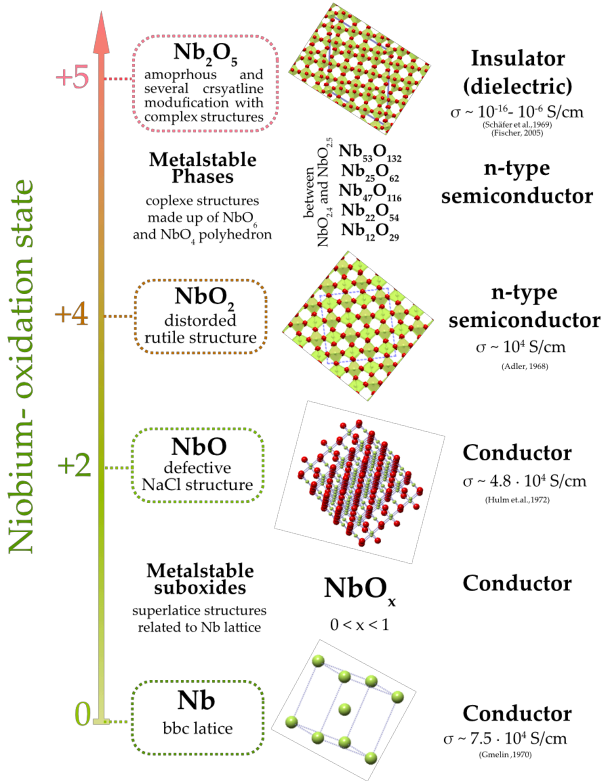

Figure 2.6 The niobium-oxygen system: main oxides and some of their structural and electrical properties (conductivity σ given at ~ 0°-25°C) as a function of the formal Nb- oxidation state (adapted from (24))

The element which Hatchett obtained from crystal matrix is a transition metal which has atomic number 41 with an atomic mass of 92,9064 and electronic configuration $[Kr]4d^4 5s^1$. Niobium, a shiny, silver metal with typical body-centered cubic structure, niobium belongs to the Im3m (229) space group, with a high melting point of 2477°C, density 8.57g/cm^3 and with a resistivity of about 13.4 μΩ·cm at 0°C (24). Moreover, it is a superconductor below the transition temperature $T_c \sim 9.3$K (25). This metal is also highly reactive and characterized by a high resistance to corrosion in many environments (24,26). Moreover, Nb forms a large variety of oxides (24) with a wide range of interesting physical properties (Figure 2.6). However, only a few stable oxides such as NbO, NbO_2 and Nb_2O_5 (see phase diagram Figure 2.1) exist. Detailed properties of known niobium oxides are described below.

2.3.1 Niobium monoxide (NbO)

The first work describing NbO crystal structure was written by Lehl et al. in Gmelins Handbook on Inorganic Chemistry in 1970 (24). Several years later, Pialoux et al. also showed the stable NbO phase with space group $Pm\bar{3}m$ (no. 221). This niobium oxide has a defective rock-salt structure with 25% orders vacancies in the Nb- and O- sublattices (24). This oxide like other transition metal oxides shows numerous point defects. Detailed explanation of this issue is described at point 2.7 in this chapter. Elilott (24) and Niebuhr (27) then showed that density of NbO is ca. 7.3 g/cm^3 with a melting point about 1935-1945°C. The electronic configuration of NbO is $[Kr]4d^3$. Niobium oxide at room temperature shows characteristic metallic behavior (24,28-30) and electrical resistivity of about 21μΩ·cm. Furthermore, below the transition temperature $T_c \sim 1.61$ K (31) the oxide is superconducting.

2.3.2 Niobium dioxide (NbO_2)

Cheetman and Rao (29) described semiconductor NbO_2 by neutron diffraction as a tetragonal crystal with space group corresponding to $I4_1/a$ (no. 88). They also showed that at low temperature the phase is distorted rutile by a chain of edge-sharing NbO_6 octahedra, cross-linked by corner-sharing (24,32). Valence state of Nb in NbO_2 is +4 which corresponds to the electronic configuration of Nb $[Kr]4d^1$. The density of NbO_2 is 5.9 g/cm^3 (33), and it melts at 1915°C. Moreover, at room temperature it is an n-type

semiconductor with an electrical resistivity of 10^4 Ω·cm (34), but above 800˚C - NbO_2 changes to a metallic conductor (24,32). Furthermore, in thin films at room temperature NbO_2 exists not as a single phase but predominantly as a layer under the Nb_2O_5 (35,36).

2.3.3 Niobium pentoxide (Nb_2O_5)

Nb_2O_5 is the most stable compound in the Nb-O system. The niobium pentoxides have several crystalline, and amorphous modifications (see Table 1). The high-temperature modification of Nb_2O_5 with monoclinic phase is marked as H-Nb_2O_5. Thermodynamically, it is the most stable form of niobium pentoxide. It is commonly obtained as a single crystal by zone floating technique (37,38). H-Nb_2O_5 has an ordered block structure with (5x3) and (4x3) group of corner-sharing NbO_6 octahedra with each block (39). Furthermore, the H-Nb_2O_5 (Figure 2.7) is also called α-Nb_2O_5 (36). Zibrov et al. (40) showed that pressure and temperature modification of H-Nb_2O_5 at 7.5-8 GPa and 800˚C -1000˚C lead to the formation of a new phase called Z-Nb_2O_5. This phase has seven coordinated octahedrons (NbO_6) and is less stable than B (see Table 1) or T-Nb_2O_5. Low-temperature T-phase is different from H. Its unit cell consists of 42 oxygen atoms, 8 niobium atoms form disordered octahedrons and second 8 niobium atoms which form pentagonal bipyramids. Moreover, 0.8 Nb ion per unit cell is located at interstitial 9-coordinated sites of the unit cell (36). T-phase is formed at ca. 500˚C. Ko and Weissman (39) reported that at temperature ca. 200˚C, Nb_2O_5 is in an amorphous phase. The temperature modification of Nb_2O_5 is shown in Figure 2.7 (39). Niobium pentoxide (24) melts at about 1495˚C and Nb formal valence state is +5, corresponding to the electronic structure of Nb atoms [Kr]$4d^0$. Kurmaev et al. (41) showed that d-electrons in Nb_2O_5 had been transformed to the O 2p-band and the Nb 4d - the band is empty as a result of niobium pentoxide as an insulator (35). The H-Nb_2O_5 is an n-type semiconductor (42) . It is worth to mention here that in the nanoscale they are usually grown as nonstoichiometric (43) by formula (2.1)

$$Nb_{3n+1} + O_{3n-2} \rightarrow Nb_2O_5 \tag{2.1}$$

	Properties						
	Crystal structure	Unit-cell parameters [Å]				Density [g/cm³]	Crystallization temperature[˚C]
		a	b	c	angle [°]		
H(α)-Nb_2O_5 (36,37,42,44,45)	monoclinic	21.34	3.816	19.47	β=120.33	4.52	1000-1100
	monoclinic	20.37	3.822	38.70	β=115.69	4.548	
	Monoclinic (P2/m)	21.153(7)	3.8233(5)	19.356(5)	β=119.80(2)		
TT- Nb_2O_5 (36,46)	monoclinic	7.23	15.7	7.18	β=119.5	4.99	770-870
T(γ)- Nb_2O_5 (36,47,48)	Orthorhombic (Pbam)	6.175(1)	29.175(4)	3.930(1)		5.236	773
N - Nb_2O_5 (49)	monoclinic (C2/m)	28.51	3.820	17.48	β=120.8	4.59	1100-1110
B - Nb_2O_5 (42)	Monoclinic (C2/c)	12.73	4.88	5.56	β=105.1	5.29	1020-1120
M (β) - Nb_2O_5 (50)	Tetragonal (I4/mmm)	20.44	20.44	3.832		4.4	1103
P - Nb_2O_5 (42)	Tetragonal ($I4_122$)	3.876	3.876	25.43		4.54	1020
L-Nb_2O_5(42)	orthorhombic	6.168	29.312	3.938		4.965	1020-1120
Z-Nb_2O_5 (50)	Monoclinic (C2/m)	5.2193(2)	4.6995(2)	5.9285(2)	β=108.559(2)	6.40	1070-1270
R-Nb2O5 (50)	Monoclinic (A2/m)	3.983	3.826	12.79	β=90.75		820-920

Table 1 Crystal structure of Nb_2O_5

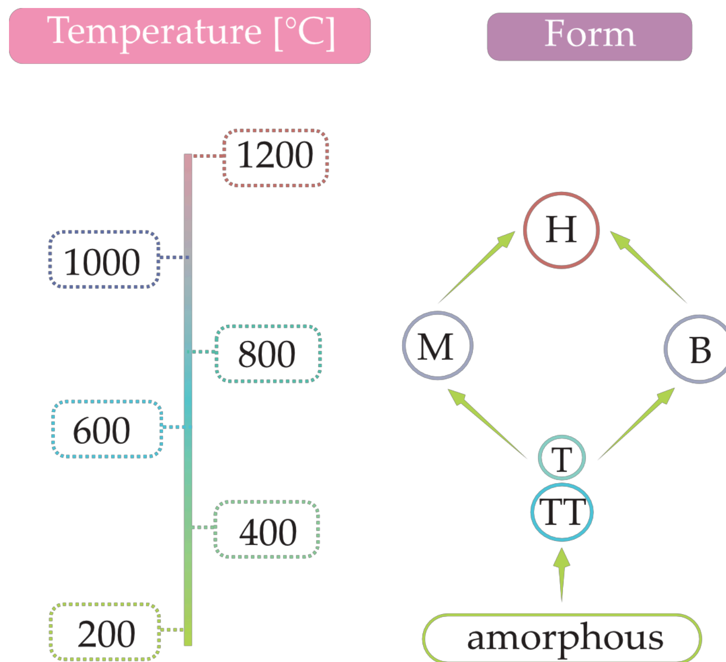

Figure 2.7 Temperature modification of Nb_2O_5 (adapted from (36))

2.3.4 Other niobium oxides

In literature several other niobium oxides such as: NbO_x, NbO_y, NbO_z, Nb_6O, Nb_4O, $Nb_{12}O_{29}$, $Nb_{22}O_{54}$, $Nb_{25}O_{62}$ or $Nb_{52}O_{132}$ have been noted (35,51). Their stability and crystal structures depend on their growth conditions. For example, at 270-500°C a NbO_x is formed and correspond to the ideal formula Nb_6O (24). This suboxide is also formed as an interface layer between near-stoichiometric Nb_2O_5 on Nb the surface (35,51) after oxidation in the air. In the 330-500°C range, another niobium oxide, NbO_y is also formed. Its formula is close to the one of ideal Nb_4O (24). However, the composition of NbO_z which is formed at 400-700 °C is still unknown (24). The $Nb_{12}O_{29}$, $Nb_{22}O_{54}$, $Nb_{25}O_{62}$ or $Nb_{52}O_{132}$ phases are described in literature (35,52,53) as non-stoichiometric Nb_2O_{5-y}. These metastable oxides are n-type semiconductors which general formulas are $Nb_{3n+1}O_{8n-2}$ and $Nb_{3n}O_{8n-3}$. Only a few of them are stable. The ideal $Nb_{12}O_{29}$, $Nb_{22}O_{54}$, $Nb_{47}O_{116}$, $Nb_{25}O_{62}$ and $Nb_{53}O_{123}$ are mainly built from blocks of NbO_6 octahedral and NbO_4 (24). However, under certain conditions, some of them can crystallize in different phases (24). Thus, $Nb_{12}O_{29}$ (24) at a different temperature preparation can crystallize - in a monoclinic or an orthorhombic phase. Their conductivity at room temperature are $3 \cdot 10^2$ S/cm, $5 \cdot 10^2$ S/cm, $2 \cdot 10^3$ S/cm for $Nb_{53}O_{132}$, $Nb_{25}O_{65}$ and $Nb_{12}O_{29}$ (54), respectively.

2.4 Electronic structure of Nb-O system

The other, most important future application related to resistivity phenomena is the electronic structure. In literature, many theoretical calculations regarding this topic can be found. The theoretical density functional theory (DFT) is described for a few oxides from the Nb-O system: NbO, NbO_2 and Nb_2O_5.

The first theoretical and experimental investigation of NbO was presented by Erbudak et al. (55). In their work, the result from photoemission energy distribution curves obtained with the use of synchrotron radiation and calculations was made by Hartree-Fock-Slater model (called self-consistent field (SCF) method) for cluster NbO_6^{10-} which showed that in this oxide, polarization effect does not significantly affect its crystal structure. The calculation results for molecular orbital (MO) are shown in Figure 2.8. Mainly, in the Nb4d, the $3t_{2g}$ valence orbitals are occupied. The lower MO t_{1g}- 4_{eg} are assigned to O 2p with covalent admixtures of 4d, 5s and 5p niobium states. Furthermore, the O 2s state with a small admixture of niobium orbitals consists of $6a_{1g}$, $3e_g$, $5t_{1u}$ molecular orbitals. The spin-

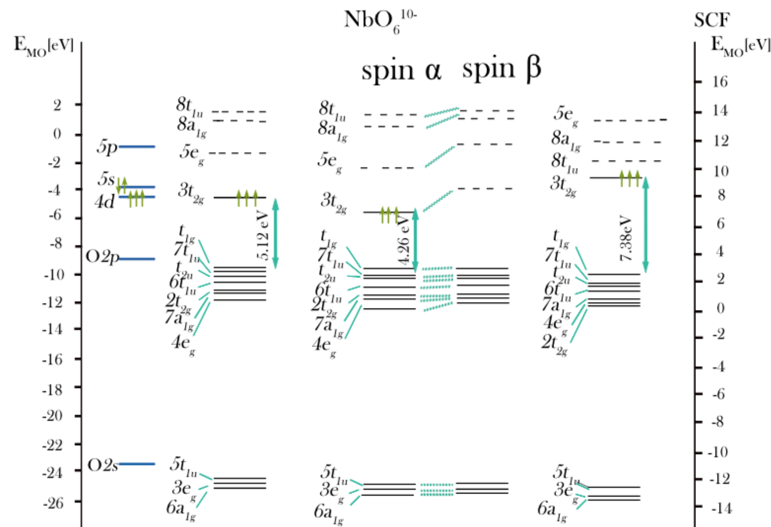

Figure 2.8 Molecular orbitals (MO) diagrams in spin-restricted (left) spin- polarized (center) self-consistent and (right) calculation with use of discrete variational method (DVM) of NbO_6^{10-} cluster (adapted from (55))

restricted method showed only energy changes for α and β spin in Nb 4d orbital in $3t_{2g}$ and 5_{eg} MO's. The difference between both orbitals equals 0.1eV. The diagram (see Figure 2.8) also shows results from SCF and non-SCF calculations, where only change for $3t_{2g}$ MO has been observed.

Kurmaev et al. (41) then calculated density of state (DOS) for Nb and NbO, NbO_2 and

Nb_2O_5. In the pure, cubic body centered Nb crystal, the strong hybridization is related to Nb 4d orbitals - the partial DOS is in quite good agreement with Nb 5p, probably due to the diffusive character of Nb5p. This result has been confirmed with the use of X-ray emission spectra (XES) for Nb $M_{4,5}$. Natural NbO consist of 25% structural vacancies, due to this fact authors choose for the subsequent calculations $Nb_{0.75}O_{0.75}$ with the NaCl-like crystal structure. In the NbO induced vacancies, states are located below the Fermi level and occupy Nb 4d states with DOS lower than $Nb_{0.75}O_{0.75}$. Moreover, the Nb 5p wave functions are strongly hybridized with O 2p and Nb 4d functions. The vacancy-induced Nb 4d states and splitting of O 2p band are more noticeable in the Nb 5p DOS for $Nb_{0.75}O_{0.75}$. The results obtained from XES for this oxide are more compatible with the calculation for $Nb_{0.75}O_{0.75}$ than NbO. Later, in this work, the authors choose tetragonally - NbO_2 and monoclinic crystal structure of Nb_2O_5 for their further calculation of DOS. The outcomes (Figure 2.9) showed that for the energy spectrum of both compounds one observes atomic- like oxygen 2s - bands with binding energies of 19 and 15 eV and the next band has an O2p-character with banding energies 4 and 0eV for NbO_2 and Nb_2O_5, respectively.

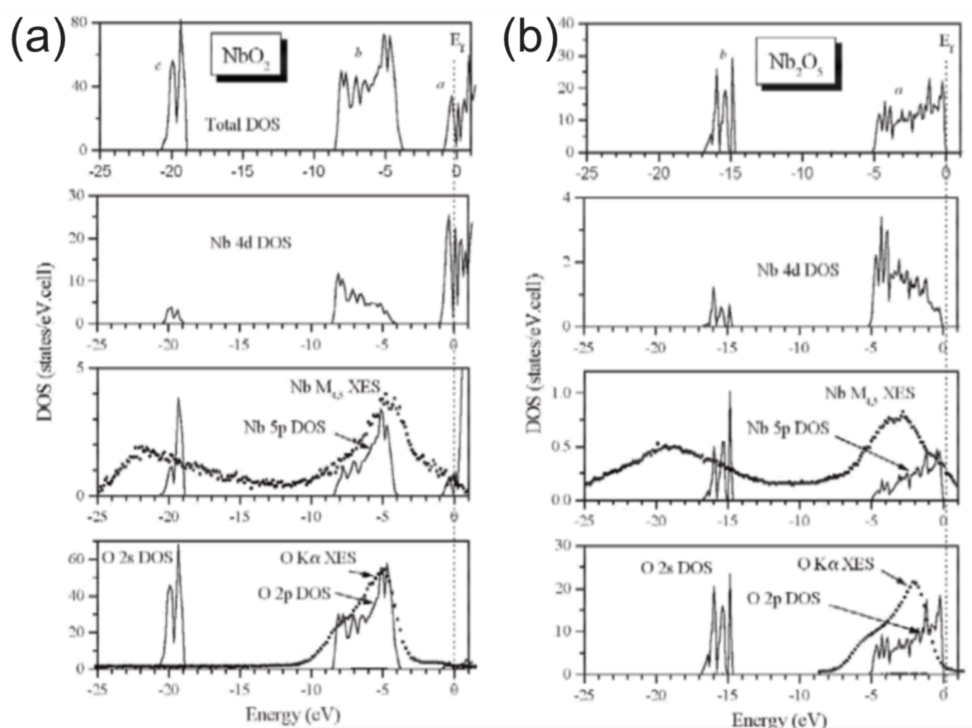

Figure 2.9 Total and partial DOS of (a) NbO_2 and (b) Nb_2O_5. The third pane from the top presents comparison of experimental (dots) and DOS calculations (41).

In NbO_2, the atomic configuration of Nb atoms is d^1. Hence Fermi energy crossed the Nb 4d band which results in the semiconducting behavior of the compound. However, in Nb_2O_5 all d-electron are transferred to O 2p and d-band is empty. The result is niobium atoms with d^0 configuration and Fermi energy located near the top of the valence band. Hence, as obtained from the experiment, Nb_2O_5 is an insulator with a calculated band gap equal to 3.53 eV and 3.9eV. Despite, Weibin et al. (56) showed for NbO_2 and Nb_2O_5 that the band gap is 0.25eV and 2.55 eV respectively (Figure 2.10). Neverthenless, in the experiment value the of this oxide is 0.7eV for NbO_2 and 3.7eV for Nb_2O_5. Moreover, they also showed the total and partial calculation of DOS for both oxides (Figure 2.11).

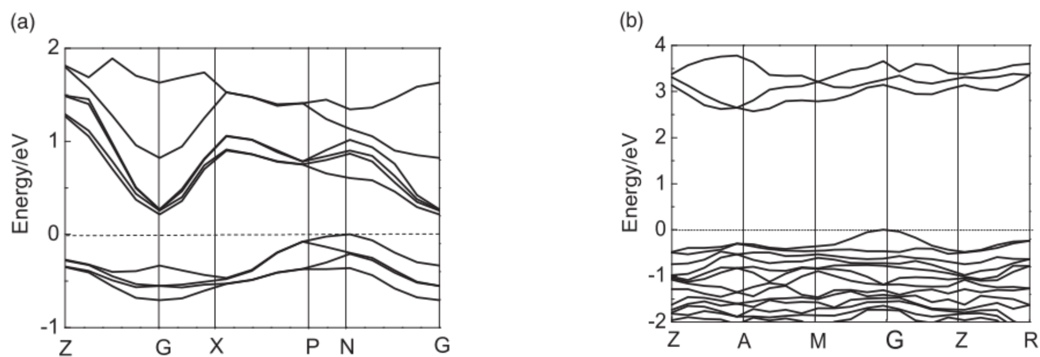

Figure 2.10 The electronic band structure for different niobium oxide: (a) NbO_2 (b) Nb_2O_5 (56)

In the valence band maximum (VBM) state for Nb_2O_5 and NbO_2 presented in Figure 2.10a and 2.10b, O2p and Nb4d are hybridized, while in the Nb_2O_5 in addition to O2p and Nb4d orbital also a little part of Nb4s orbital is hybridized. The authors also presented experimental results where the electronic structure obtained from UPS on Nb thin film deposited by pulsed laser exposure in air are in good agreement with the calculated results. The Nb_2O was composed of tree peak with banding energy equal 2, 6 and 11eV contributed to Nb4d, O2p and Nb4d orbital, respectively. Whereas, Nb_2O_5 was composed of two peaks, first O2p at 7eV and a second peak at 14 eV which is the contribution of strong hybridized O2p and Nb4d states

The other work showed that the monoclinic B-Nb_2O_5 build with disordered NbO_6 octahedra arranged in strings compound of pairs of edge-sharing octahedral linked in zigzag of corner-sharing octahedra has a band gap equal 2.5eV for PBEsol a 4.1eV for HSE06 (57), where Perdew–Burke–Ernzerhof (PBEsol) and Heyd–Scuseria–Ernzerhof (HSE06) are the applied functional. The first is exchange-correlation and second hybrid functional, respectively. The VBM is in Γ-point where as conduction band minimum is located along $\langle \bar{v}, v, v \rangle$ direction. The bang gap in the Γ-point is equal $E_g^{PBEsol} = 3.1\ eV$ or $E_g^{HSE06} = 4.6\ eV$. The result is not confirmed experimentally only by reported data where the measured gap was 3.4 eV for H-Nb_2O_5 and the T-Nb_2O_5 whereas 4.2eV for the amorphous phase. The simulation of DOS indicated that the valence band is built up from the hybridized Nb d-states and O-p states. In this structure, p-states dominate in VBM and arise mainly from O_2 and O_3 ions. However, the conduction band and CBM consist of mainly Nb d-states and arise from the Nb ions (Figure 2.12)

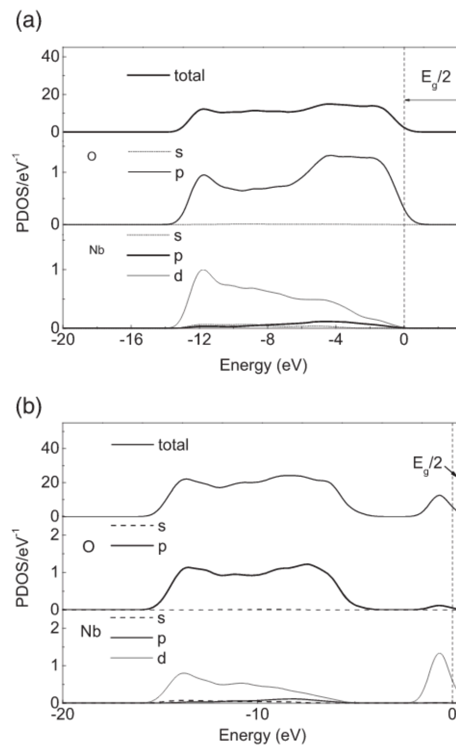

Figure 2.11 DOS calculation of (a) Nb_2O_5 and (b) NbO_2 (33)

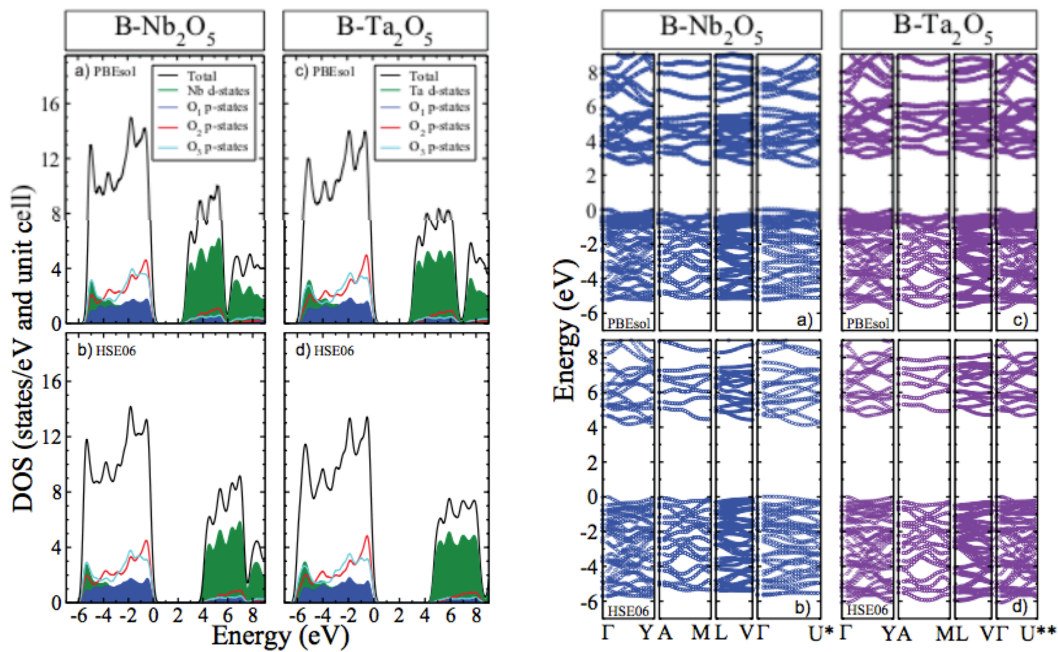

Figure 2.12 Calculated dispersion relation along the high symmetry directions in the irreducible Brillouin zone for (a) B-Nb_2O_5 with PBEsol, (b) HSE06, and B-Ta_2O_5 with (c) PBEsol and (d) HSE06 and calculated total and site-projected DOS for B-Nb_2O_5 with (a) PBEsol, (b) HSE06, and B-Ta_2O_5 with (c) PBEsol, (d) HSE06. The black lines correspond to total DOS; the green-shaded areas correspond to Nb (Ta) d-states, the blue-shaded areas, red lines and cyan lines correspond to O_1, O_2, and O_3 p-states, respectively. The energy is shifted to the VBM. (57)

2.5 Tantalum – oxide system

Tantalum as a pure element was discovered a year later than Niobium in 1802 by Ekeneberg. The process of obtaining pure metal was like the 'torture of Tantalus' hence he named the new element as Tantalum (58). For about 60 years after its discovery, many researchers believed that Nb and Ta where the same elements until researchers showed

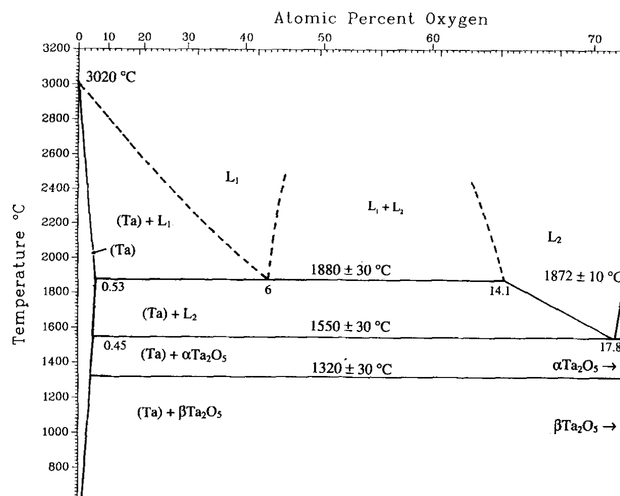

Figure 2.13 Phase diagram of Ta-O system

that their acids were not the same compounds. Like Niobium, Tantalum primarily occurs as a mineral called tantalite (Fe, Mn)Ta_2O_6, always with Nb and impurities like Fe and Mn. The element is a grey transition metal which has atomic number 73 with a relative atomic mass of 108.9479 and electronic configuration [Xe]$4f^{14}5d^{3}6s^{2}$. Tantalum melts at 2994°C. Typically Ta has body-centered cubic (α-Ta) structure, which like Nb, belongs to Im3m (229) space group and has density 16.634 g/cm^3. It has a low resistivity in the range 15 μΩ·cm to 60 μΩ·cm (59). However, Ta has two more phases. The second phase known as β is metastable and has tetragonal crystal symmetry ($P4_2$/mnm). Its density is equal to 16.33 g/cm^3. The β-Ta usually is produced by sputtering (60), chemical vapor deposition (61) and electrochemical deposition from a molten-salt solution (62). This phase has much higher electrical resistivity then α. The resistivity range is from 170 μΩ·cm to 210 μΩ·cm(59). The last known phase of Ta, which was reported in a few works concerning the metal deposited as a thin film (60) is centered cubic (fcc). Recently Janish et al. (60) demonstated that in deformed textured Ta sputter target cut by electro-discharge machining (EDM) also showed a hexagonal close-packed (hcp) structure. This metal, also like Nb, is highly reactive and characterized by a high resistance to corrosion in many environments (63,64). Moreover, Ta forms a variety of oxides with a wide range of interesting physical properties. Only a few stable oxides like TaO_x, TaO_2 and Ta_2O_5 exist (see phase diagram Figure 2.13) and, are described below in more detail.

2.5.1 Tantalum dioxide

Garg et al. (65) showed that TaO_2 could be obtained by several methods, e.g. oxidation of Ta powder with Zn oxide and oxidation of Ta carbides under steam, reduced Ta_2O_5 with magnesium or carbon in vacuum or reduction of Ta_2O_5 by shock loading to 50 - 60 GPa. It has tetragonal crystal symmetry ($P4_2$/mnm) and a rutile - type structure (65). Recently, Muraoka et al. (66), showed that TaO_2 phase is formed on an NbO_2 layer manufactured by pulsed laser deposition.

2.5.2 Tantalum pentoxide

The most stable form of tantalum oxide is Ta_2O_5. In nature, it is a transparent microscopic colourless mineral called Tantite. It melts at about 1870 °C. The tantalum pentoxide is also characterized by high index refraction near 2.152 at 663 nm, large transmittance 0.3 -10 lm and high k dielectric constant from 30 to 110 (67,68). The crystal structure of Ta_2O_5

is similar to Nb_2O_5. Due to the growth condition, it can also be classified as low or high temperature and high pressure. The low-temperature phases are T, TT, L, β and δ (see Table 2).

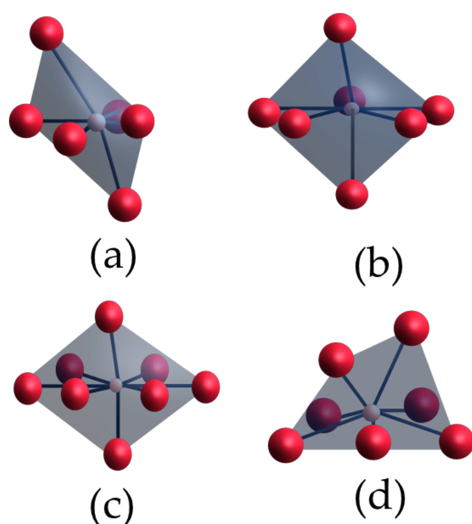

Figure 2.14 Representative polyhedra cut from some of the relaxed crystal structures of Ta_2O_5. (a) Distorted octahedra TaO_6, (b) pentagonal bipyramid TaO_7, (c) hexagonal bipyramid TaO_8 and (d) mono-capped trigonal prism TaO_7. (69)

The most stable is L- phase in 1360 ˚C. Moreover, at the same temperature, the H-phase is formed. It is also called high–temperature phase. The temperature modification is shown in Figure 2.15. The B and Z- phases are classified as high-pressured.

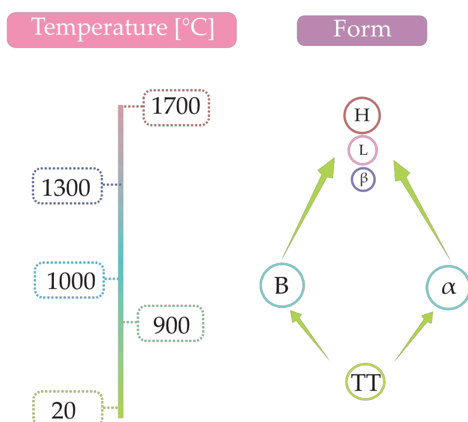

Figure 2.15 Temperature modification of Ta_2O_5

They are formed at 8GPa in 1000˚C to 1300˚C temperature range. Furthermore, those phases of Ta_2O_5 show different polymorphism. It can be divided in phases formed from disordered octahedra - TaO_6 (B, β and λ), a combination of disordered octahedra and pentagonal bipyramids - TaO_7 (β, L, H, T), single form of TaO_7 polyhedra (Z) and disordered octahedra and hexagonal bipyramids -TaO_8 (δ)(69) (Figure 2.14)

	Properties						
	Crystal structure	Unit-cell parameters [Å]				Density [g/cm^3]	Crystallize temperature[°C]
		a	b	c	angle [°]		
L-Ta_2O_5 (70)	orthorhombic	6.198	40.290	3.888		8.31	1700-1350
	monoclinic (C112/m)	6.1939					
H-Ta_2O_5 (71,72)	orthorhombic	35.6	3.79	3.735			1320
	tetragonal	3.801	3.801	35.67			1640
	monoclinic	3.784	3.802	35.82	β = 91		
	monoclinic	5.367	5.368	35.707	β = 91,42		
	triclinic	3.794	3.807	35.70	α= 90°,54.4' β = 90°,11.5' γ= 89°,59.9'		1775-1400
B-Ta_2O_5 (40)	monoclinic (*C*2/*c*)	12.7853 (4)	4.8537 (1)	5.5276 (2)	β= 104.264 (2)		1000–1300
Z-Ta_2O_5 (40)	monoclinic (C2)	5.2252(1)	4.6991 (1)	5.8534(1)	β= 108.200(2)		
TT -Ta_2O_5 (73)	hexagonal (P6/mmm)	3.639		3.901			20-900
T-Ta_2O_5 (73)	orthorombic (Pmm2)	43.997(8)	3.894(1)	6.209(3)			
δ- Ta_2O_5 (73,74) (57)	hexagonal	3.62	3.62	3.87			
	hexagonal	7.191	7.191	3.831			
λ- Ta_2O_5(75)	orthorombic (Pbam)	6.25	7.4	3.83			
β -Ta_2O_5 (76) (77) (78)	orthorhombic (Pccm)	6.217	3.677	7.794			1320
	orthorombic	7.353	6.179	3.858			
	monoclinic	7.316	15.54	21.22	β= 120.6	8.9	1400
α-Ta_2O_5 (78)	tetragonal	3.80	3.80	35.58			550-1100

Table 2 Crystal structure of Ta_2O

2.5.3 Other Tantalum oxides

In their work Garg et al. (65) also showed several stable and metastable forms of the Ta-O system. For example, TaO_x, TaO_y, TaO_z, TaO_u, Ta_2O, Ta_2O_3 or Ta_3O_9 and others. The first four phases (TaO_x, TaO_y, TaO_z, TaO_u) as described in literature are not well defined. However, recently TaO_x has become the most often studied oxide in thin films form because of its potential application in redox-oxide memory (ReRAM) (79,80,81). This metastable phase described by Brauer et al. is obtained by oxidation of Ta powder at ca. 350˚C for 2 hours. Moreover, at phase TaO_y (65) is formed on a thick Ta sheet at oxygen pressure $6.67 \cdot 10^{-2}$ Pa at 300 ˚C for 10min. The other crystal structure of TaO_y is described in literature (65) as the orthorhombic phase corresponding to β-phase of Ta_2O_5. It is obtained by oxidation of Ta powder or Ta hydride at a temperature between 600 ˚C to 900 ˚C for periods between 1 to 48 hours. However, the cubic phase of TaO_z is formed after heating monocrystalline Ta thin film at 380 ˚C for 1h at an oxygen pressure of $6.67 \cdot 10^{-2}$ Pa (65). Gang et al. (65) also noted the TaO_u phase. It is formed under oxygen pressure below 1.33 Pa a temperature of 1500 ˚C. As mentioned by Gnanarajan et al. (82), another tantalum oxide phase is Ta_2O. Studied in the thin films form, they showed that it has a cubic structure with a lattice constant of 6.68Å and its energy band gap which depens on the thin film thickness (up to 100 nm) is in the range between 2.03eV to 2.17eV. The resistivity is in the range from 150 to 330 μΩ·cm. Ta_2O_3 was reported to crystalizes at orthorhombic β phase or exists in the amorphous state (65) while the crystal structure of metastable Ta_3O_9 is monoclinic (65).

2.6 Electronic structure of Ta-O system

In related literature, only a few items describing the electronic structure of the Ta-O system can be found. The one written by Ivanov et al. (83) considered δ- Ta_2O_5 , Perevalov et al. (84) concentrated on β- and δ- Ta_2O_5 crystal modification and Zacherle et al. (85) showed the result of DOS calculations for λ-Ta_2O_5. The δ- Ta_2O_5 with a hexagonal structure (P6/mmm) (83) has an indirect bandgap which is equal to 1.31 eV and conduction band minimum at the center of the Brillion zone (Figure 2.17)

However, the experimental value of the bandgap of amorphous tantalum pentoxide is much higher and reaches the value of 4.2 eV. The calculation of effective masses of holes

and electrons showed diverse values due to strong anisotropy along the single directions - the value for effective electron mass along Γ→A equal 0.3, but for Γ→M the value match 2.9. For the holes, effective masses depend on direction as follows for: A → Γ and A → L is 1.3 and 1.6, respectively. In this work the authors also showed results for the partial density of state (PDOS).

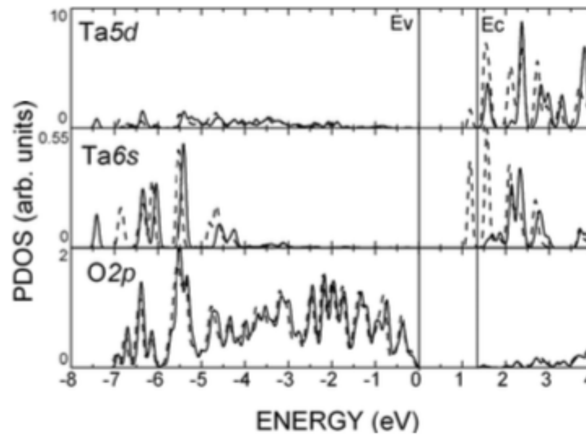

Figure 2.16 Partial density of the states of Ta and O atoms closet to the vacancy. Solid curve is marked ideal δ- Ta_2O_5; dashed curve δ- Ta_2O_5 with oxygen vacancy. Adapted from (83)

This calculation demonstrated the contribution of Ta 5d, 2s and O2p orbitals to the electronic structure of prefect δ- Ta_2O_5. The O2p orbital is formed/located mostly in an upper sub-band of the valence band with a small input of Ta5d states. However, Ta5d formed a conduction band with the addition of O2p states.

The situation is slightly different in δ- Ta_2O_5 with oxygen vacancies. In their considerations, Ivanov et al. (83) choose supercell with 168 atoms after 2x2x3 translation of the unit cell. They also removed one O atom with (0.5, 0.5, 0.5) coordinates in crystallographic axes. The PDOS calculation showed that oxygen vacancy causes a defect level in energy gap (Figure 2.16).

The defects level is related to the presence of Ta5d and Ta6s states in this band. They also have influence on effective masses of electron and holes. The oxygen vacancy gave an energy gain of 0.3eV for electrons and 1.75eV for holes. However, Perevalov and Shapashnikov (84) showed that oxygen vacancy led to instability of the adopted crystalline structure irrespective of the supercell size (Figure 2.18). Total electron density of state (TDOS) demonstrated that neutral oxygen vacancy formed single occupied defect level in the band gap, 2.6eV above the top of the valence band. Moreover, the position of the level is related to the presence of doubly coordinated oxygen vacancies. The same

authors presented calculations for β-Ta_2O_5. This orthorhombic crystal structure with 77 atoms contains TaO_6 octahedra and TaO_7 pentagonal bipyramids. In the calculation, at 14-atomic orthorhombic cell was used. The β-Ta_2O_5 is a direct-bandgap insulator with the dispersion maximum at Z point in Brillouin zone (84).

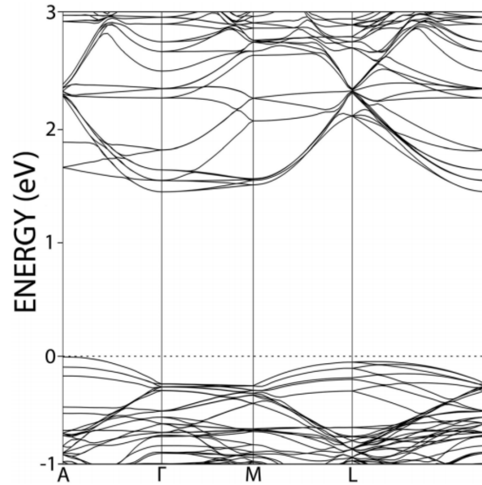

Figure 2.17 Band structure of δ-Ta_2O_5 along a few high symmetry directions in the irreducible Brillouin zone. (83)

The authors used two different functional, first, hybrid B3LYP which influences on bordering on lowering valence subband and increasing in the ionic gap. It has a given bang gap equal E_g=4.1eV. The second classical of calculations of GGA gave a lower result for calculated band gap. The E_g is equal 1.9eV. The PDOS calculations for this tantalum pentoxide - are the same as δ- Ta_2O_5. However, TDOS calculations of neutral oxygen vacancy -in β-Ta_2O_5 showed small changes compared to the defect-free structure. Furthermore, the doubly coordinated oxygen vacancy in the tantalum plane showed two levels in the band gap the lower which is occupied by electrons and upper which is empty. The triply coordinated vacancy in the tantalum plane formed a single occupied defect level above the top of the valence band in the band gap.

The Zacherle et al. (85) presented that Ta 5d, 6s and O2p orbitals have a contribution to the λ-Ta_2O_5 electronic structure. The optical band gap is equal 4eV and is located between the occupied O2p state and Ta5d unoccupied state. Pérez-Walton et al. (69) reported that the monoclinic phase of tantalum pentoxide (B-Ta_2O_5) is a semiconductor with a band gap equal $E_g^{PBEsol} = 3.1\ eV$ or $E_g^{HSE06} = 4.7\ eV$, where PBEsol and HSE06 are functionals. The VBM like B-Nb_2O_5, is located in Γ-point with gaps $E_g^{PBEsol} = 3.4\ eV$ and $E_g^{HSE06} = 5.0\ eV$,

while CBM is located along direction $\langle 2u, u, 0\rangle$. The DOS calculations for this structure showed that the valence band is built up from hybridization of Ta d-state and O p-state. In the VBM p-states dominate and arise mainly from O_2 and O_3 ions. However, the conduction band and CBM consist of mainly Ta d-state and arise from the Ta ions.

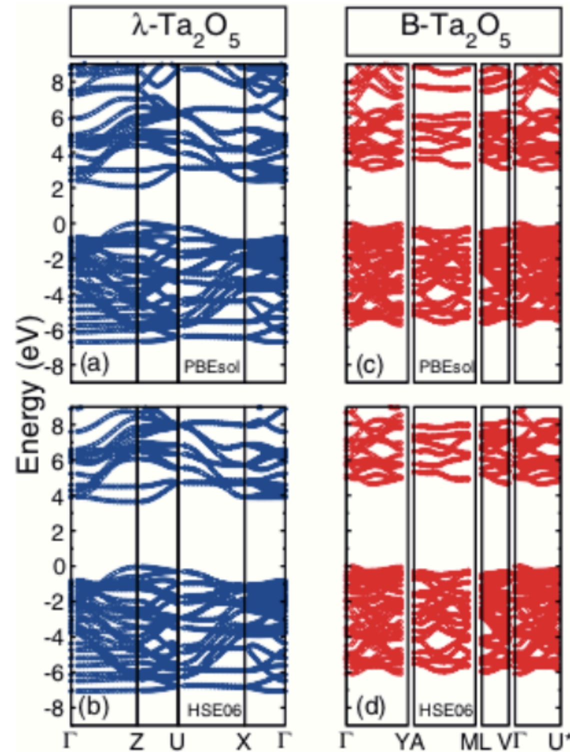

Figure 2.18 Calculated dispersion relation along the high symmetry directions of the irreducible Brillouin zone for λ-Ta2O5 with (a) PBEsol (b) HSE06 with (c) PBEsol (d) HSE06 for B-Ta_2O_5. The data was adapted from (84)

The calculation of electronic structure in the other non-stoichiometric phase of Ta_2O_{5-x} (85) is complicated. It depends on the structure, the local relaxation of the atomic arrangement around the defects or even on the charge of defects.

The last work of Zhu et al. (86) showed calculation results for stabile triclinic structured T-TaO_2 semiconductor with a band gap grater then then 1.0eV. However, this T-TaO_2 structure corresponds to disordered rutile type TaO_2 (R-TaO_2). The PDOS for this promising candidate for RRAM showed that the valence band mainly consists of localized overlapping of Ta-d and O-p state.

2.7 Defects in the Nb-O and Ta-O system

Defects have a significant influence on material properties. Generally, they are classified as points and extended defects (see Figure 2.19). More detailed classification of defects is presented in the figure below.

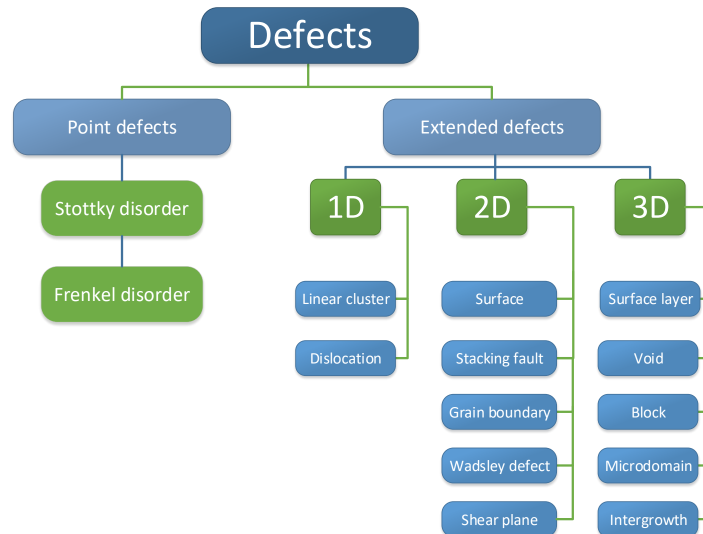

Figure 2.19 Classification of defects. - Classification of defects based on the topological criteria. The point defects are considered zero-dimensional (6)

2.7.1 Point defects

As we know, the perfect crystal does not exist in nature and if the imperfection is limited to one lattice or structural site and its immediate vicinity it is termed as point defect (87). Point defects are cation and anion vacancies and interstitials, which are in thermodynamic equilibrium and typically are present in all solids at temperature -273,15°C. A vacancy is an unoccupied regular lattice site, while an interstitial is an ion displaced from its lattice position into an interstitial site. Primary classification of point defects dividing them to intrinsic (native) and extrinsic (impurities/dopants) are described by general notation defined by Kröger-Vink. Their work describes their type, electronic charge and lattice position in reference to the perfect lattice (88). In the notation

$$\boldsymbol{M_S^C}$$

M is the atom e.g. Nb, Ta or O; **S** indicates the site that species occupied in the lattice; C means the charge. Also, this notation uses symbols like **e** to describe electron, **h** a hole, and **i** interstitial or **V** a vacancy. The negative charge is denoted by (ʻ) and positive by (•). The oxygen vacancy is marked

as $V_O^{\cdot\cdot}$ and niobium and tantalum vacancy as V_X'' (X = Ta or Nb).

In niobium and tantalum oxide the intrinsic ion disorder plays the main role. These defects are divided into two types of disorder:

- a defect characterized by displacement of cation from their regular lattice site into interstitial position is named a Frenkel disorder
- a defect corresponding to the formation of a stoichiometric amount of cation and anion vacancies (Schottky pair) in the solid is called a Schottky disorder

Many phases of Ta-O and Nb-O are described in literature (see point 2.5 and 2.3 of this chapter, respectively) but only a few are well characterised in terms of point defects. For example, the most investigated from the Ta-O system is the β-Ta_2O_5 due to its high-k-dielectric in metal – oxide - semiconductors transistors (88-90). The defect chemistry described oxygen vacancies in this oxide are as follows:

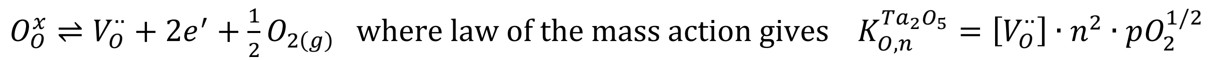

$O_O^x \rightleftharpoons V_O^{\cdot\cdot} + 2e' + \frac{1}{2}O_{2(g)}$ where law of the mass action gives $K_{O,n}^{Ta_2O_5} = [V_O^{\cdot\cdot}] \cdot n^2 \cdot pO_2^{1/2}$

$O_O^x \rightleftharpoons O_i'' + V_O^{\cdot\cdot}$ where law of the mass action gives $K_F^{Ta_2O_5} = [O_i''][V_O^{\cdot\cdot}]$

where pO_2 *is* oxygen partial pressure, n concentration of electrons.

The intrinsic electronic disorder in the β-Ta_2O_5, where the electron is transferred from valence band to conductive band, correspond to formation of electron-hole pairs and is described by the equation:

$nil \rightleftharpoons e' + h^{\cdot}$ where the law of mass action gives $K_B^{Ta_2O_5} = n \cdot p$

However, in low oxygen partial pressure (pO_2), electron concentration varies with oxygen partial pressure, thus

$$n = \left(2K_{O,n}^{Ta_2O_5}\right)^{1/3} pO_2^{-1/6}$$

The electron concentration in reduction condition also influence small acceptors impurities like e.g. Al^{3+}, Cr^{3+}, Fe^{3+}, Sc^{3+} (91). Hence,

$$n = \left(\frac{K_{O,n}^{Ta_2O_5}}{[A_{Ta}'']}\right)^{1/2} pO_2^{-1/4}$$

where A_{Ta}'' is acceptor impurities.

At higher pO_2 values, the conductivity is pO_2-invariant, meaning that the oxygen vacancies are the majority of mobile charge defects, whereas, under oxidizing conditions, the increasing conductivity with increasing pO_2 point toward p-type conductivity resulting from (88):

$$n = K_B^{Ta_2O_5} \left(\frac{K_{O,n}^{Ta_2O_5}}{[A_{Ta}'']} \right)^{1/2} pO_2^{1/4}$$

Similar behaviour of oxygen vacancies is observed in the Nb-O system. However, Kurmaev et al. (41) showed that in nature the NbO consist of 25% structural vacancies. Other works (44,92-94) consider stoichiometric and nonstoichiometric Nb_2O_5. In stoichiometric H-Nb_2O_5 at a lower temperature, the defect concentration varies as $pO_2^{-1/4}$ but in nonstoichiometric, H structure is equal $pO_2^{-1/6}$ at lower pressure. Moreover, Hutchison et al. (95) and Anderson et al. (94) for N-Nb_2O_5 and H-Nb_2O_5, respectively, showed that not only oxygen vacancies but also Nb ions have influence on point defect in these structures. Furthermore, the interstitial tetrahedral Nb, can thermodynamically affect structure Nb_2O_{5-x} as follows:

$$Nb_{Nb} + {}^{5}\!/_{2}\, O_o \rightleftharpoons Nb_i^n + ne^- + {}^{5}\!/_{2}\, O_o$$

where x in the structure relates to oxygen partial pressure $x \propto pO_2^{-5/4(n+1)}$.
Temperature reduction conditions not only have influence on the pressure but also strictly affect the conductivity. Hence, its relationship is expressed by

$$\sigma = \sigma_0 exp\left(-\frac{E}{RT}\right)$$

where E is related to the heat of formation of vacancies, and the ionization energies of trapped electrons, σ_0 includes currier mobility μ, which in semiconductors relates to temperature by relationship $\mu = \mu_0 T^{-n}$. In this equation n is contains with value between 2 to 3.5 (92). The carrier concentration $[e^-]$, under limiting condition can be given by

$$[e^-] = (K_0 K_{01})^{1/2} pO_2^{-1/4} exp\left(-\frac{\Delta H_V + E_1}{2RT}\right)$$

or

$$[e^-] = (K_0 K_{01} K_{02})^{1/3} pO_2^{-1/6} exp\left(\frac{\Delta H_V + E_1 + E_2}{3RT}\right)$$

ΔH_V represent the heat of formation of oxygen vacancies, E_1 and E_2 represent ionization energies on the first and second trapped electron, K_0,K_{01}, K_{02} are the pre-exponential factors for K, K_1 and K_2 connected with low of mass action as follows:

$K = [O_o] \cdot pO_2^{1/2}$, $K_1 = \frac{[O_o^{\cdot}] \cdot [e^-]}{[O_o]}$, $K_2 = \frac{[O_o^{\cdot\cdot}] \cdot [e^-]}{[O_o^{\cdot}]}$ and their temperature dependence $K = K_0 exp\left(\frac{-E}{RT}\right)$.

2.7.2 One-dimension defects

In natural crystals, a linear change in the structure is also observed. It is called dislocation (Figure 2.20). They can deform all or partial structure of crystal on the edge, screw it or mix both (Figure 2.21). One-dimension defects also have relevant influence on mechanical properties, particularly on metals and at high temperatures.

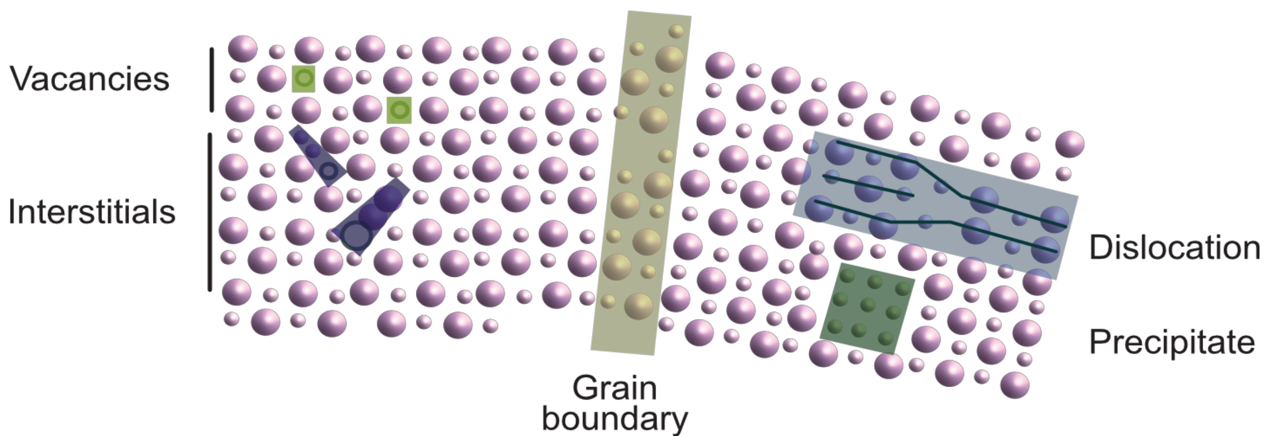

Figure 2.20 Schematic two-dimensional representation of some of the defects present in a solid of this type metal oxide(88)

Works describing dislocation in Ta-O and Nb-O systems are extremely rare. Michaelis (96) mentioned that in amorphous phase the Ta/Ta_2O_5 in a thin film formed dislocation. However, more detailed studies have shown that nucleation formed Ta/Ta_2O_5 structure related to 2D defects like grain boundaries (96). Shindo and Kamatsu (38) showed that density of dislocation in $H\text{-}Nb_2O_5$ single crystal along then [001]-axis equal $2.4 \cdot 10^5$ cm^{-2}.

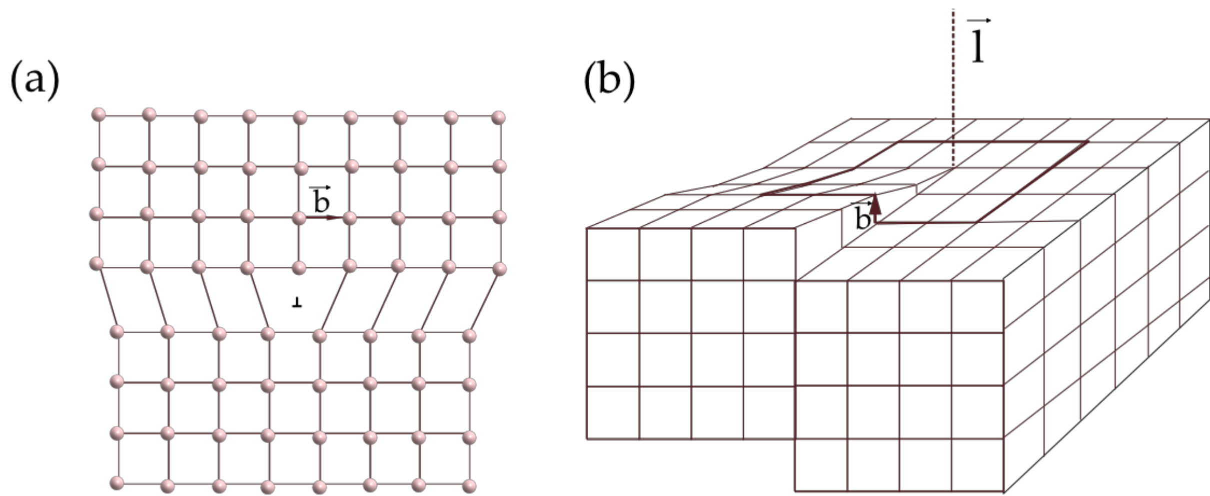

Figure 2.21 Simplified representation of (a) an edge dislocation with ℓ⊥b and (b) a screw dislocation with ℓ||b. (88)

2.7.3 Two- dimensional defects

In literature, equally with point defects, surface defects are the most intensively studied by microscopic techniques. In the Nb-O and Ta-O system interface between homogeneous regions of material defects like grain boundary, Wedsley, shear plane and stacking fault are formed. However, as mentioned above, for Ta-O few publications consider only one point and two-dimensional defect, while for the Nb-O system several works were noted. From this point of view, this part of the thesis will only consider niobium oxides.

2.7.3.1 Shear plane

The shear plane is observed in a crystal when the crystal plane is shifted relative to its neighbouring crystallography plane. In Nb_2O_5 and NbO_2 which are derived from ReO_3 structural type, where NbO6 octahedra are linked, a typical oxygen atom is observed. However, the most common are in reduced H-Nb_2O_5 which are related to $Nb_{28}O_{70}$, $Nb_{25}O_{62}$ and $Nb_{12}O_{29}$. (93). It is also worth mentioning that orthogonal shear plane in e.g. H-Nb_2O_5 can be arranged as in Figure 2.22 and their crossroads can create blocks. This corresponds to the block structure which is described in more detailed in point 2.7.3.3.

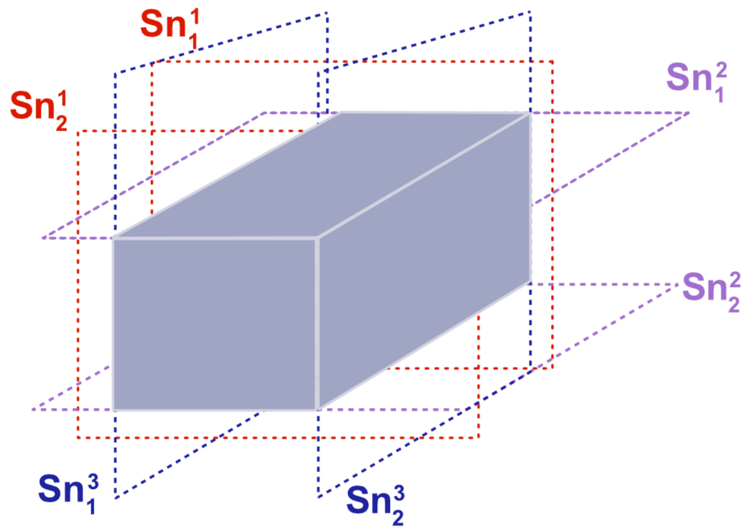

Figure 2.22 In contrast to TiO_2 the accumulation of oxidase vacancies for Nb_2O_5 have been observed in three orthogonal directions. Along the plane in three orthogonal directions means these planar defects (Wadsley defects) upper crossing, together create a block structure.

2.7.3.2 Stacking faults

These defects are related with the sequence of lattice planes in a crystallographic structure. Any disorder in the sequence of atoms is called stacking faults. Nimmo et al. (93) reported that such defects are observed in $Nb_{39}O_{97}$ (Figure 2.23) from ideal DCDCDC.. structure to DCDCDCCDCDCCDCCDCDCDC… . However, Iijima (44) showed that an ideal H-Nb_2O_5 structure could be expressed by A and B sequence model, where A is the block row of 3x4 blocks, and an ideal sequence looks like ABABAB… . Figure 2.24 is presents defect sequence BAAAB marked by a yellow frame. This structure is expressed by 3x4 blocks which correspond to a $WNb_{12}O_{33}$ structure which is known as one of H-Nb_2O_5 structures (Figure 2.24).

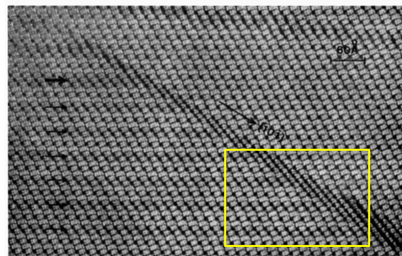

Figure 2.23 Two-dimensional lattice image showing an interaction between the defect of A and C (44)

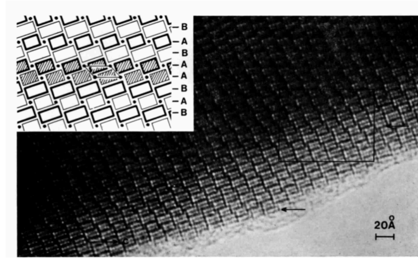

Figure 2.24 Two-dimensional lattice image of H-Nb_2O_5 showing the defect of type A parallel to the c axis. Insert correspond to the enclosed area. (44)

2.7.3.3 Wadsley defects and block structure

A surface with ordered arguments in one distinguished plane in which mistakes occur in regular spacing in such a plane are called Wadsley defects. They are observed in nonstoichiometric niobium oxide. This was first reported by Iijima (97) in $Nb_{12}O_{29}$, $Nb_{22}O_{54}$ and $Nb_{29}O_{62}$. This structure is closely related to H-Nb_2O_5 (Figure 2.25 and Figure 2.26). This defect in this oxide tends to appear in pairs or groups with regular spacing in a matrix lattice. Moreover, this defect in a structure makes the overall composition of the specimen oxygen deficient. Iijima (97) also observed that a higher concentration of Wadsley defects is connected with the degree of oxygen deficiency.

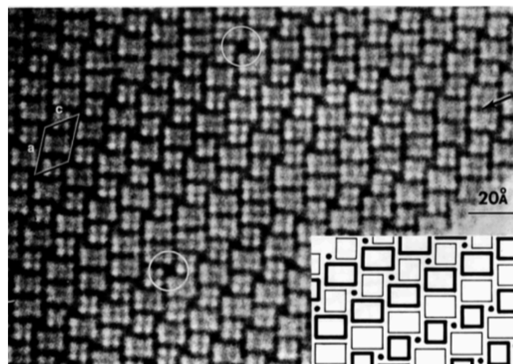

Figure 2.25 High-magnification lattice image showing the $Nb_{12}O_{29}$-type Wadsley defect (indicated by arrow). Some of the tetrahedral sites show darker contrast than others, suggesting metal-atom vacancies (97).

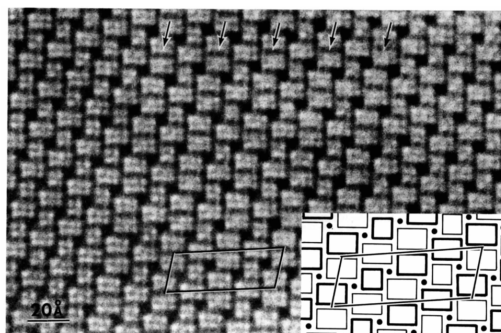

Figure 2.26 An ordered intergrowth o the $Nb_{29}O_{62}$ –type Wadsley defects (indicated by arrows) into the host structure. The region forms a superstructure having a composition of $Nb_{47}O_{116}$. The unit cell is outlined. (97)

2.8 Electronic transport

Electronic transport in crystal and thin film is a large and complex field. At this point in only two aspects will be presented: charge carrier transport and electrical conduction.
Carrier transport is a broad topic that encompasses both traditional bulk processes and low dimensional, quantized structures.
Niobium and tantalum oxides' dependence of their structure is as an insulator, semiconductor or conductor.

2.8.1 Electronic transport in niobium oxides

The most studied of the niobium oxide system is Nb_2O_5. Kofstand's previous work (92) describes the electrical behavior of α-Nb_2O_5 connected with various temperature conditions. This oxide was annealed at a temperature range from 750°C to 1200°C. The characteristic change to the n-type semiconductor of α-Nb_2O_5 at 1000°C - 1100°C was noted.

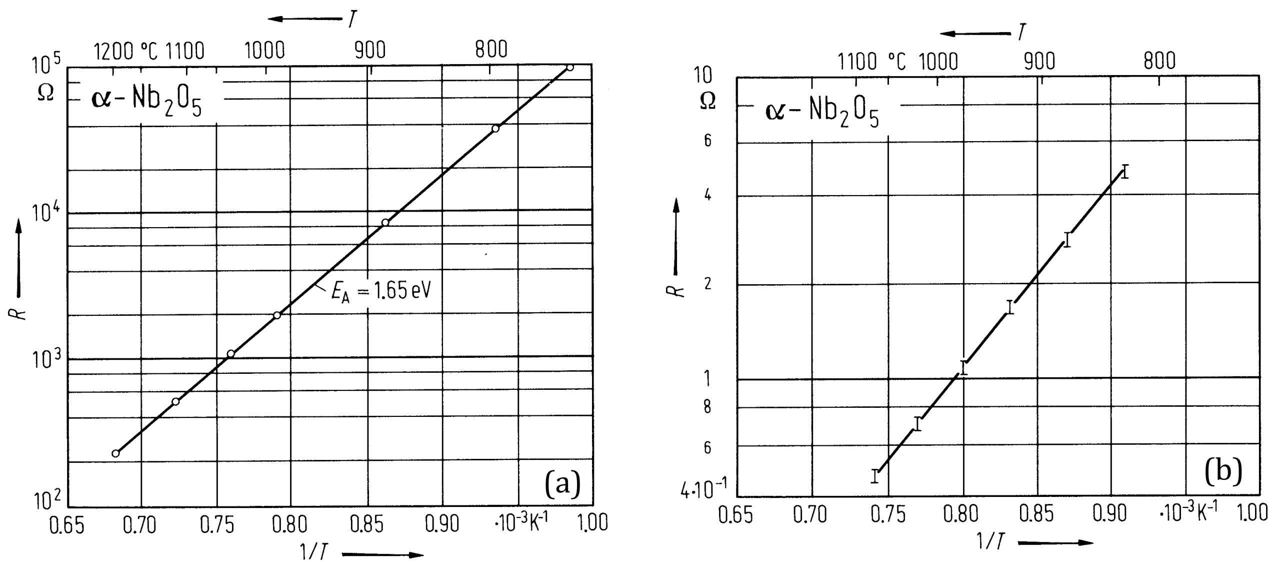

Figure 2.27 The logarithmic of electrical resistance of α-Nb_2O_5 as a function of reciprocal temperature (a) at 1atm ($pO_2^{-1/4}$ region); (b) $pO_2 = 10^{-13}$ atm ($pO_2^{-1/6}$ region) (92)

The linear resistance changes observed at the region $pO_2^{-1/4}$ increases with temperature (Figure 2.27a) and their activation energy is equal to E_A= 1.65 eV. However, in the region $pO_2^{-1/6}$ thermogravimetry studies have shown that in this region activation energy increases almost three times (E_A=4.44 eV) for the formation of doubly ionized oxygen

vacancies. Kofstand also showed that actual conductivity in this region has lower activation energy (Figure 2.27b), where carrier mobility can be expressed by relationship $\mu \propto T^{-3}$ (Figure 2.29). According to another literature position (98) in H-Nb_2O_5 activation energy for the region $pO_2^{-1/4}$ is much higher than observed by Le Brusq et al. (98) and equal E_A= 3.10 eV with slightly activated mobility $E_A(\mu) \approx 0.10 eV$ and $\mu(1100°C) \approx 0.10\ cm^2/V \cdot s$.

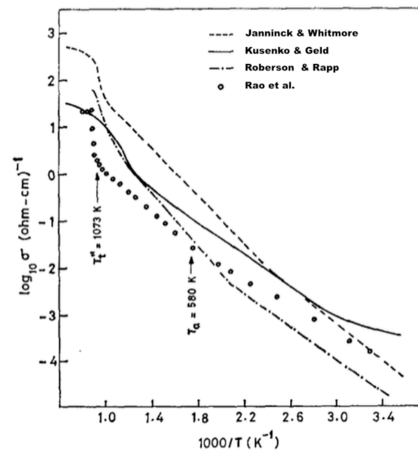

Figure 2.28 Four probe conductivity data on NbO_2 (29)

Another situation is observed for n-type semiconductor NbO_2 (99). The mobility of the conduction electron and hole equal $E_A(\mu_e + \mu_h) \approx 0.43 eV$ and electron and hole mobility were $\mu_e + \mu_h \approx 62\ cm^2/V \cdot s$. Rao et al. (29) showed that this energy depends on temperature close to that presented by Robertson and Rapp(99) and equal $E_A(\mu) \approx 0.45 eV$ at 300 $°C$ (Figure 2.28).

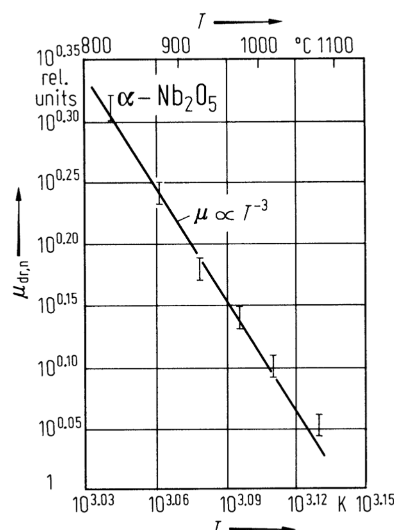

Figure 2.29 Temperature dependence of electron drift mobility for α-Nb_2O_5 at $pO_2 = 10^{-13}$ atm (92)

Bélanger et al. (100) showed that resistivity in rutile-type NbO_2 a single crystal, dependent on a crystal plane, that their conductivity changed at 800 $°C$. The oxide below this temperature is a semiconductor while above this temperature the conductivity character changes depending on crystal direction. In direction a, it was a semiconductor and after rotation to c direction, NbO_2 indicated metallic-like character (Figure 2.30). The activation energy in both cases were almost the same and equal $E_A \approx 0.45eV$. However, in the nanoscale, NbO_2 is also observed as a sublayer with metal-insulator-metal (MIM) structure. Slesazeck et al. (101) reported that between two platinum electrode and niobium pentoxide, NbO_2 layer energy activation was $E_A = 0.215eV$ while applied low potential equal $v_m = -0.5\ V$.

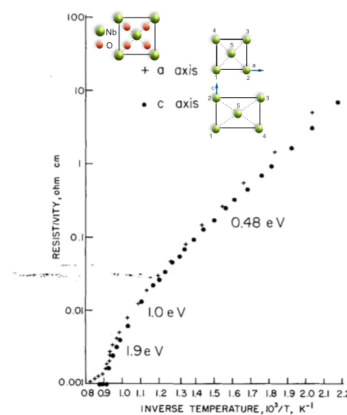

Figure 2.30 Resistivity as a function of temperature for current parallel to the crystallographic axis a and c (projection of structure left corner of picture) (100).

2.8.2 Electronic transport in tantalum oxides

Several articles have described electronic transport in tantalum oxides. Kofstad also observed changed of the conductivity of Ta_2O_5 with temperature like Nb_2O_5 (87,192). The oxide behaviour changes linearly from an n-type semiconductor to p-type with increasing pO_2. Stroud et al. (102) showed that in polycrystalline Ta_2O_5 between 900$°C$ -1400$°C$ electron motilities equal $\mu(1100°C) \approx 0.05\ cm^2/V \cdot s$ at $pO_2 = 10^{-16} atm$. The Seebeck coefficient determined by thermocouple $Pt_{30}Rh$ attached to the end of samples suggest motion of electron in a very narrow conduction band (103) (Figure 2.31). Also, Stroud et al. presented that minimum conductivity correspond to equilibrium between electron acceptor atoms (n-type) and holes electron (p-type) then activation energy for electron conductivity is $E_A = 1.8eV$.

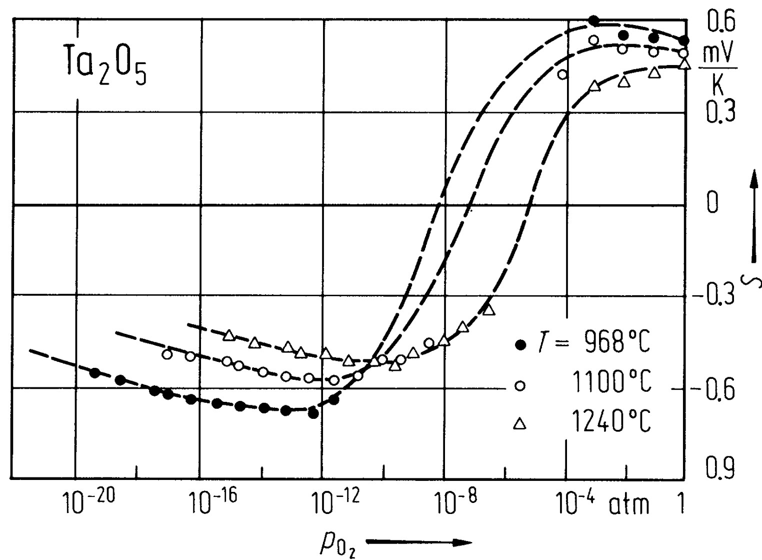

Figure 2.31 Seebeck coefficient obtained in various oxygen pressures at 968°C, 1000°C, 1240°C (102)

2.9 Resistive switching

The 21st century is known as the information age. It would not have happened without the development of computer technology and the Internet. It was 1945 when von Neumann first presented, an architecture model that computing and memory units are separated and connected via buses through which computing data and instruction code are transported between processor and memories (104). Although all these processes consume energy, which effect gives less power to actual computing operation in our computers. This effect is known as the "von Neumann bottleneck" (104). Hence many researchers have worked for a solution, proposed new computer architecture or presented alternative approaches. One 'non-von Neumann' type architecture, based on the resistivity switching (RS) phenomena is called "iMemComp". This new solution was proposed by Li et al. (104). The authors proposed that architecture can be used by the unified core to make both memory ("Mem") and computing ("Comp") tasks with the capability of parallel computing, learning and memorizing ("intelligent") user-defined logic function. The "iMemComp" is constructed on a sandwich-like emerging device, called RS devices, whose resistance can be modulated via applying external voltage. It uses nonvolatile memory and Boolean logic functions to allow parallel computing and logic learning.

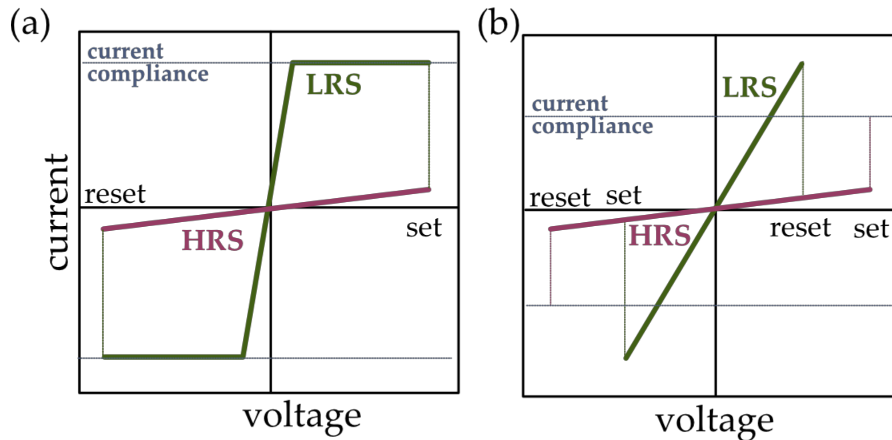

Figure 2.32 Two basic type of resistivity switching phenomena (a)bipolar switching – there is a difference in polarity, the SET voltage is one polarity of voltage while RESET operation request the opposite polarity and (b) unipolar switching – there is no difference in polarity, the SET voltage is always higher than the RESET (105)

However, this idea of a new computer model did not first arise in the minds of Li et al. (104) if in 1962 when Hickmott (1) first observed resistivity switching phenomena in thin film Al/Al_2O_3/Al. Since that time, this effect is has been intensively studied in metal oxides such as TiO_2 (106,107), Nb_2O_5(10,108), Ta_2O_5 (109), VO_2(110), Fe_2O_3(111), $SrTiO_3$ (112), $SrZrO_3$(113), $BaTiO_3$(114), $LaMnO_3$ (115) and many more. The metal-insulator sandwiches indicated that the resistivity switching phenomena is a promising candidate for a new type of nonvolatile memory called ReRAM whereby the RS effect is controlled by the current magnitude or voltage bias polarity. However, a consistent model describing the phenomena still does not exist. There are several different mechanisms changing resistivity in a non-volatile way (Figure 2.32) and related with I-V curves – bipolar and unipolar switching (105,116). However, the origin of resistivity switching effect on a nanometer scale takes place through ionic transport and redox-reaction mechanisms (105). Nevertheless, at this point is worth mentioning that the mechanism occurrence of RS phenomenon is related to oxygen dislocations in oxide material.

Szot et al. (3) showed that by using a local conductivity atomic force microscope (LC-AFM) (Figure 2.33) in nanometer size areas the switching was locally and by applying an appropriate switching voltage with an AFM tip, a few nanometers areas can be switched between 'ON' and 'OF' states. These areas correspond to existing dislocations in the materials and the oxygen is transported along them which can be an easy diffusion path and driving force for resistivity switching.

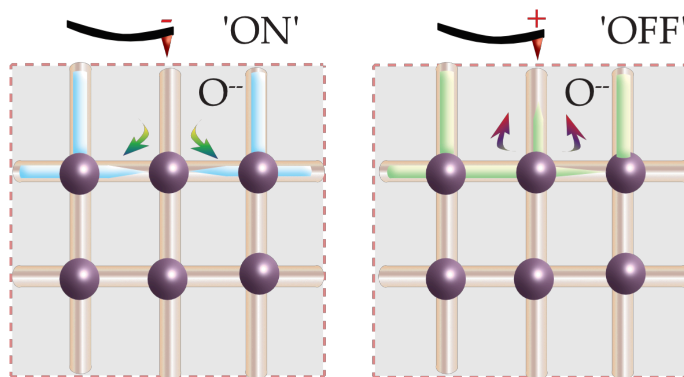

Figure 2.33 The part of SrTiO3 single crystal. Adapted from Szot et al.(3).

In general, three different major mechanisms could be identified such as electrochemical metallization mechanism, thermochemical mechanism and valence change mechanism which relate to redox processes (Figure 2.34).

In this thesis, only mechanisms closely correlated with Nb-O and Ta-O systems will be only considered.

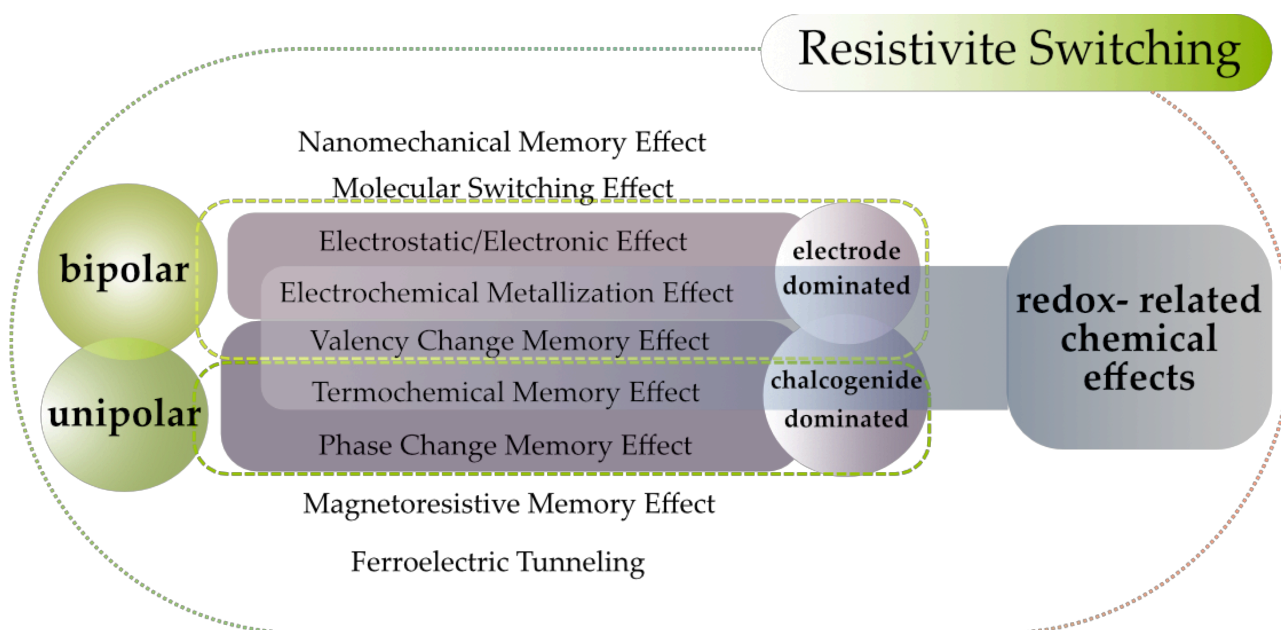

Figure 2.34 Summary of the resistive switching mechanism. Classification of the most common RS driving mechanism. The classes in the center are especially interesting, since those are related to the redox chemical effect (105).

2.9.1 Resistive switching in Nb-O system

The character of resistive switching in metal oxide is grouped into two categories: unipolar and bipolar (105,117). The mechanism effect is diverse. Many models propose oxygen diffusion (3), Schottky barrier behaviour at the metallic contact interface, charge trapping/de-trapping (108) or the creation of crystalline defects (108). However, most of

the niobium oxide exhibit unipolar resistivity switching. This is based on the filament model (Figure 2.35) where a conductive channel called a filament is formed in insulating oxide if a critical voltage is applied across it.

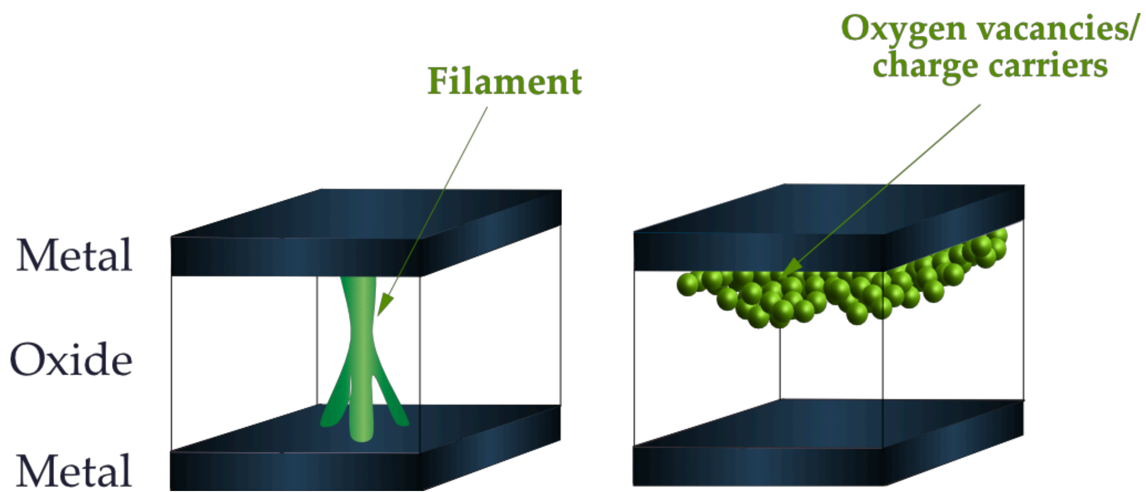

Figure 2.35 Two types of conductive paths responsible for resistivity switching according to Sawa (12,104). Left filament type, right interfacial type(12,118)

However, first the conductive filament must be produced in an electroforming step as a soft breakdown in the dielectric material. The switching process occurs by rapture and re-formation of the filaments (3,108). In the niobium oxide, RS depends on applied electrodes, forming and the growth film method (119). For example, Jung et al. (119) presented that amorphous NbO_x grown on $Pt/SiO_x/Si$ substrate by Pulsed Laser Deposition (PLD) indicated a unipolar type of RS. However, after the forming process, as a result of the presence of electrically-induced channels two metallic oxides, NbO_2 and Nb_2O_5 are created on the thin film surface. In another work Jung et al. (122) showed that the electroforming process changes the film dramatically, inducing metallic nanostructures (nanochannels). Bae et al. (120) presented that different thicknesses induce different RS phenomena. The NbO_x between platinum electrodes with a thickness less then 45nm showed the typical unipolar character of RS, but thicker NbO_x film showed mono-stable threshold switching behaviour. Nevertheless, this effect depends on the amount of applied voltage. If it is increased from 2.5V to 3.5V the mono-stable RS behavior transform to bi-stable. Recently, Kim et al. (121) reported that switching power in $Pt/Nb_2O_5/Pt$ decrease increasing switching resistance. They also showed that the RESET process (Figure 2.32) (low- resistance state (LRS) → high-resistance state (HRS)) can be described in the framework of the conductive filament model, or vice versa, the observed power universality proves the existence of typical behavior in the filament model. The

SET (HRS→LRS) process, a similar low-power reaction between switching power and resistance is observed, but it is found that larger electrical power is needed, by as much as one order of magnitude at a similar switching resistance. Another interesting work by Jung et al. (122) showed that current-voltage characteristic in unipolar type RS by using Schottky emission, Frenkel-Pool emission and Ohmic conduction was modeled (Table 3). However, using WO_{3-x} interface in a RS device can easily prevent localization of filament position after the "forming" process.

Process	Expression	Voltage and temperature dependence
Schottky emission	$J = A^{*}Texp\left[\frac{e\left(\phi_B - \sqrt{eE/4\pi\varepsilon_i}\right)}{kT}\right]$	$\sim T^2 \exp\left(\frac{a\sqrt{V}}{T} - \frac{e\phi_B}{kT}\right)$
Frenkel-Poole emission	$J \sim Eexp\left[\frac{e\left(\phi_B - \sqrt{eE/4\pi\varepsilon_i}\right)}{kT}\right]$	$\sim V \exp\left(\frac{2a\sqrt{V}}{T} - \frac{e\phi_B}{kT}\right)$
Ohmic conduction	$J \sim Eexp\left[\frac{-\Delta E_{ae}}{kT}\right]$	$\sim V \exp\left(\frac{-c}{T}\right)$

Table 3 Leakage conduction mechanisms in metal/oxide/metal structures where J: current density, A^*: effective Richardson constant, Φ_B: potential barrier height, E: electric field, e: electron charge, ε_i: oxide permittivity, d: oxide thickness, ΔE_{ae}: activation energy of electrons, $a \equiv e/(4\pi\varepsilon_i d)$. (122)

Nevertheless, in the niobium oxide system bipolar type of RS is also observed. This interfacial type of RS takes place in a particular extended area at the interface between electrode and oxide (Figure 2.35). The electrochemical migration of oxygen vacancies, trapping of electron and holes or charge-induced Mott transition at the active interface could be responsible for this RS process. Bipolar type of RS was also observed in Nb_2O_5 obtained by atomic layer deposition (ALD) between TiN/Ti and $Pt/SiO_2/Si$ electrodes (123). Chen et al. (123) reported that at room temperature such designed nonvolatile memories are stable and can be read with $5 \cdot 10^4$s. Hanzing et al. (124) showed that nonstoichiometric Nb_2O_5 which show reproducible bipolar RS could be formed through the formation of MIM stacks by DC magnetron sputtering.

2.9.2 Resistivity switching in the Ta-O system

Besides $SrTiO_3$, tantalum oxides are the most investigated systems as a possible material for stable nonvolatile memory devices. This oxide indicates both type of resistivity switching, the same as Nb-O. Most research work on RS in the Ta-O system has been devoted to optimization of the switching characteristic (4,9,80,125-145). The first report with promising parameters for application as nonvolatile memories was shown by Lee et al. (4). Their work presents stable and low RESET current through crossbar array using an intrinsic Schottky barrier to suppress leakage of current. It is worth mentioning that the Schottky barrier depends on the bending of an energy band at the interface that is of the size/value of Fermi energy, in the n-doped semiconductor when it is brought in contact with metal leading to the formation of a space charge layer at the interface (12). However, this model describes an idealized situation where two contacting materials have homogenous bulk properties. Hence materials, like oxides (with surface defect) at the Fermi level are pinned at the interface a forming so-called Bardeen barrier and cannot be adjusted by band bending (12) in the metal-semiconductor interface as they are very complex and many parameters would need to be taken a model to work correctly.

Another interesting feature presented in the work of Lee et al. (4) is related to the plasma-oxidized bilayer in Pt/Ta_2O_{5-x}/TaO_{2-x}/Pt which leads to superb endurance, retention and speed by localizing the RS phenomena. The endurance of this RS device was 10^{12} for 30x30μm cell size. Furthermore, Park et al. (146) have shown filamentary and bipolar character of RS in a Pt/SiO_2/a-Ta_2O_{5-x}/a-Ta_{2-x}/Pt-based ReRAM device using an in-situ probing method inside a transmission electron microscope (TEM). They showed that the current flow is perpendicular to the exchange of oxygen vacancies due to the Soret effect (thermophoresis). The dominant role of the filament was also observed by He et al. (89) for the Pt/Ti–Ta_2O_5/Pt system. The Ta_2O_5 doped by Ti have an influence on RS parameters. The RS ratio is higher, and Ti suppressed migration of oxygen vacancies via formed inactive Ti/O^- vacancy complex. The crucial role of the Ti layer was also found by Rahaman et al. (79) in the Al/Cu/Ti/TaO_x/W system. The authors showed that the Ti layer could control formation/dislocation in Cu nanofilament. However, it also can be controlled using defective high-κ TaO_x solid electrode. The Ti layer influences the period of data storage. This extrapolated time of data storage is 10 years. Recently, Lee et al. (109) demonstrated insulating frame Ta/Ta_2O_{5-x}/Ta or Pt/amorphous TaN/ Pt in Pt/Ta_2O_{5-x}/Ta/Ta_2O_{5-x}/Pt effect on reading margin, on/off ratio and improved selectivity

without reliability degradation. This complementary resistive switching (CRS) structure indicated the bipolar type of RS. Furthermore, Yoo et al. (80) showed that application of a thin stoichiometric Ta_2O_5 layer inside Pt/TaO_x/Pt cell could change the nature of resistivity switching from unipolar to bipolar. However, not only dopants or insulating frame have an impact on RS in tantalum oxides. Kim et al. (147) have shown for TaO_x a relation between the oxygen pressure during film preparation and switching properties. Xiao and Watanabe (81) presented that oxygen vacancy strongly influences RS in amorphous TaO_x. Their molecular dynamic simulation of heterostructure Pt/a-TaO_x/Pt revealed the conductive nature of Ta-Ta bonding and indicated that different oxygen vacancy concentrations influence intrinsic conductivity in a-TaO_x.

2.10 Application of Nb-O and Ta-O systems

Due to the vast potential of applications of niobium, tantalum and their oxide, they find a significant role in daily life. Among others they are applied to pacemakers, pipes and steel implants. Pure Ta is also a substance used in surgical clips, lumbar implants to stabilize the spine as well as aircraft turbines The Nb-Ti alloys are used as superconductive magnets applied in Magnetic Resonance Imaging (MRI). The Ta-C alloy is applied to cutting tools, while Nb-O is used in lenses, ceramics capacitors and acoustic wave filters. The Nb_2O_5 and Ta_2O_5 are used in sensors, optical and microelectronic devices, and tantalum pentoxide is also used in X-ray instruments. It is also worth noting that the tantalum and niobium oxides thin foils are used by jewelers.

Importantly, as mentioned in this chapter, further application of these oxides can be expanded to the field of electronic industry as a new type of nonvolatile memories.

3. Experimental methods

Due to the large number of experimental methods, only a few were carefully chosen to investigate the complicated structure of samples. Therefore, this chapter briefly describes and characterizes the methods involved.

3.1 X-ray photoemission spectroscopy

X-ray Photoemission Spectroscopy (XPS), which is also called ESCA (Electron Spectroscopy for Chemical Analysis) is a commonly used surface sensitive analytical technique (148,149) which works in an ultra-high vacuum environment. This primary, non - destructive method of surface physics provides accurate qualitative elemental analysis (for almost all elements except H and He) as well as quantitative composition and ability to determine chemical the state (binding and oxidation) of outermost layers of solid materials. The information from 1-5 nm from the top of samples surface with high precision (approximately equal 0.1% at.) is collected. XPS was developed by Kai Siegbahn in 1954 (148). It is based on the photoemission effect, which leads to the excitation and emission of the electron from a surface by soft X-rays upon irradiation with photons (Figure 3.1).

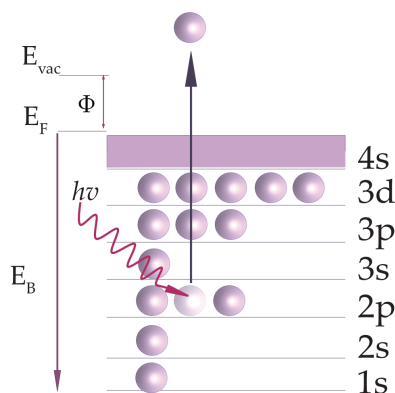

Figure 3.1 Photoexcitation from the energy level.

If X-ray energy is large enough, photoelectrons are expelled from the atomic electron shells, the kinetic energy (E_{kin}) of emitted photoelectron is measured by the analysis and detection system. The Physical Electronics PHI 5700/600 system, where photoelectrons

were excited by monochromatized Al Kα (1497 eV) radiation was used. The unique energy detected for a particular element from a surface region is identified based on binding energy (E_B) and is measured relative to the Fermi level (E_f) of the individual atoms. The relation between E_{kin} and E_B is as follows

$$E_{kin} = hv - \Phi - E_B \qquad (3.1)$$

where hv represents the energy absorbed by a photon and Φ is work function of the spectrometer.

The typical measurements of the survey spectrum, core level spectra or valence band of a sample is made in an ultra-high vacuum at about 10^{-10} Torr. This condition allows investigation of the sample surface with the absence of environmental impurities. The sample exposed to monochromatized X-ray and ejected electrons with E_{kin} during the photoemission process are focused on a hemispherical electron energy analyser and measured by detector (149) (Figure 3.2).

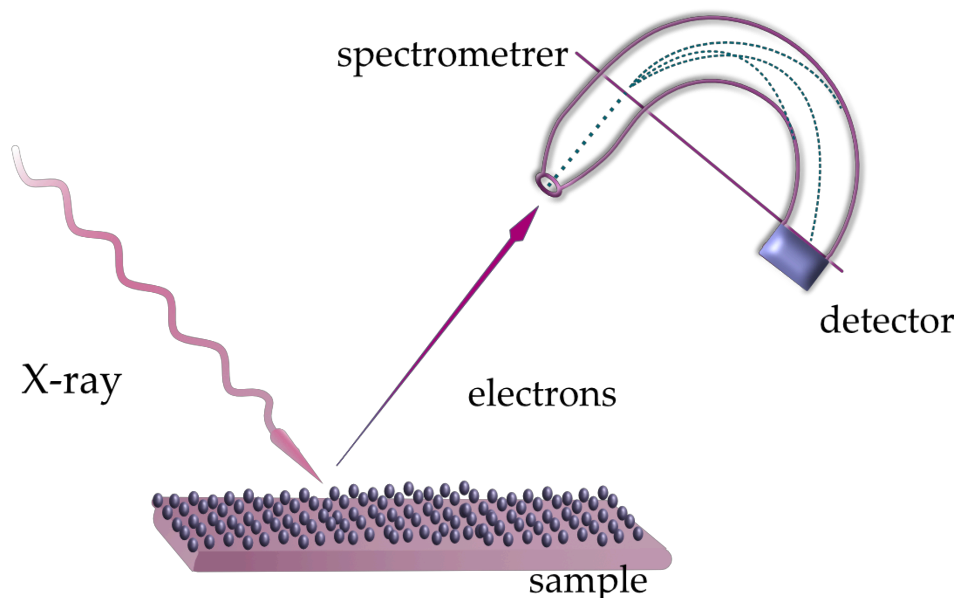

Figure 3.2 Schematic of the XPS spectrometer. Adapted from (12)

However, in order to avoid a charging effect in insulating samples, a flood gun is used. It compensates the charge of the sample surface by low energy electrons. The simplified

schematic setup for XPS experiment is shown in the Figure 3.2. The collected spectrum is divided in peaks which consist the core levels and valence band. Typically, analysis of core level, peak shape lines gives information about the electronic structure, oxidation state and chemical bands on the surface of analysis material. Furthermore, the elemental analysis of core-level spectra can give qualitative and quantitative information about the surface sample composition. The Valence band peaks analysis delivers information about the local environment of molecules interaction and chemical banding. Moreover, this analysis provides a designation of the value of the band gap and allows to investigate the electronic structure close to Fermi level (148).
All XPS spectra were shifted with respect to carbon C *1s* line at 284.6 eV and corrected for the background signal using the integrated Shirley algorithm. The bands were fitted by a composition of Gaussian and Lorentzian lines using MultiPak software.

3.2 X-ray diffraction method

X-ray diffraction (XRD) is a non-destructive method used to obtain information about the crystal structure of characterized material. This method was discovered in 1912 by Max von Laue and is used to investigate solid material. The experiment starts when X-rays are generated by a cathode X-ray tube. Next, it is filtered to produce monochromatic radiation and such beam is later collimated and directed towards the sample. The interaction of the incident X-rays (Figure 3.3) with the sample produce a constructive interface and diffracted ray when Bragg's law is fulfilled

$$n\lambda = 2d_{hkl}\sin(\theta) \qquad (3.2)$$

where n is an integer, λ is the wavelength of the X-ray radiation, θ is the diffraction angle between the incident beam and lattice plane, and d_{hkl} is the distance between lattice plane labelled by Miller indexes hkl in the crystal (11,12).
All results presented in this thesis were obtained with the use of two different PANalytical Empyrean diffractometers in Chorzów, Poland and at the University du Main in Le Mans, France. A Cu K_{α} X-ray tube was used. The experiments, including characterization of both

single crystal and thin films were done using Bragg Brentano geometry. Incident and reflected angles are identical relative to normal of the sample surface (Figure 3.3).

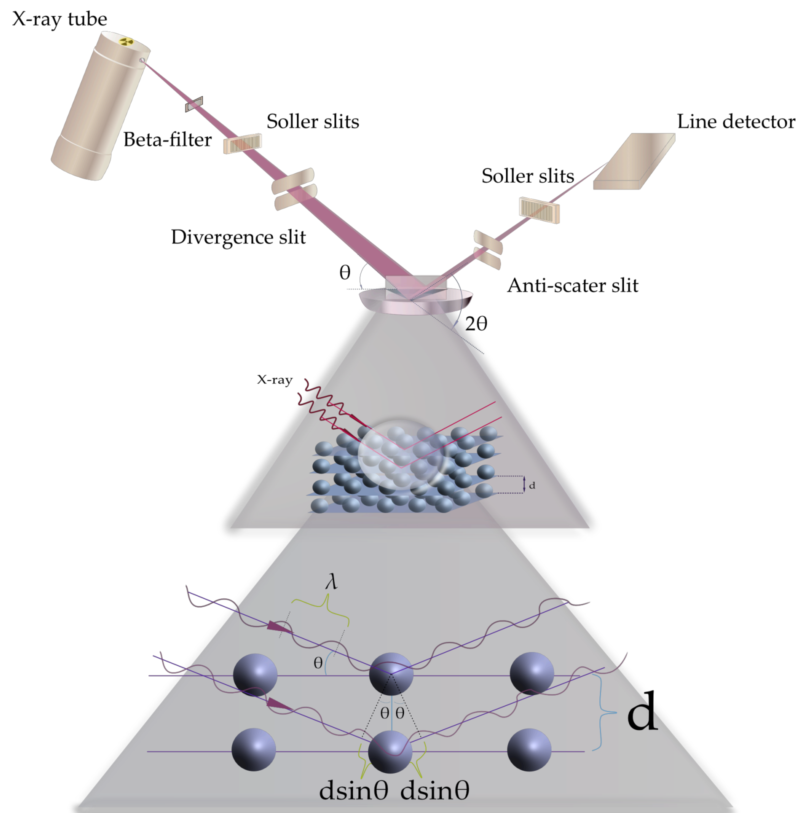

Figure 3.3 Schematic diagram of the diffractometer configuration of Bragg—Brentano geometry used in PANalytical diffractometer. Schematic illustration of Bragg law which is shown more closely.

3.3 X-ray reflectivity method

The other powerful non-destructive X-ray method used to characterize multilayers and the thin films is X-ray Reflectivity (XRR). This technique is used to determine structural qualities of the by sample analyzing its electron density, thickness, roughness and chemical composition. It is not based on diffraction phenomena due to the fact the X-rays impinge on a flat surface and in part are reflected and transmitted through the material. In the main concept, XRR used the optical properties of X-Ray, including Snell's law. Hence, the investigated sample may be amorphous and not consist of crystalline matter. The geometry of the experiment is close to Bragg-Brentano, where both incident and exit angle are equal; however, the X-ray beam is in the range between 0° to 5° depending on film properties and materials. First Kiessing (150) observed that density of material relates to critical angle θ_c. The index of refractive index for X-ray is expressed by

$$n = 1 - \delta - i\beta \quad (3.3)$$

where δ is dispersion and β is absorption terms,

$$\delta = \left(\frac{\lambda^2}{2\pi}\right) r_e N_a \rho \left(\frac{Z + f'}{A}\right) = \left(\frac{\lambda^2}{2\pi}\right) r_e \rho_e \quad (3.4)$$

$$\beta = \left(\frac{\lambda^2}{2\pi}\right) r_e N_a \rho \left(\frac{f''}{Z + f'}\right) \delta = \frac{\lambda}{4\pi} \mu \quad (3.5)$$

where λ is the wavelength, r_e the classical electron radius ($r_e = 2.818 \cdot 10^{-15} m$), ρ the mass density, ρ_e the electron density of material, N_a Avogadro's number, Z atomic number, A the atomic mass and μ is linear absorption coefficient for energies far from X – ray threshold. The corrected *f'* and *f''* are real (dispersion) and imaginary (absorption) part of the dispersion corrections, respectively (150, 151,152).

The investigated materials have different δ parameter dependent on their refractive index (deviated from unity) and its scattering properties. Hence dispersion (eq. 3.4) is proportional to the product of scattered electron with Thompson amplitude r_e far from absorption edge and electron density ρ_e. The typical values of both δ and β are in the range 10^{-5} to 10^{-8} such that the refractive index is slightly less than 1.

The total external reflection from a sample surface must be less than the critical angle θ_c when the X-ray beam hits the surface under the angle θ_{tr} obtained from Snell-Descartes' law

$$cos\theta_c = n = 1 - \delta \quad (3.6)$$

moreover, the approximating $\cos\theta_c$ to small angles

$$\theta_c = \sqrt{2\delta} \quad (3.7)$$

Typical values of θ_c are of the order of some milli-radian. For Nb and Ta is equal $\theta_c^{Nb}(\lambda \sim 1.54\text{Å}) = 0.4°$ and $\theta_c^{Ta}(\lambda \sim 1.54\text{Å}) = 0.51°$.

The thickness of multilayers or oxide layers from XRR is determined by analysis of so-called Kiessing fringes (Figure 3.5). However, information hidden in them are described by Fresnel reflectivity. The multilayers deposited on substrate contain N layers. Each of the layer *j* has a refractive index n_j described by Eq. 3.3 and thickness d_j, the interfaces are in Z_j. From each interface, the reflected r_j and transmitted t_j wave are described in relation

$$X_j = \frac{r_j}{t_j} = \frac{r_{j,j+1} + X_{j+1} e^{2ik_{Z,j} Z_j}}{1 + r_{j,j+1} X_{j+1} e^{2ik_{Z,j} Z_j}} e^{-2ik_{Z,j} Z_j} \ . \quad (3.8)$$

where

$$r_{j,j+1} = \frac{k_{Z,j} - k_{Z,j+1}}{k_{Z,j} + k_{Z,j+1}} \ . \quad (3.9)$$

is Fresnel coefficient of the interface between layer j and j+1. The $k_{Z,j}$ is the z-component of the wave vector of layer j (see Figure 3.4) (153,154).

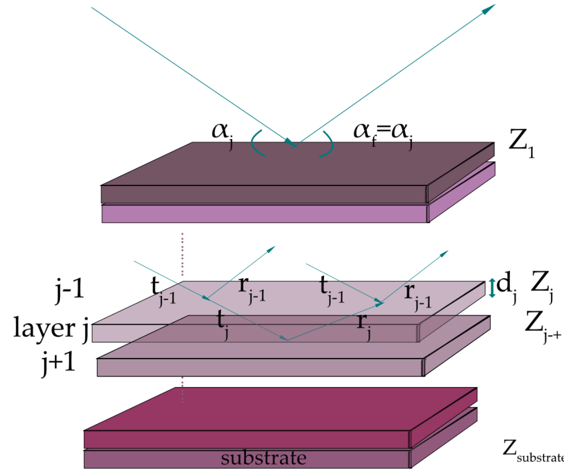

Figure 3.4 Illustration of the plane of incidence for a stratified medium (153,154)

The oscillations (Kiessing fringes) have their origin in the electron density of considered film. Electron density profiles are irrespective of the crystallinity and their periodicity in q and can be expressed by the relation

$$t = \frac{\lambda}{2\Delta\theta} = \frac{2\pi}{\Delta q} \quad (3.10)$$

where

$$q = \frac{4\pi sin\theta}{\lambda} \quad (3.11)$$

Δθ (or Δq) is the difference between two consecutive minima and λ is wavelength (for typically Cu Kα line ≈1.54Å). This method only gives the proper result when an angle is greater or equal 4θ.

All measurement presented in this thesis were obtained by analytical Empyrean diffractometers in Chorzow. The calculation of thickness and density profile of layers was

made with software REFLETIVITIE2000 written by G. Vignaud and A. Gibaud and X-pert Reflectivity.

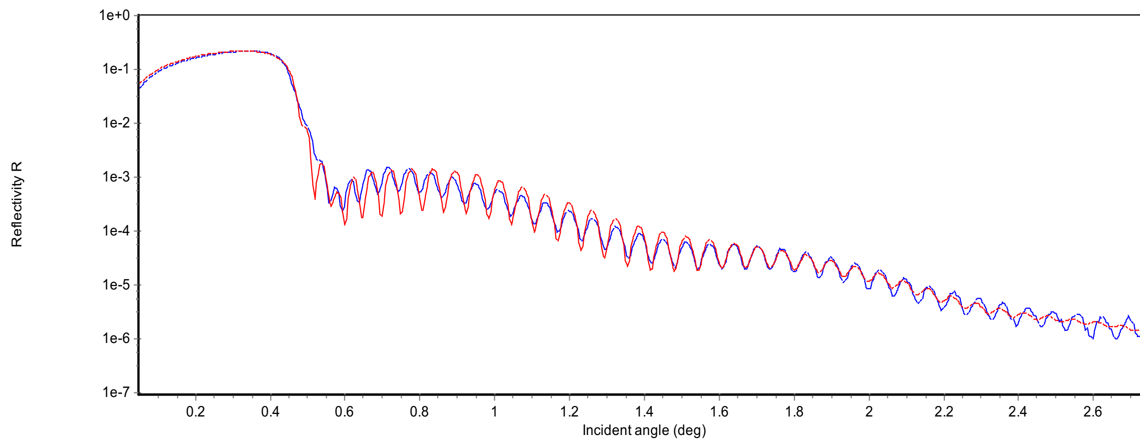

Figure 3.5 Example of Ta_2O_5 thin layer. The blue line is an experimental result and the red one is derived from the calculation.

3.4 Atomic Force Microscopy

Besides Scanning Tunneling Microscopy (STM), Atomic Force Microscopy (AFM) allows obtaining information about the surface of a solid with atomic resolution. Both microscopic techniques belong to the Scanning Probe Microscopy (SPM) family and were invented by Gerard Binning and his colleagues in the 1980's. They are based on the concept of using a very sharp probe (tip) to investigate topography, friction, stiffness, adhesion, charge, etc. of a given material in a controlled way. However, a characteristic feature of the AFM is that a deflected flexible cantilever with a sharp tip is used to determine the topography of the sample. With this system, different forces may influence the final result (11). When the tip is at a distance of 100nm from the surface, it interacts electrostatically (Coulomb force). If the tip is on the level 10 nm above the surface, the van der Waals interaction occurs between the tip and surface. However, below 0.2 nm and 0.1nm, the forces are closely connected with molecular and covalent bonding. They are described by Lennart-Jones phonetical (eq 3.12.)

$$V = 4\varepsilon\left[\left(\frac{\sigma}{r}\right)^{12} - \left(\frac{\sigma}{r}\right)^{6}\right] \tag{3.12}$$

Where ε is the depth of potential, σ is a distance where potential is zero [Figure 3.6]. The first part of Eq. 3.12 relates to van der Waals potential; the second represents the repulsive potential to the surface. The typical distance between tip and sample force-distance taking in account repulsive and attractive forces is shown at Figure 3.6.

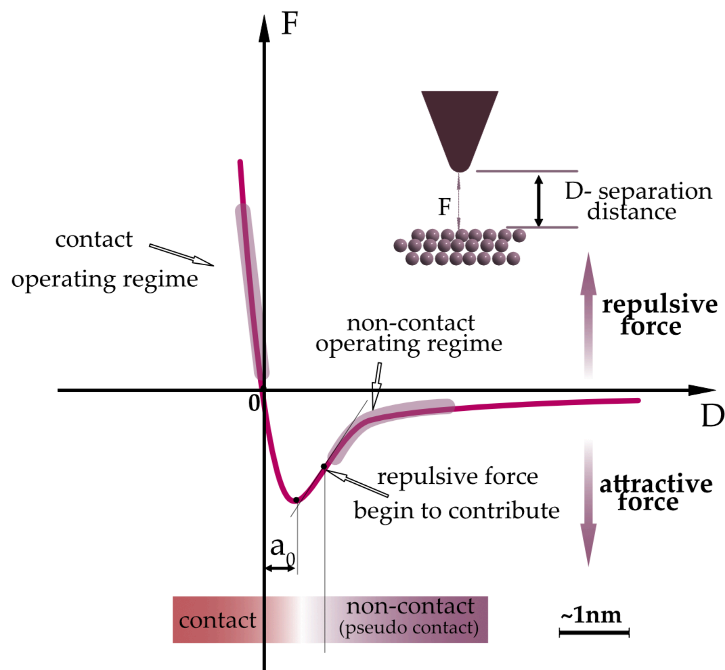

Figure 3.6 A simple sketch of interaction force F as a function of separation distance D between the tip and the specimen. The positive interaction force stands for a repulsive force pushing the tip away from the sample. This imposes a positive deflection of the cantilever in a vertical direction. A negative integration force stands for attractive force pulling the tip towards the sample, which leads to a negative deflection of the cantilever. The sketch can be diveded into three zones according to the presentence of attractive and repulsive forces. The attractive forces play crucial role in the non-contact (dynamic) operation mode.
The attractive force zone starts at infinite distance D from the sample where the interaction force approaches zero and is undetectable. The zero ends when the repulsive interaction starts to continue approaching the sample with the tip, the force gradient starts to decrease again. In the zone, where both kinds of force are present, contribute to the interaction. The most significant distance is reached when the gradients of attractive and repulsive force are equals. Here, the attractive interaction force reaches its maximum. The distance that tip has to travel from the point to reach the full contact is equal to the intermolecular distance a_0. It depends on material properties of the tip and the same sample, usually in order of few a Ångstroms. In the last zone active is only repulsive force. It plays a crucial role in the contact (static) operation mode. The 'zero' point can be considered as beginning full contact between tip and sample. The interaction force in this position is equal to zero and the cantilever is not deflected. If the tip continues to approach the sample, the interaction force increases very fast and the tip starts to deform the measurement specimen. Scheme adapted from (143)

However, forces between the tip and surface are described by van der Waals interaction. This occurs between the microscopic body and spherical end of the tip (radius R, density ρ_1) at distance D from the flat surface with density ρ_2 (155)

$$F = \frac{\pi^2 \rho_1 \rho_2 CR}{6} \frac{1}{D^2} \qquad (3.13)$$

The Figure 3.7 illustrates the measurement principle of topography. The displacement of the probe tip is defined by an optical lever, amplifying the vertical cantilever moment into a 2-quadrant photodiode. It is determined by focusing a laser beam onto the backside of the cantilever and directing it to the photodiode.

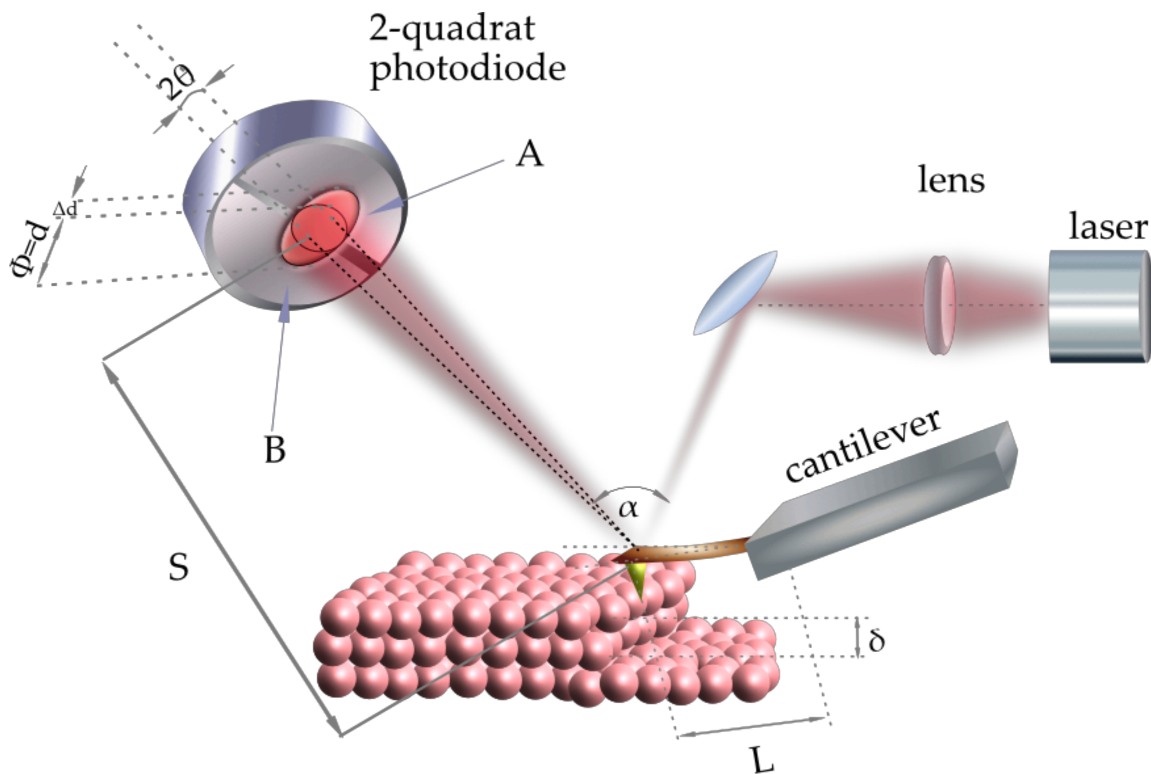

Figure 3.7 The scheme of AFM measurement adapted from Rodenbüchner thesis (12)

The relation between L (cantilever length) and S (distance to the photodiode) is called the lever amplification; with typically a factor of about one thousand. This ratio permits defining the tip displacement of the order of 0.01nm but is limited by the mechanical stability of the measurement setup. However, another method to measure the cantilever displacement exists similar to laser interferometry, which will not be described in this dissertation. The sample surface topography is scanned by moving the cantilever with piezo motors in the real space coordinate. The cantilever uses a z-coordinate, while x- and y-coordinates are related to the motors. Furthermore, damage of the surface is prevented by the cantilever tip or controlling the z-motor by the setup cantilever displacement as a

feedback loop (12).

There are three main topographical modes in this technique.

- First, contact mode (static) where the tip is in full contact with the sample surface (Figure 3.8). The static deflection of the cantilever measures the topography in atomic scale resolution. In this mode, when conductive tip (e.g. Pt/Ir) is in contact with the surface, the current flowing between tip and surface is measured when voltage is applied to the tip. This measurement technique is called local conductivity atomic force microscopy (LC-AFM). This mode is important for the investigation of resistivity switching phenomena in metal oxides (155).

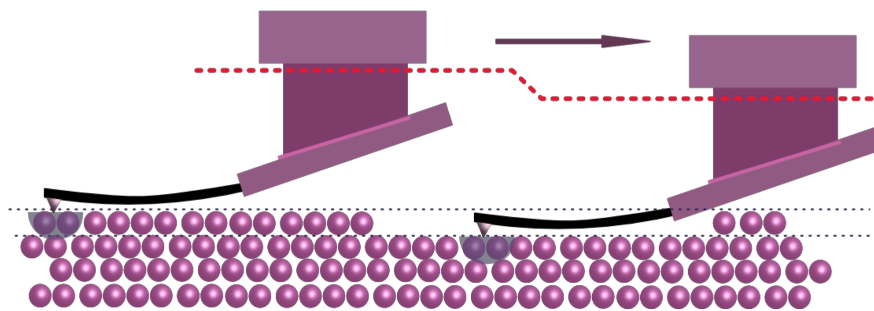

Figure 3.8 Contact (static) operation mode

- A non-contact (dynamic) mode where the cantilever is in resonant frequency (or close to it) of the piezoelectric drive with vibration amplitude less than 100nm. The modulated oscillation describes the surface topography (Figure 3.9) (155).

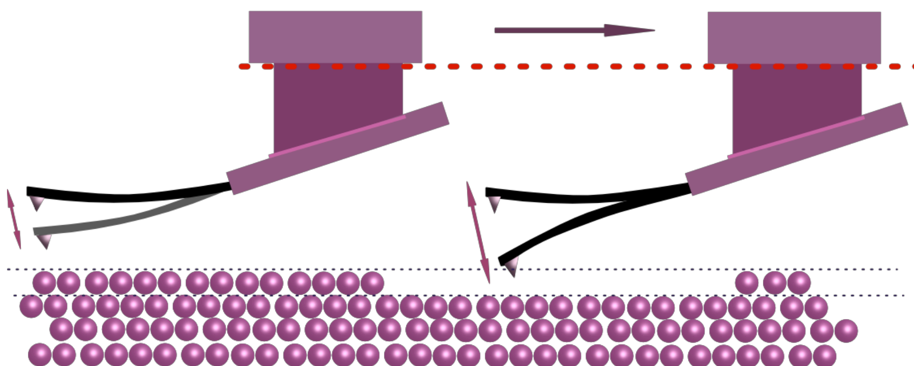

Figure 3.9 Non-contact (dynamic) operation mode

- Tapping mode is a combination of both above modes (Figure 3.10). It allows minimalizing the friction between the tip and measured surface, which is

dominant in static mode. In this mode when the oscillating tip only touches the sample surface at the maximum deflection of the cantilever, at the moment the direct mechanical contact is with the strongly repulsive interaction between tip and surface. The distance between the tip and the sample can be controlled (155).

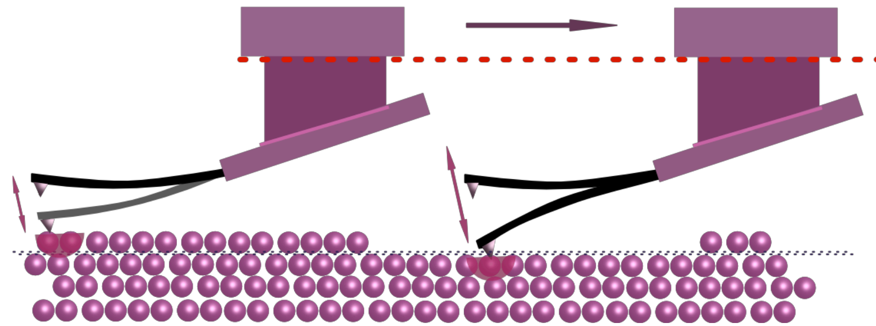

Figure 3.10 Tapping operation mode

In this work are presented AFM studies, obtained by Omicron STM/AFM VT-50/500 and Jeol JSPM-4610A equipped with Pt/Ir and diamond tips.

3.5 Raman spectroscopy

One of the most popular optical methods to characterize lattice dynamic in solids is Raman spectroscopy. The inelastic scattering of the light on atoms was first observed in 1928 by Chandrasekhara Venkata Raman and is now called the Raman effect. It is a powerful technique to probe molecular and crystal lattice vibration and is sensitive to composition, bonding, chemical environment, phase and crystalline structure of the investigated material. Raman spectroscopy allows identifying the structure of the material in any physical form, such as gases, liquids, solution, crystalline or amorphous solids. The effect is described through inelastic scattering of photons. The electron is excited by a laser beam to higher virtual energy level E^*. This energy is not stable, hence the electron decays to a lower energy state**,** which can be vibrational existed state E_{vib} representing lattice vibrations (Figure 3.12). However, on the other hand, an electron can also be exited from a vibrational state and decay into the ground state E_g. Both these states, where an emitted photon has lower and higher energies, are called Stokes and Anti-Stokes respectively. The energy shift between absorbed and emitted light is measured and can be assigned to the mode of lattice vibration (12).

The Raman spectra of a single crystal of Nb_2O_5 were recorded using a multichannel Raman spectrometer T64000 JobinYvon-Horiba equipped with an Olympus BX40 microscope system, 50x objective and argon-krypton laser (Coherent Innova-70) operating at 514.5 nm with approximately 3.5 mW of radiation power at the sample. Triple monochromator modes with resolution of a 0.7 cm^{-1} with 1800 lines/mm allowed the collection of Raman spectra in the two spectral windows i) 10 - 510 cm^{-1} and ii) 510 – 1110 cm^{-1} as a result of the gratings. Single Raman spectra were accumulated by 5 scans with an integration time of 120 s in each region. The polarized Raman spectra were obtained on H-Nb_2O_5 crystals previously oriented under a polarized optical microscope. Here, the incident excitation laser beam was stated as parallel to the z-axis of Nb_2O_5 crystals (c.a. 500 x 500μm) positioned with the (001) face parallel to the XY plane of the microscope stage. It is crucial to note that the orientation of the niobium crystal might be somewhat speculative due to difficulties in its spatial orientation among the main axis as a result of crystal twinning or its imperfections. Therefore, the possible choices of the assumed crystal face result from low crystal index (001) direction which was only locally assumed on the base of the shape of the crystal observed under the microscope (Figure 3.11). Hence, the polarization was measured at 0° (z(xx)z), 90° (z(xy)z), 180° (z(yy)z), and 270° (z(yx)z).

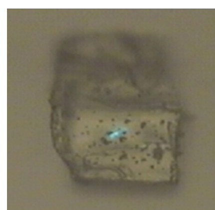

Figure 3.11 Crystal oriented among the (001) (main axis) investigated by Raman. The green dot shows where the laser beam was on the crystal.

The thermal stability and determination of phase transformation were obtained using measurements performed during heating to 900°C using a LINKAM THMS600 heating stage with a temperature accuracy of 1°C. All temperature-depended measurements were performed under polarized light with similar polarization angle as in the case of data collected at room temperature. All data were pre-prepared for analysis performing a baseline correction, cosmic ray removal and peak fitting analysis with a minimum number of components representing the physical view of the crystal structure were performed using GRAMS software package. The spectrometer's monochromator was calibrated using

the Raman scattering line of a silicon plate (520.7 cm^{-1}). All experiment were performed at Universite du Main, Le Mans, France.

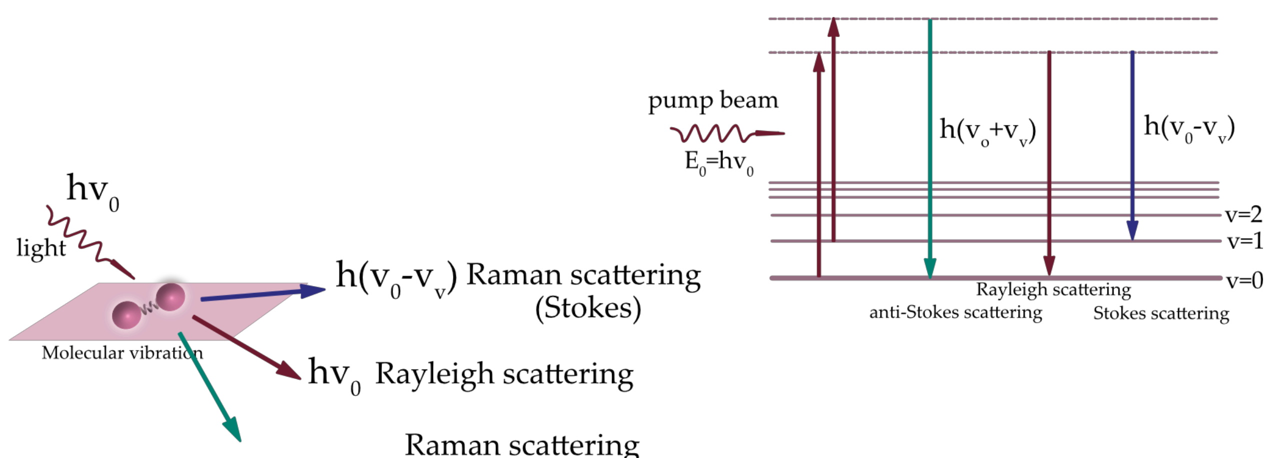

Figure 3.12 Schematic identifying light scattering after laser exposure on a sample surface. Photons of light are focused on the sample through the microscope objective at a defined magnification. When they interact with chemical bonds within the material electrons are excited to virtual energy levels. These molecules return to the original energy level by emitting a photon of light, known as elastic or Rayleigh scattering, or it can undergo an energy shift and return at lower (Stokes) or higher (anti-Stokes) energy levels, known as Raman scattering. Raman scattering is a low-probability process with around 1 in 108 photons inelastically scattered (arrow widths are not representative); Stokes Raman scattering is more intense than anti-Stokes scattering because of the increased probability of a molecule being in the ground vibrational state. Fluorescence can occur when electrons are excited to electronic energy levels and return to the ground energy level by emitting a photon of light at a longer wavelength. Adapted from (156)

3.6 Time of flight secondary ion mass spectroscopy

Another powerful and extensive surface sensitive technique in usage is Time of Flight Secondary Ion Mass Spectrometry (ToF SIMS). It is generally used for the identification of trace elements, organic molecules, biological structure and polymer on the surface. This technique works well in investigating the effects of grain boundaries or the impact of highly defective areas on the oxide surface. Since the first work of Professor Alfred Benningove's group (157) at the University of Münster in the 1980's, TOF-SIMS have undergone continual development (158). The detection limit of TOF SIMS is 1 ppm for some molecules and down to 1 ppb for some elements. Depending on the SIMS mode, the information is coming from the top nanometers of the sample (static mode) or its depth (depth profile) with the best resolution of approximately 1 monolayer. This versatile technique not only generates mass spectra which show elements, molecules or molecular fragment of the surface, and distribution maps of particular secondary ions, but also can determine 3-dimensional elemental or molecular distribution by depth profiling of the

samples. The TOF-SIMS, unlike XPS, can detect all elements in the periodic table. However, TOF-SIMS has a destructive nature towards sample. The sample is bombarded with pulsed Bi primary ions in ultra-high vacuum samples surface, then a small fraction (typically 10^{-2} to 10^{-4}) of the desorbed species are ionized, called secondary ions (Figure 3.13). They are extracted via application of an extraction voltage and analyses in time- of-flight mass spectrometer. The typical TOF-SIMS instrument schematic diagram is shown in Figure 3.13. In this work a TOF.SIMS-5 spectrometer designed by IonTOF was used with a bismuth analysis ion source and caesium ion sputtering source. (159)

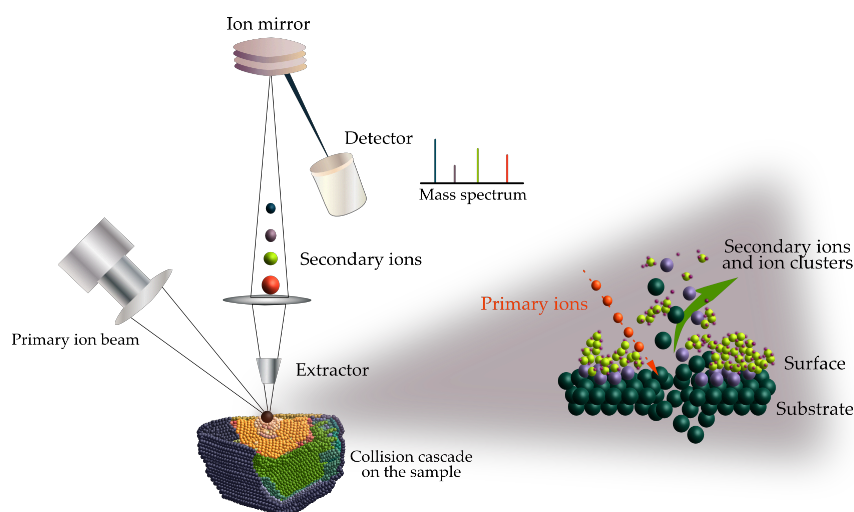

Figure 3.13 Schematic diagram of TOF-SIMS instrument. The surface bombarded by Bi ions generate the different types of secondary ions and cluster ions.

4. Results and discussion

In this chapter the results of investigation of niobium pentoxide single crystal and thin films of tantalum and niobium oxides are shown. In the beginning, the chapter considers the structural, morphological and atomic properties of Nb_2O_5 single crystal, then analysis of the fundamental properties of the thin films is presented.
Part of this chapter have been published before in:

Nowak A, Persson J, Schmelzer B, Szade J, Szot K. Low temperature reduction in Ta–O and Nb–O thin films. J Phys D: Appl Phys. 2014 Mar 10;47(13):135301–10.

4.1 Basic properties of Nb_2O_5 single crystals

In this thesis, the first studies of Nb_2O_5 single crystal will be shown. Its fundamental properties such as its crystal and electronic structure are well known, however, this is the first time the properties have been demonstrated in connection with controlled temperature by driven reduction. The results of morphology and local-conductivity studies of the crystals are also discussed in the following sub-chapter of this thesis.

4.1.1 Crystallographic structure

The first investigations of Nb_2O_5 single crystal by zone floating technique was in 1976 by Shindo and Kamatsu (38). The obtained crystal by this technique showed a twinning plane in the growing crystal. One year earlier, Katsuo Kato (37) showed the high-temperature modification of niobium pentoxide. He called this crystal structure as H-Nb_2O_5. However, their crystal was obtained by the Bridgman-Stockbarger technique. The single crystal had a monoclinic P2/m structure with cell parameters: a=21.153 (7)Å, b= 3.8233 (5) Å, c= 19.356 (5) Å, β =119.80 (2)° (37). An ordered block structure with (5x3) and (4x3) group of corner-sharing NbO_6 octahedra with each block (Figure 4.1) was observed. In this thesis, the niobium pentoxide single crystal was grown by zone floating technique. Nevertheless, the earlier studies of Shindo and Kamatsu (38) showed that

crystal grown by this technique had a twinned lattice structure. The four-cycle single crystal X-ray diffraction (XRD) investigation on a 0.1x0.1μm piece of crystal, has confirmed this result. The refined parameters of twinned crystal used in shelXle software are combined with the literature reference (Table 4). The single crystal XRD structure refinements show that for both fitted structures the space group is the same P2/m as reported in the literature (37). However, both matches of twins showed different cell parameters (Table 4). The obtained result showed that only one structure (called as Nb_2O_5(2) in Table 4) almost corresponds to the literature data in terms of lattice parameters. The lattice parameters of Nb_2O_5 (1) phase significantly differ from Nb_2O_5 (2) when comparing c parameters, the c parameter of (1) phase is c.a. 1.5 time longer than in phase (2).

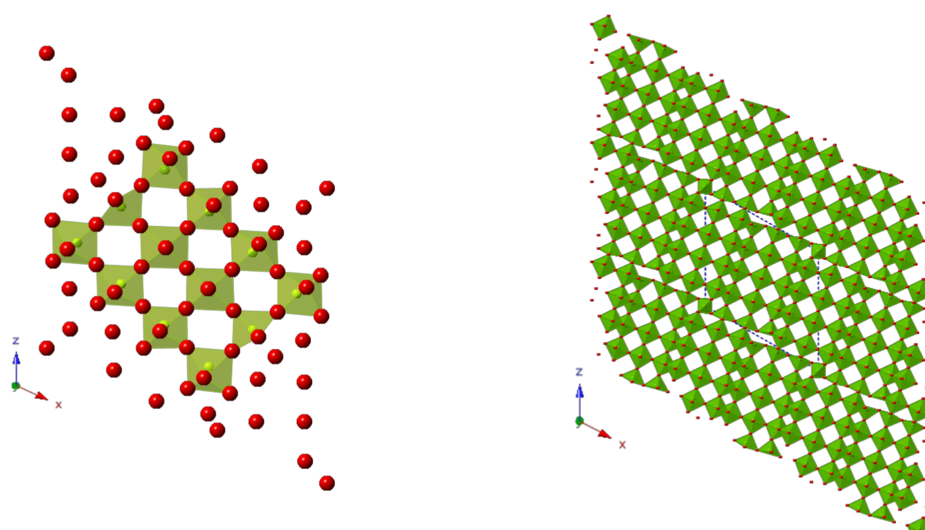

Figure 4.1 Structure two obtained from fitting the diffraction studies compared to the H-Nb_2O_5 from literature (37).

The difference in the c parameter may be related to the block-like structure of niobium pentoxide and the varying distribution of tetrahedrally coordinated Nb atoms. Moreover, beforehand Laue diffraction patterns cleave the Nb_2O_5 crystal (Figure 4.2) indicating that the crystal has a very complicated structure as Shindo and Kamatsu mentioned in their work (38). The Laue diffraction patterns of twinned crystal overlap one another. The beam size in Laue diffractometry is much larger than in the 4 circles which most likely indicates the beam was diffracted by several twinned blocks. The polycrystal circles may also come from surface contamination and/or a defected surface.

NB_2O_5 (1)	NB_2O_5 (2)	literature data (37)
a = 20.3622(3) Å	a = 19.35237(3) Å	a = 21.153 (7) Å
b = 3.8263(1) Å	b = 3.82222 (4) Å	b = 3.8233 (5) Å
c = 35.0271(6) Å	c = 20.36953 (2) Å	c = 19.356 (5) Å
α = 90.0000(0)°	α = 90.0000(0)°	α = 90.0000(0) °
β = 95.8260(10)°	β = 115.6975 (5)°	β = 119.80°
γ = 90.0000(0) °	γ = 90.0000(0)°	γ = 90.0000(0)°

Table 4 Result for structure refinement on the twinning structure of Nb_2O_5 single crystal

After basic crystallographic tests, the Nb_2O_5 single crystal was crushed into powder for investigations in the broad temperature range. The powder diffraction was performed with the use of Empyrean PANalytical powder diffractometer in an air and diluted hydrogen atmosphere at a temperature range up to 1000°C. From the literature (Chapter 2, Sec. 2.3.3) it is known that H crystal phase is formed at 1100°C. A few years ago, Qi et al. (160) obtained H-Nb_2O_5 crystal in the form of nanofibers beginning at 500°C. There is a lack of information on the behavior of H-Nb_2O_5 single crystal after heating in air. Recently, Pilarek et al. (161) showed that after annealing commercially available Nb_2O_5 in an air environment of 800-1100 °C, a mixture of three main phases of niobium pentoxide H, M and T are formed. Moreover, at stable H-Nb_2O_5 structure, without the presence of other Nb-O phases, was achieved after melting powdered crystal at 1500°C.

Figure 4.2 The Laue diffraction pattern of single crystal Nb_2O_5 collected on crystal as-grown.

In this investigated case, the different temperature conditions and their influence on the cell parameters of H-Nb_2O_5 crystal were considered. The evolution of the temperature dependence of the powder diffraction pattern was provided by the Rietveld refinement method (162). The procedure started after adapting the structural or dataset points from

the database. The starting point for calculated reflection positions and intensities are refined to the experimental data in an iterative mathematic process based on the least squares' method. With this method, the refined results generally include the unit cell parameters (a, b, c, α, β, γ) and atomic position (x,y,z) with temperature displacement factor (Debye-Waller factors), the profile parameters of the used mathematical function, asymmetry of the reflections, multiple background points, and parameters depending on the measuring device and method (e.g. displacement and transparency) (163). All factors can be refined for multiple phases simultaneously.

The basic data phase analysis was made by HIGHSCORE+ from PANalytical software. The Rietveld refinements were carried out with FULLPROF.

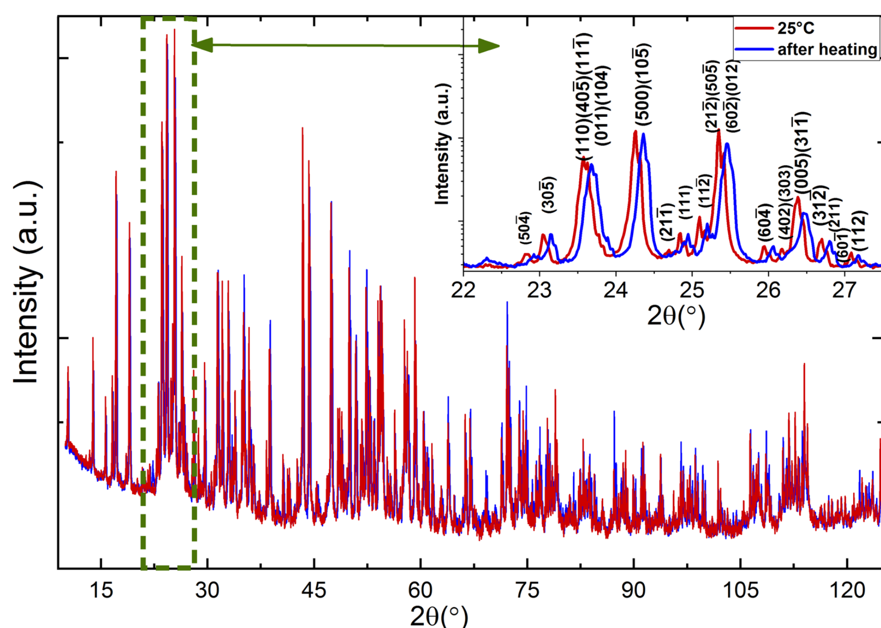

Figure 4.3 Powder diffraction pattern of the pulverized crystal in the before and after annealing. The data were collected in

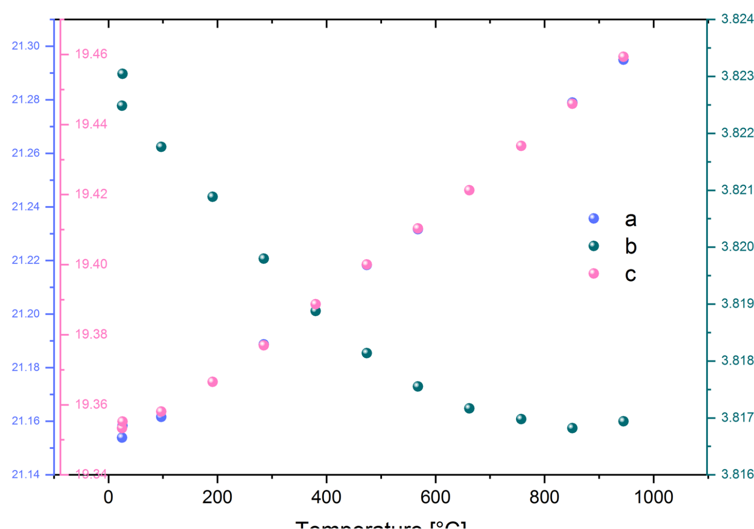

Figure 4.4 Temperature dependence of the cell parameters of H-Nb_2O_5 powder placed in air

Temperature [°C]	unit cell					
	a [Å]	b[Å]	c[Å]	α [°]	β [°]	γ [°]
25	21,15390(8)	3,82248(5)	19,35335(9)	90	119,816(3)	90
97	21,16158(3)	3,82176(3)	19,35804(9)	90	119,828(2)	90
191	21,17467(7)	3,82088(4)	19,36650(7)	90	119,844(0)	90
285	21,18871(7)	3,81979(6)	19,37699(1)	90	119,853(1)	90
380	21,20374(9)	3,81887(8)	19,38874(1)	90	119,863(2)	90
474	21,21833(6)	3,81814(0)	19,40003(6)	90	119,872(3)	90
568	21,23174(5)	3,81755(0)	19,41034(9)	90	119,877(1)	90
662	21,24627(1)	3,81716(7)	19,42124(4)	90	119,881(2)	90
757	21,26283(5)	3,81697(9)	19,43390(7)	90	119,888(1)	90
851	21,27899(9)	3,81682(2)	19,44595(5)	90	119,893(0)	90
945	21,29502(1)	3,81693(9)	19,45932(6)	90	119,90(0)	90
26	21.15837(5)	3.82304(7)	19.35518(8)	90	119.818(1)	90

Table 5 Cell parameters obtained from Rietveld refinement to H-Nb_2O_5 powder after heat process in air

The H-Nb_2O_5 powder pattern after heating at almost 1000°C in air showed slight distortion after cooling (Figure 4.3). The only significant change is observed in the b parameters (Figure 4.4). It decreases exponentially with temperature. A different trend is observed with a β angle which increases with the temperature. This effect showed that the unit cell is broadening with temperature (Table 5). A similar change overlap in the powder pattern was measured in a diluted hydrogen atmosphere (Figure 4.5). However, cell parameter b exhibited a polynomial trend. Moreover, parameters a and c exhibit linear increase with temperature (Figure 4.6).

Temperature [°C]	unit cell					
	a [Å]	b [Å]	c [Å]	α [°]	β [°]	γ [°]
25	21,1646(3)	3,82419(6)	19,3643(8)	90	119,818(1)	90
100	21,1735(9)	3,82422(9)	19,3686(6)	90	119,834(8)	90
200	21,1865(7)	3,82334(2)	19,3789(1)	90	119,853(3)	90
300	21,1956(0)	3,82280(4)	19,3873(2)	90	119,861(6)	90
400	21,2106(0)	3,82261(9)	19,3988(3)	90	119,864(1)	90
500	21,2248(1)	3,82198(6)	19,4136(7)	90	119,873(4)	90
600	21,2393(0)	3,82151(0)	19,4254(5)	90	119,875(0)	90
700	21,2496(8)	3,82236(5)	19,4406(0)	90	119,867(1)	90
800	21,2602(1)	3,82428(1)	19,4532(6)	90	119,848(2)	90
25	21,1485(9)	3,82788(9)	19,3720(1)	90	119,819(1)	90

Table 6 Cell parameters obtained from Rietveld refinement to H-Nb_2O_5 powder after heat process in diluted hydrogen.

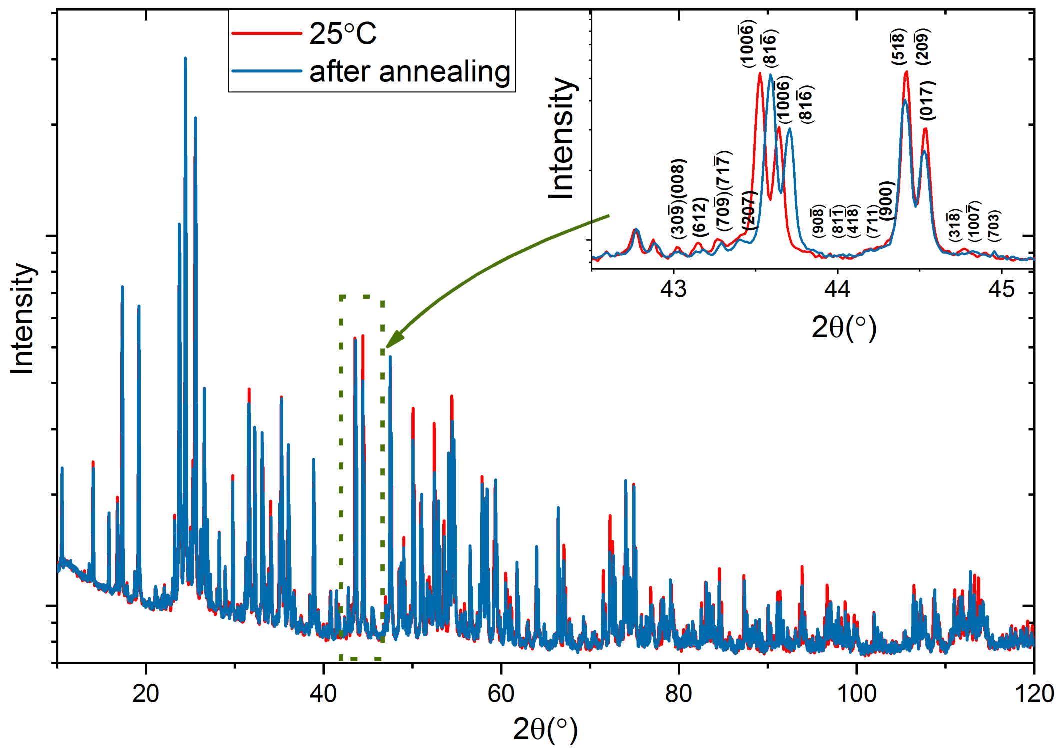

Figure 4.5 Powder diffraction pattern of the pulverized crystal in diluted hydrogen before and after annealing. In both cases, the data were collected at room temperature.

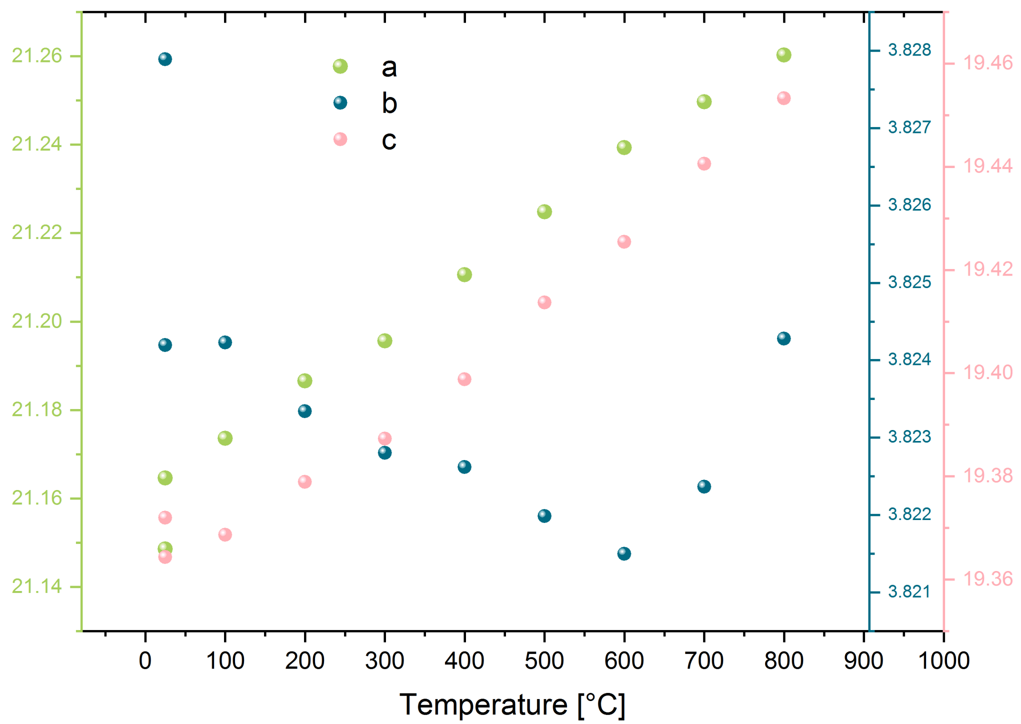

Figure 4.6 Temperature dependence of the cell parameters of H-Nb_2O_5 powder placed in a diluted hydrogen environment

The structural changes after cooling the process are inconsiderable, in contrast to measurements preformed in air where bordering of the peaks was observed. The cell parameters only indicated changes in the range 0.001% to 0.1%. In both atmospheres the lack of other crystal phases after reduction condition is difficult to find due to the large number of peaks. Hence, additional structural investigation was conducted and are described below.

However, in is worth mentioning that after 12h reduction in the H_2 atmosphere at 1050°C the energy dispersive X-ray spectroscopy (EDX) indicated that NbO_2 was presented on surface was (Figure 4.7). Nevertheless, in this thesis, this particular experiment is not considered in detail. The mentioned result was recently presented at the poster session by Wrana et.al. at Faraday Discussion 2018, Aachen, Germany.

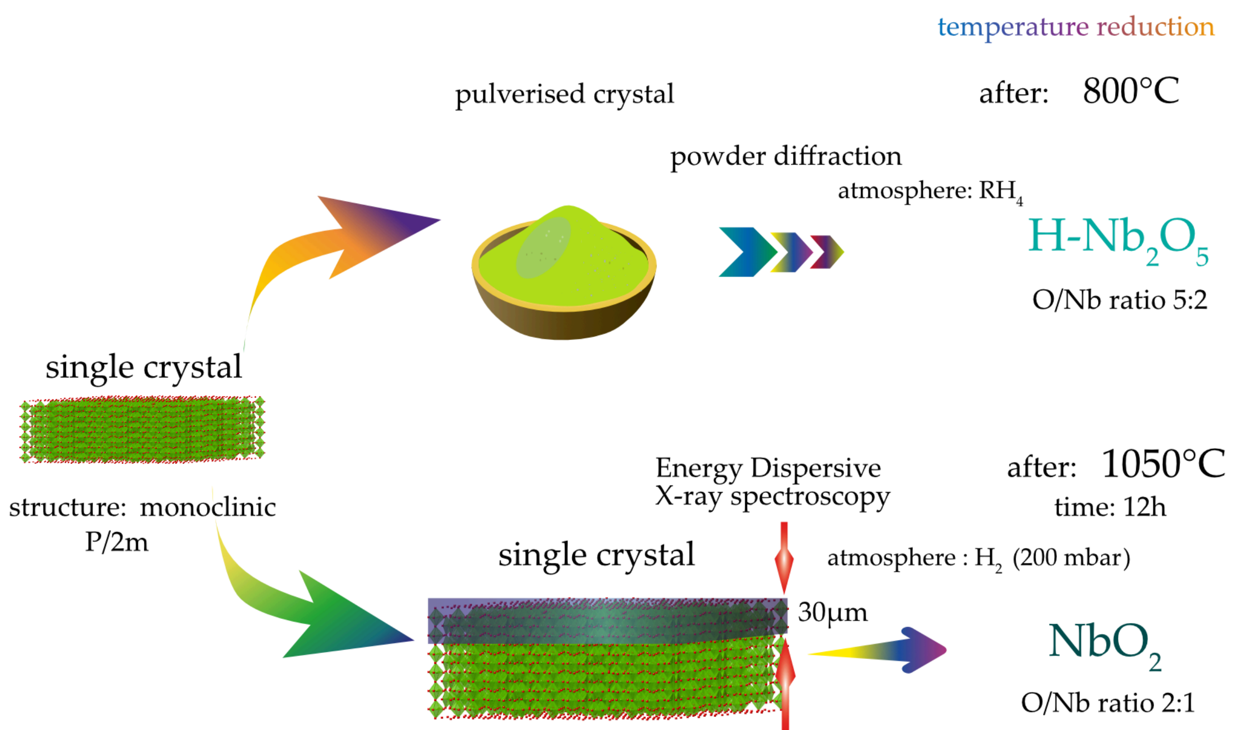

Figure 4.7 Difference between crystal non- and pulverized after reducing in H_2 and RH_4 atmosphere, respectively.

4.1.2 Raman spectroscopy

Raman spectroscopy was applied as a complementary technique for the investigation of crystal structure details and possible inhomogeneities of the H-Nb_2O_5 single crystal. As is known from theory the amount of active optical modes predicted by the symmetry analysis of monoclinic niobium (V) pentoxide with space group P2/m (C^1_{2h}) are given as $\Gamma_{red} = 95A_g(R) + 50A_u(IR) + 49B_g(R) + 100B_u(IR)$ (*R* = Raman active; IR = infrared active). Here, a total of 150 modes should be infrared-active while 95 modes should be Raman-active in the case of z(xy)z-direction of an incident polarized light and 49 modes at y(zx)y and x(yz)x polarization (Chapter 3 sec. 3.5). In turn, the number of acoustic vibrations is estimated as follows: $\Gamma_{red} = A_g(R) + 2B_u(IR)$ (164). However, the total number of bands observed in the experimental spectra strongly depends on the internal distortion of the crystal structure as well as modifications of the crystal field and might differ slightly from the theoretical projection.

The structure of niobium pentoxide belongs to the no centrosymmetric block structures (165) with a different type of niobium-oxygen polyhedra: edge-shared $(NbO_6)_{es}$ and corner-shared $(NbO_6)_{cs}$ octahedra as well as NbO_4 tetrahedra (Figure 4.8).

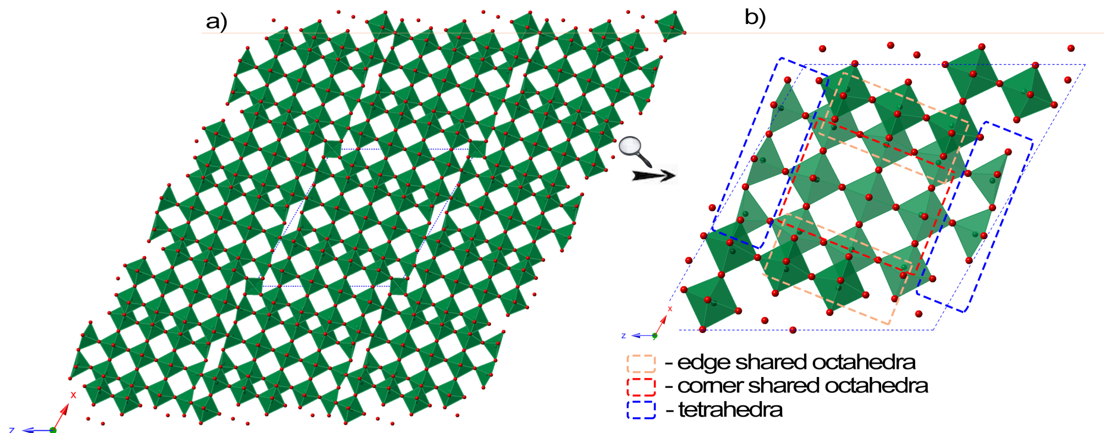

Figure 4.8 Crystal structure of a) H-Nb_2O_5 with various niobium-oxygen b) polyhedra: edge-shared $(NbO_6)_{es}$ and corner-shared $(NbO_6)_{cs}$ octahedra as well as NbO_4 tetrahedra. Oxygen is marked as small red dots.

Such atom arrangement generates local anisotropy which implies splitting of longitudinal-transverse optical (LO-TO) modes appearing in the Raman spectrum.

According to theoretical predictions the vibrations of NbO_6 complexes, due to the C_{2h} symmetry might be defined as $\Gamma_{red} = 2A_g(R) + A_u(IR) + B_g(R) + 2B_u(IR)$ or $\Gamma_{red} = A_g(R) + A_u(IR) + 2B_g(R) + 2B_u(IR)$ depending on the crystallographic position of niobium in the crystal structure. Specific crystal orientation in the XY plane with an incident laser beam parallel to the z-axis of the crystal, due to the theory, result in an activation of only the A_g type symmetrical modes wherein B_g are silent. In turn, the crystal field may provide activation of lower symmetrical modes (165).

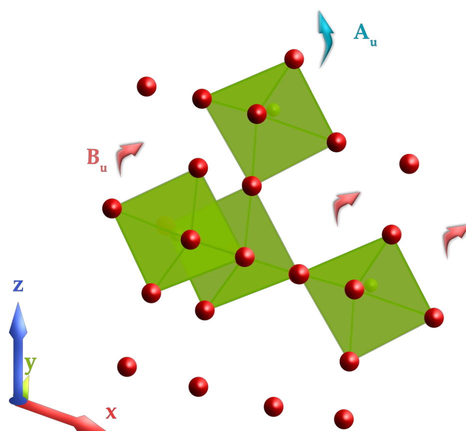

Figure 4.9 Acoustic mode presented in the 6Å part of H-Nb2O5 crystal oriented towards lattice parameter b

Correlation between theoretical prediction and experimental results provided by the mathematical equations was developed by Hardcastle and Wachs (166). As a result, the symmetric ν_1 stretching vibration of the Nb-O bond due to A_1 and E type LO modes in the 760 - 1000 cm^{-1} range correspond to the symmetric bending ν_2 (A_1 and E type) and ν_3 TO modes observed in the 620 - 680 cm^{-1} region. It is worth noting that internal distortion, caused by i) depolymerization of the ideal three-dimensional niobia network or ii) by tilting of two adjacent NbO_6 octahedra and the off-centere displacement of the Nb atom (167) imply that bands are strongly polarization sensitive. Moreover, the bands' intensity depends on the position of the crystal under the laser beam or position of the polarizer among the main axis of the crystal.

In the following, the experimental spectra of the analyzed Nb_2O_5 crystal are presented by sample geometry arranged according to procedure presented in the methodology part. Hence, the strong band observed at z(xx)z polarization of about 993 cm^{-1}, which according to many reports might originate from highly distorted NbO_6 octahedra with an asymmetric Nb-O=Nb bridge (165,167,168) .This band is an indication of unsaturated chemical bonds. A similar interpretation might be made for the band of

about 892 cm^{-1} originating from non-bridging Nb–O bond (168,169). Vibration of these bands may also be overlapping within edge-shared and corner-shared octahedra (170). The intensity of such bands lowers permanently with the rotation of the crystal, indicating high sensitivity of such units to polarization. According to some authors this may result from the unsaturated chemical bonds in the marginal part of the crystal structure. The strong intensity of such bands is probably an effect of specific arrangement in the structure, what is especially visible at z(yy)z polarization at which those intensities are very low. Similar modification in band intensity is observable in the case of LO-TO modes for NbO_6 octahedra. It is worth noting this unit due to two band generating structural anisotropy as observed at 598 cm^{-1} which is associated with bridging oxygen in corner-shared $(NbO_6)_{cs}$ units and at around 659 cm^{-1} with the edge-shared $(NbO_6)_{es}$ moieties. The presence of such bands, their position as well as polarizability is strongly conditioned through the degree of distortion of niobia octahedra. That results from the size of the niobium ion which is relatively too small to form a regular octahedra (170). Such deformation might also be explained by Pauling's electrostatic valence rule (171). As a result, one can distinguish slightly distorted corner-shared octahedra with the Nb-O bonds in the range of 1.9 - 2.0 Å and highly distorted edge-shared octahedra characterized by the shorter (1.7 - 1.9 Å) and longer (2.0 - 2.3 Å) Nb-O bonds. Furthermore, the stronger electrostatic repulsion occurring within the edge-sharing octahedra in relation to corner-sharing moieties might provide stronger deformation of the $(NbO_6)_{es}$ units which activate Nb-O-Nb vibrational modes and correspond to the band at about 689 cm^{-1} (165) . Its origin might also be correlated with some type of bond order within the niobia polyhedra due to the more ordered structure characteristic for the TT-phase (167). This observation may confirm a twinning structure of the analyzed Nb_2O_5 (172) within an additional crystal sub-lattice, in which locally appeared a pseudohexagonal phase which enforces the appearance of internal strains or structural disorder. The twinning structure may also explain the presence of many such bands which were not predicted by theoretical calculation. It is also interesting is also that the intensity of such band is more or less similar at the rotation of the crystal in the XY plane suggesting similar orientation of the NbO_6 units along the main crystal axis (Figure 4.10). What is more importance is the presence of niobia distortion implies higher intensity of bands in the region of 620 - 680 cm^{-1} in relation to other ones that provide evidence about the quality of the three-dimensional network (173,174). Moreover, edge-shared octahedra predominate over

those which are corner-shared, implying stronger bands in the spectrum (Figure 4.10). Additional evidence of structural distortion within niobia octahedra is provided by the high polarizability of the main bands of this region (Figure 4.10). Here, one can observe a mutual correlation between the intensity and position of bands derived from the $(NbO_6)_{cs}$ and $(NbO_6)_{es}$ i.e. stronger bands of $(NbO_6)_{cs}$ are connected to the lower intensity bands of $(NbO_6)_{es}$ with a slightly blue-shift of the band position. This is especially easily observed for z(yx)z for which corner-shared niobia octahedra are probably arranged more parallel to the main crystal axis and incident laser beam. One possible explanation might possible be slightly inaccurate orientation of the crystal relative to the beam. The opposite situation is observed in z(yy)z and z(xy)z polarization for which bands of $(NbO_6)_{es}$ are stronger in intensity, indicating their arrangement in the direction of the main crystal axis of the Nb_2O_5 crystal. The band shift, in turn, might result from:

i) locally different arrangement of the $(NbO_6)_{cs}$-$(NbO_6)_{es}$ units in the crystal structure,

ii) deformation of $(NbO_6)_{es}$ units or

iii) presence of point defects in the form of e.g. oxygen vacancies such as in the TT-phase as suggested before.

Interestingly the system composed of $(NbO_6)_{cs}$-$(NbO_6)_{es}$ is additionally tilted, probably due to structural distortion / deformation of the crystal structure evidence through the relatively low intensity of bands in the region of 620 - 680 cm^{-1} at z(xx)z polarization (Figure 4.10). Moreover, the magnitude of the band at 689 cm^{-1} is not fully correlated with alteration of the previously mentioned bands and is practically not polarized-affected. This may confirm a more ordered structure presence locally which hypothetically may correspond to the TT-Nb_2O_5.

At a lower wavenumber, the main bands of the range 300 - 550 cm^{-1} are associated with ν_5 bending modes of the Nb-O-Nb angle (A_1 and E type) in the block structure of niobium oxide while the anti-symmetric ν_4 bending vibration overlapping with the ν_6 bending of the O-Nb-O angle are located in the 200 - 300 cm^{-1} range (165,167,175). Also, strong bands around 260 cm^{-1} arise from vibrations activated through the non-cubic structures, similar to literature data (165). Plenty of bands observed in this region and their high polarizability results from the structural anisotropy associated with $(NbO_6)_{cs}$-$(NbO_6)_{es}$-NbO_4. Unfortunately, such effect might also be correlated to the non-ideally

parallel crystal orientation among the incident laser beam. This spectral region is also responsible for the collective movement of the whole molecular fragments as well as of lattice modes. In turn, bands observed below 200 cm^{-1} result from the external modes wherein polarization sensitive bands close to 118, 140 and / or 180 cm^{-1} could be assigned to a metal-metal (Nb-Nb) vibration mode (170). The strong modification of the band intensity during the crystal rotation in the XY plane suggest very irregular spatial arrangement of the distorted niobia tetrahedra and the same possible interpretation of Nb-Nb bands could be made as for the A_1 or E type.

High resolution Raman spectroscopy data also allow to separate optical modes observed in the region of 100 - 1100 cm^{-1} from the acoustic modes which occurred in the 20 - 100 cm^{-1} range. Here, the bands are usually linked to the displacement of atoms of the same amplitude; direction and phase. The origin of such bands is somewhat controversial and it is usually difficult to provide an unambiguous interpretation. However, through the analogy to optical modes, bands in the 70 - 100 cm^{-1} region may be assigned to transverse acoustic (TA) modes within niobia octahedra wherein longitudinal acoustic (LA) modes associated with the Nb-O bonds may be observed in the 30 - 60 cm^{-1} range (Figure 4.10).

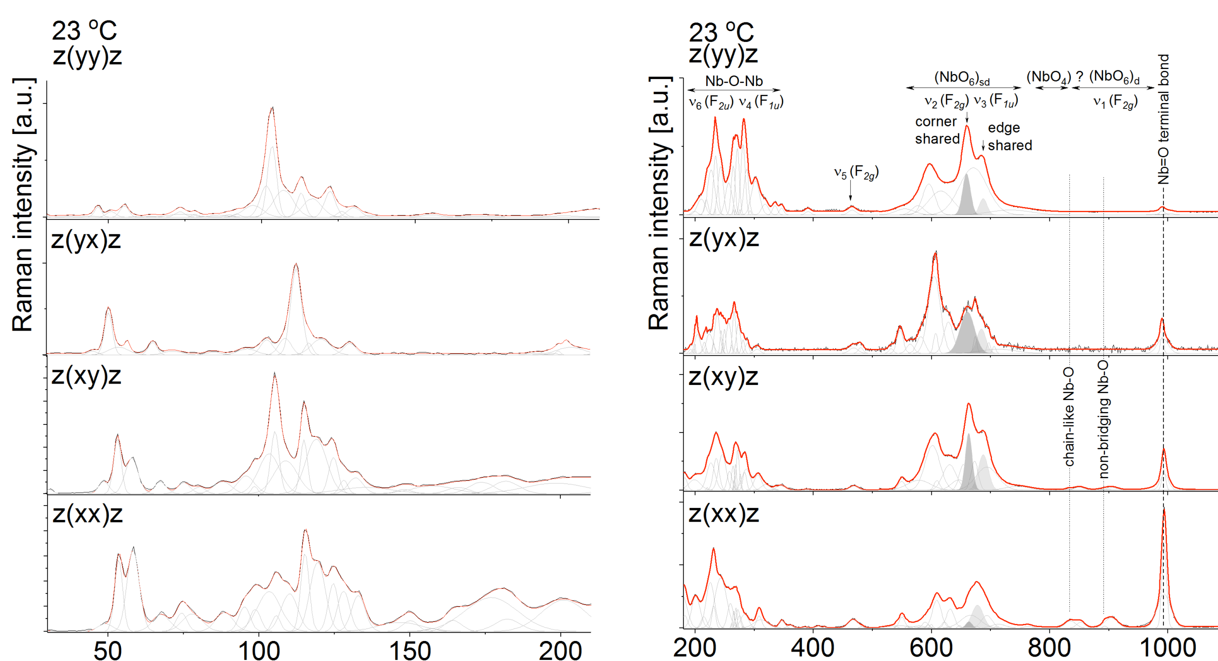

Figure 4.10 Polarized Raman spectra of the H-Nb_2O_5 single crystal oriented along the z-axis and rotated in the XY plane. The band fitting analysis were performed using Grams Software package. The different polyhedra were color-highlighted: dark gray means corner-shared, gray - slightly deformed edge-shared and light gray - highly distorted niobia octahedra. Acoustic modes were described by the red-arrow in the range below 100 cm^{-1} while the optical modes were illustrated in the 100 - 1100 cm^{-1} range.

The TA-LA modes, similar to TO-LO are also polarized-sensitive, giving an opportunity to determine the symmetry-dependent type of vibration. As a result, the band at about 50 cm^{-1} may originate from A_1 (Figure 4.10) or E type due to high intensity in z(xx)z, z(xy)z and z(yx)z polarization while the band at 58 cm^{-1} due to high intensity in z(xx)z probably originated from A_1. The intensity of bands in the TA region is relatively non-polarized-sensitive. The intensity of bands derived from the vibrations of TA modes in z(yy)z polarization is usually similar in intensity to bands of the LA modes. This may confirm a specific atom arrangement, structural deformation and probable titling of niobia octahedra along the main z-axis as appeared in the studied crystal.

According to Gatehouse et al. (176) in the crystal structure of H-Nb_2O_5 one of 28 of the niobium atoms appears in a tetrahedral coordination with Nb-O bond distance close to ~1.66 Å, and C_{2h} symmetry defined as $\Gamma_{red} = A_u(IR) + 2B_u(IR)$. The major bands derived from the Nb-O bond in tetrahedron might be located, respectively in the 790 - 830 cm^{-1} region (ν_1 vibrations), 300 - 350 cm^{-1} (ν_2 vibrations), 640 - 670 cm^{-1} (ν_3 vibrations) and 400 - 440 cm^{-1} (ν_4 vibrations) regions. However, the band intensity of the NbO_4 units is much less intense than of the octahedra, especially in the case of z(xy)z polarization. As a result, one can expect activation of the low intense ν_1 mode while the other ones such as ν_2, ν_3, and ν_4 are probably too weak to be seen on the spectrum or are overlapping with stronger bands of niobia octahedra (165,174). As a result, those modes were not analyzed further in the text.

4.1.2.1 Temperature-depended experiment

In situ heat treatment analysis were performed to look more precisely upon the crystal structure of niobium oxide, determine possible alteration taking place within the block structure of H-Nb_2O_5 and their impact on the phase transition. It is crucial to note that the crystal was annealed at air condition, and therefore those results cannot be directly correlated with other results obtained from vacuum data. The observed alterations are only suggestive of some hypothesis about possible structural modification taking place during the heating and cooling processes. This observation is usually performed by following the change in band position, modification of its intensity or full width at half maximum (FWHM). However, the crucial point is to perform so-called reduction procedures on the raw data which allow reducing problems originated from the thermal effects or real modifications taking place in the structure during the heating. Here, the real

intensity of Raman bands (I^{red}) and mean of phonons at a particular temperature n(ν,T) expressed by the Bose-like statistical description of phonons, are calculated using:

$$I^{red}(v) = \frac{v}{(v_L - v)^4}[n(v,T) + 1]I^{exp}(v);\ n(v,T) = \frac{1}{exp^{\frac{\hbar v}{k_B T}} - 1}$$

where $(v_L - v)^4$ is the correction for the wavelength dependence of the scattered intensity; $\hbar$ – Planck constant, k_B – Boltzmann constant, T – temperature.

As a result of the reduction procedure, the recalculated temperature-dependent Raman spectra obtained through the z(xx)z polarization are presented in Figure 4.11. A similar procedure was performed for other data but due to the highest similarity of the data were not summarized. One can therefore, observe the shift of the main bands, modification of their intensity as well as broadening of Raman features which imply a decrease in the number of bands obtained due to the fitting procedure during the rise of temperature (Figure 4.11). Interesting behavior was observed in the case of bands assigned to unsaturated Nb=O bonds and Nb-O-Nb bridging bonds within niobia octahedra (Figure 4.13).

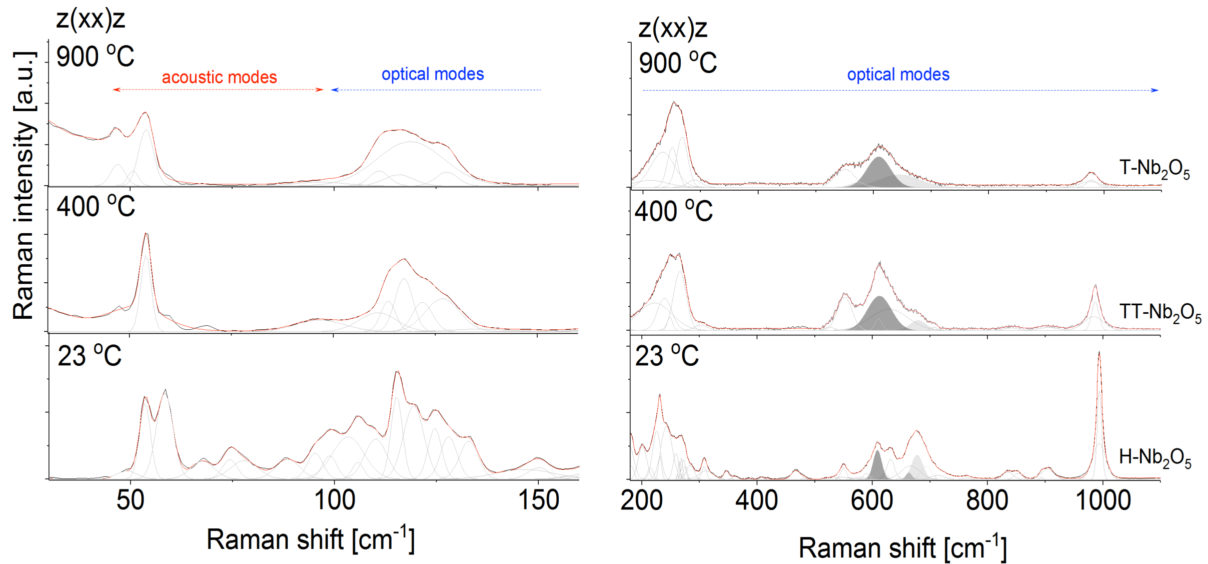

Figure 4.11 Temperature-dependent in situ polarized Raman spectra of the H-Nb_2O_5 single crystal oriented along the z-axis and measured at z(xx)z polarization. The band fitting analysis were performed using Grams Software package. The different polyhedra were color-highlighted: dark gray means corner-shared, gray - slightly deformed edge-shared and light gray - highly distorted niobia octahedra. Acoustic and optical modes were described, respectively by red- and blue-arrows in the range below 100 $cm^{-1}$and in the 100 - 1100 cm^{-1} range.

The position of these bands gradually red-shifted. The temperature-evolution might be correlated to the monotonic function depending on the anharmonic coefficients ascribed

to the properties of the decay process taking place due to the thermal effect on the structure of niobium oxide (177). As a result such modification might be described using the theory prediction given by the equation (178) :

$$\nu(T) = \nu_0 + C\left[1 + \frac{2}{\exp^{\frac{\hbar\nu_0}{2k_BT}} - 1}\right] + D\left[1 + \frac{3}{\exp^{\frac{\hbar\nu_0}{3k_BT}} - 1} + \frac{3}{\left(\exp^{\frac{\hbar\nu_0}{3k_BT}} - 1\right)^2}\right]$$

where ν_0,C and D are anharmonic coefficients obtained by three- and four-phonon processes, $\hbar$ – Planck constant, k_B – Boltzmann constant, T – temperature.

Hence, the evolution of terminal Nb=O bond changes with ν_0= 993cm^{-1} , C =-0.17cm^{-1} and D =-0.03cm^{-1} corresponds well to data presented in literature (177). In turn, the position of the band of NbO_6 is changes with ν_0= 664 cm^{-1}, while C =-1.11 cm^{-1} with the anharmonic coefficient D = 0 indicates the three-phonon process responsible for the wavenumber shift. Moreover, the position of this band is red-shifted for temperatures up to about 700 °C with the blue-shift band for higher temperatures.

This behavior might result from a structural phase transition which according to literature data, corresponds to the transformation of niobium oxide phases into an oxygen-defected T-phase. The change in the character of the band position evolution indicates a strong structural rearrangement. According to XRD results in this modification resulted from an increase of the number of structural point defects and formation of different polyhedra as distorted octahedra or pentagonal bipyramids joined by edge- and corner-sharing (in XY plane) and by corner-sharing along z-axis (179). Interestingly, in turn, the analysis of bands assigned to the O-Nb-O modes centered at a lower wavenumber. Here, two different temperature-evolution trends were found. The band at 305 cm^{-1} progressively shifted towards lower wavenumbers from 23 °C to 300 °C, then its position is practically unaffected by temperatures even up to 700°C and above this temperature the band again gradually red-shifted towards 302 cm^{-1} for temperatures up to 900°C. As one can easily recognized, the shift is not fully monotonic as in the case of previously described Nb=O and cannot be fully described by the theory. Hence, this evolution cannot be related to a normal anharmonic effect of an optical phonon. Similar behavior was found for the band centered at 299 cm^{-1} observed for the original H-Nb_2O_5. Here, the band position is red-shifted up to 233 cm^{-1} at 573 K while above this

temperature the opposite trend results from the blue-shift of the O-Nb-O band and probably suggest some structural modification. These results are well correlated with previously reported data presented in literature (177,179,180,181) indicating the transformation of the origin monoclinic H-Nb_2O_5 into pseudohexagonal TT-Nb_2O_5 phase. It is also worth noting that the different band position evolution of the two low-lying bands confirms the different type of polyhedra building the crystal structure of niobium oxide. Here, the evolution of high wavenumber band close to monotonic function indicates only slight structural modification of the edge-shared niobia octahedra in relation to corner-shared units which during the transformation undergo a stronger rearrangement. This behavior is in accordance with expectations for the TT-phase which, enforces structural arrangement and formation of oxygen deficiency distorted octahedra with the Nb-O-Nb-O chain structure observed along the z-axis. This structure is characterized by the edge-sharing tetra-, penta-, or hexagonal bipyramidal units (NbO_6, NbO_7, NbO_8 units) (179,182). This modification in tetrahedral units might also be seen in the low-wavenumber region where bands primarily assigned to the vibration of Nb-Nb are lowering in intensity. The presence of atypical structural units is also reflected through the broadening of Raman features (Figure 4.11).

Finally, an interesting situation was found in the acoustic mode region where with an increase of temperature the intensity of most bands decreases, indicating strong structural reorganization which practically implies inactivation of acoustic modes. The band at about 50 cm^{-1} might have another origin and according to some reports might be correlated with the appearance of a Boson peak usually associated with the existence of intermediate range order (IRO) typically for the glass or non-ordered phases. Likewise, this is commonly absent in the materials with the crystalline structures (183,184). The Boson peak usually appears due to an increase in the vibrational density of states above the Debye value, caused by localized excitations (phonon localizations).

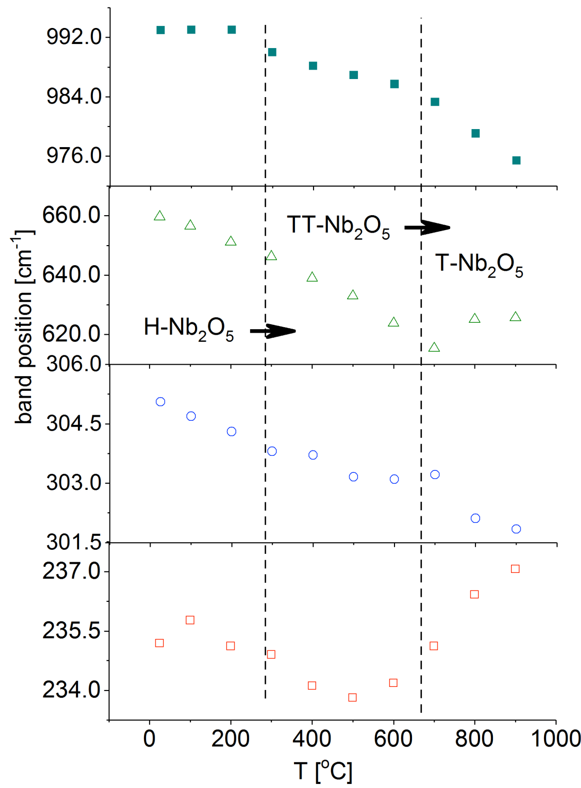

Figure 4.12 The temperature evolution of the band position of a) terminal Nb=O, b) Nb–O–Nb bridging bond in NbO_6,and c,d) O-Nb-O bridging bond in NbO_6 for the H-Nb_2O_5phase. The data are presented for z(xx)z polarization. The expected behavior by theory of phonon anharmonicity are red-line highlighted.

The appearance of Boson peak might be interpreted in terms of its relationship to the amplitude and extent of the density fluctuations in low-ordered materials.

To look more closely at the structural modifications and correlate these changes with the temperature evolution of the Raman spectra, the integrated intensity analysis for main bands correlated with different niobia octahedra were thoroughly investigated (Figure 4.11and Figure 4.13). First, the Nb=O bond undergoes interesting behavior, clearly highlighted in the form of two kinks at temperatures of about ~ 400°C and ~ 800°C and correlates with structural phase transition between crystalline defected H-Nb_2O_5 structures. Hypothetically that alteration might be described according to the following scheme:

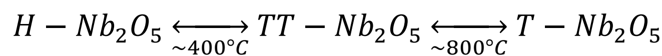

$$H - Nb_2O_5 \underset{\sim 400°C}{\longleftrightarrow} TT - Nb_2O_5 \underset{\sim 800°C}{\longleftrightarrow} T - Nb_2O_5$$

A significant increase of the integrated intensity value of the Nb=O in the temperature range of 400°C – 800°C is strongly correlated with the formation of the bipyramidal structures. This data refers to the significant role of Nb=O groups at the initiation of

structural rearrangement, niobia ion movements from its initial positions and formation of more ordered crystal structure with niobia polyhedra joined only by edge-shared units. Furthermore, a similar value of the Nb=O band analysis for H- and T-phase might be evidenced by corner-shared units joining different polyhedra. More precise analysis of the bands originating from the Nb-O-Nb vibration give an opportunity to follow the evolution of various structural units depending on the degree of octahedra distortion and type of octahedra. A similar trend was found for the distorted and slightly distorted edge-shared $(NbO_6)_{es}$ (620 - 680 cm^{-1} and 680 - 720 cm^{-1}) and corner-shared units $(NbO_6)_{es}$. However, while the temperature evolution of integrated intensity of both $(NbO_6)_{es}$ progressively lowers in value up to about 300°C , only slight changes within $(NbO_6)_{cs}$ occurred. This suggests at structural reorganization and rearrangement in the angular deformation of the edge-shared units wherein the corner-shared moieties are practically insensitive to a rise of temperature.

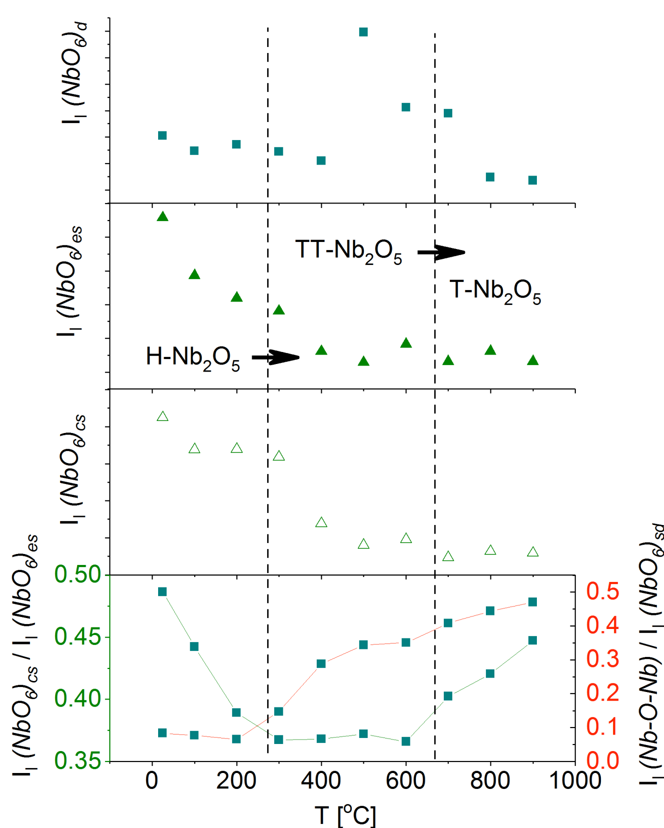

Figure 4.13 Temperature evolution of the integral intensity of bands assigned to different niobia polyhedra a) terminal Nb=O, b) edge-shared $(NbO_6)_{es}$ (620 - 680 cm^{-1}), c) corner-shared $(NbO_6)_{cs}$ (560 - 620 cm^{-1}) as well as d) correlation between integrated intensity analysis for niobia polyhedra presented in the form of the ratio: $(NbO_6)_{cs}$ / $(NbO_6)_{es}$ (green line) and (O-Nb-O) / $(NbO_6)_{sd}$ (red line).The data are presented for z(xx)z polarization

Some modification in the integrated intensity values detected above this temperature probably result from the structural transformation of H-Nb_2O_5 to TT-phase and are well correlated with the temperature-evolution of the band position (Figure 4.12 and Figure 4.13). Here, one can find a significant decline in the values for corner-shared units and only slight changes within edge-shared octahedra.

This might be linked to structural data resulting from the presence of octahedra and pentagonal bipyramid structures constituting the structure of the TT-Nb_2O_5. Further increase of the temperature influences the gradual decline of the integrated intensity value linked to the $(NbO_6)_{cs}$ with relatively constant value for $(NbO_6)_{cs}$ as a result of the transformation of corner-shared units to the oxygen-distorted edge-shared units. This trend is followed up to 700°C where as an effect of the TT-phase transformation to T-phase, only a slight increase in the value is observed. This may be visible in the case of the temperature-evolution behavior of the ratio: $(NbO_6)_{cs}$ / $(NbO_6)_{es}$ (Figure 4.13). In turn, by following the temperature profile created on the basis of the integrated intensity of the O-Nb-O bridging band in relation to the $(NbO_6)_{cs}$ a gradual increase of the value evidences the rearrangement linked to the lengthening of the Nb-O bonds. This corresponds to formation of an atypical niobia oxide polyhedra and correlates with the analysis mentioned above of band position evolution. It is worth noting that all observed changes are reversible after sample cooling which illustrates that structural phase transformation is reversible and is characteristic only for high temperatures.

4.1.3 Surface composition and electronic structure

The most powerful tool to examine the surface composition and provide the possibility to determine the electronic structure is X-ray photoelectron spectroscopy. As mentioned in Chapter 3 Sec. 3.1, all temperature dependent measurements were obtained in a UHV environment with a starting point of 25°C. The XPS spectra were recorded at 25°C, 200 ° C, 400 ° C, 600 ° C, 800 °C and 1000 ° C.

At room temperature, the oxygen spectrum O1s contains surface adsorbates (Figure 4.15) and shows two additional peaks related to OH/H_2O and CO/CO_2 molecules. However, the surface contains carbon and silicon (Figure 4.14) which absorbed from the air. At 400 °C the number of adsorbates was significantly reduced. A reduction of physisorbates took place already at 200° C. The niobium Nb3d state in the crystal indicated only the presence of state Nb^{5+}. The Nb3d doublet indicated a spectrum characteristic for Nb_2O_5. Also, the

valence band spectrum (Figure 4.16) showed the shape characteristic for this compound. The O1s line position is 530.9eV which also corresponds to Nb_2O_5 (185)(Figure 4.15).

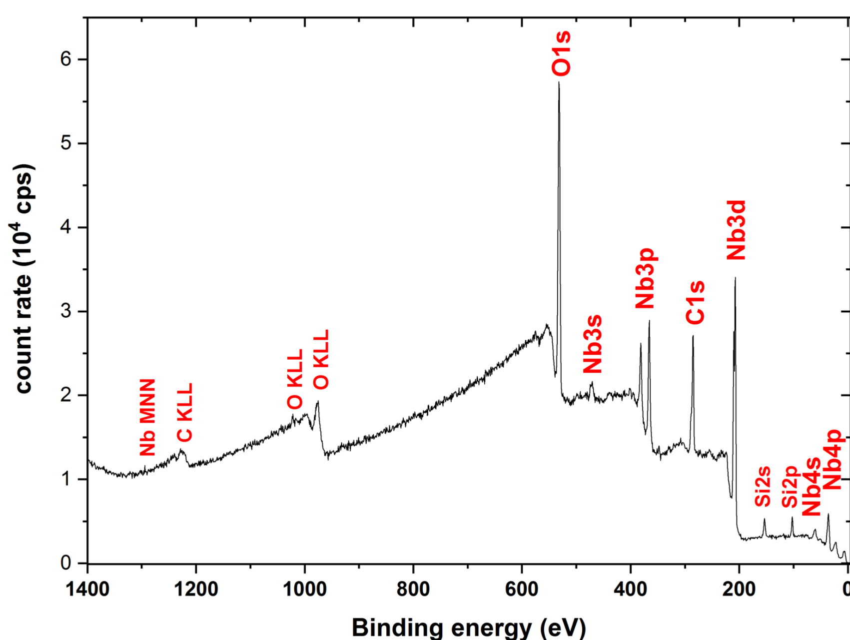

Figure 4.14 Overview spectrum of H-Nb_2O_5 obtained in the room temperature

After the annealing process, the position of the peak's characteristic for Nb^{5+} state was changed only by 0.05eV towards higher binding energies. However, at 200°C it was found that the Nb in the +4 state, with binding energy corresponding to 206.05eV (186) is present. The concentration of Nb^{+4} state increased from 0.25% at 200°C to 5% at 1000 °C. The ratio of the main Nb doublet increase with an increase of the temperature.

The analysis of the ratio of chemical composition O/Nb (Figure 4.17) revealed insulator to semiconductor transition on the surface layer. The starting value at room temperature which was close to 4.0 decreased to 2.1 for 1000° C. However, after the cooling down process the value was close to 2.5, which is probably a result of removing surface adsorbates during heating and diffusion of oxygen to the surface from the deeper atomic layers during cooling. This process may lead to the correct stoichiometry of the oxide after cooling down the crystal. Another reason for decreased O/Nb ration can be related to the reversible structural transition which was observed in the XRD and Raman spectroscopy studies.

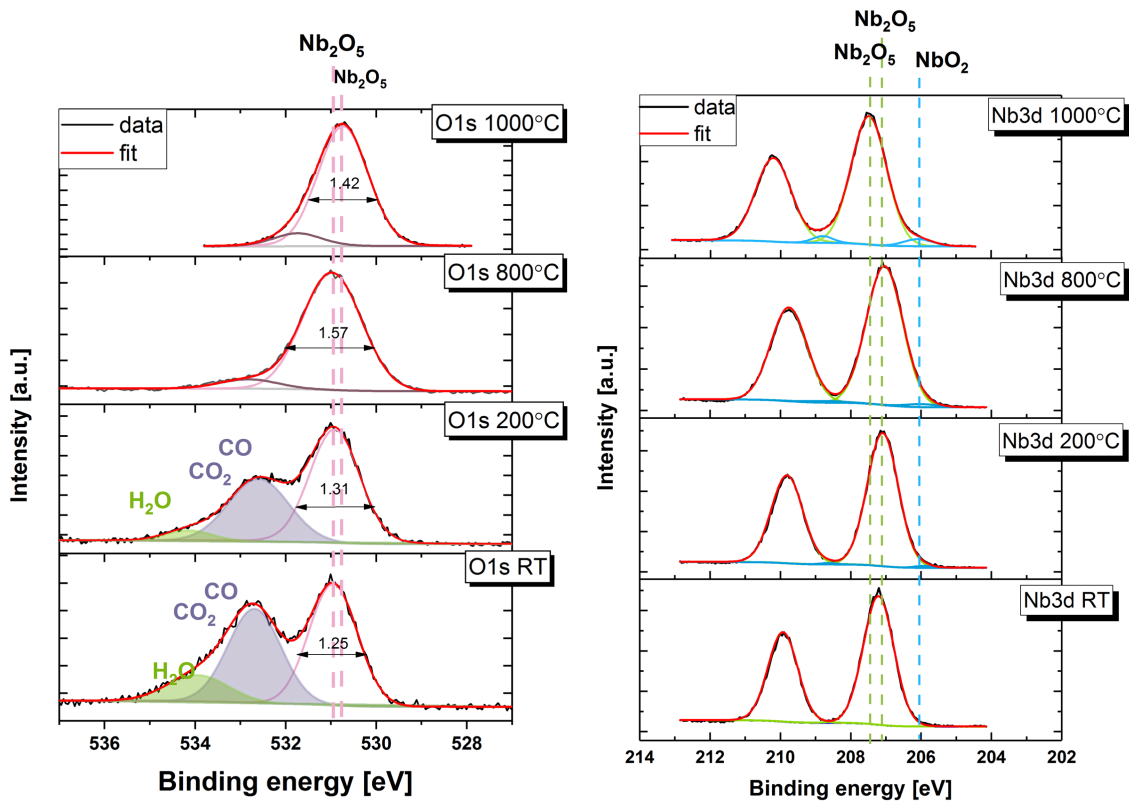

Figure 4.15 XPS selected temperature data for Nb3d and O1s lines

Finally, interesting information was obtained from the valence band (VB) spectra of the Nb_2O_5 single crystal surface. Figure 4.16 shows that up to 800° C the spectra corresponds to insulator behavior of Nb_2O_5 (187). At 1000° C the VB is slightly changed creating new states in the energy gap region for binding energies in the 0-2 eV range.

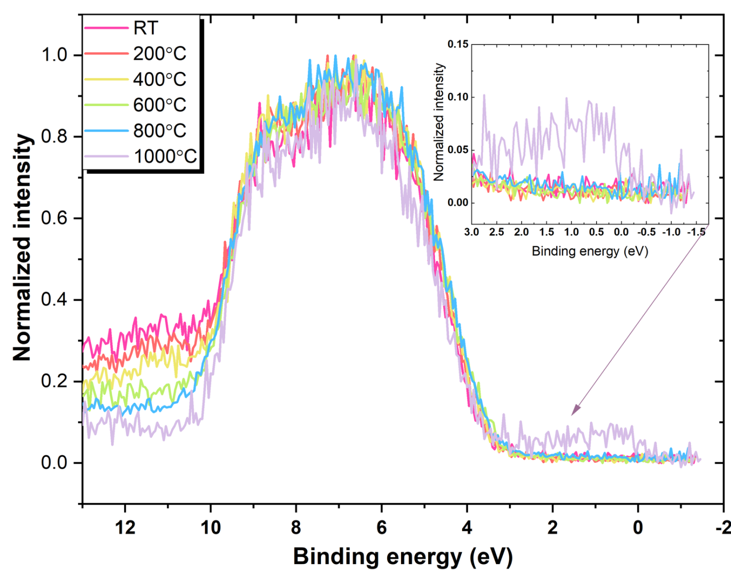

Figure 4.16 Temperature Valence Band dependence in the single crystal

These states can be related to the Nb^{4+} state. Semiconductor behavior corresponding to NbO_2 is confirmed. The effect of temperature induced reduction of the Nb_2O_5 crystal is generally weak. It is possible that lower partial oxygen pressure in the XPS analysis chamber is necessary to induce stronger reduction of Nb valence state.

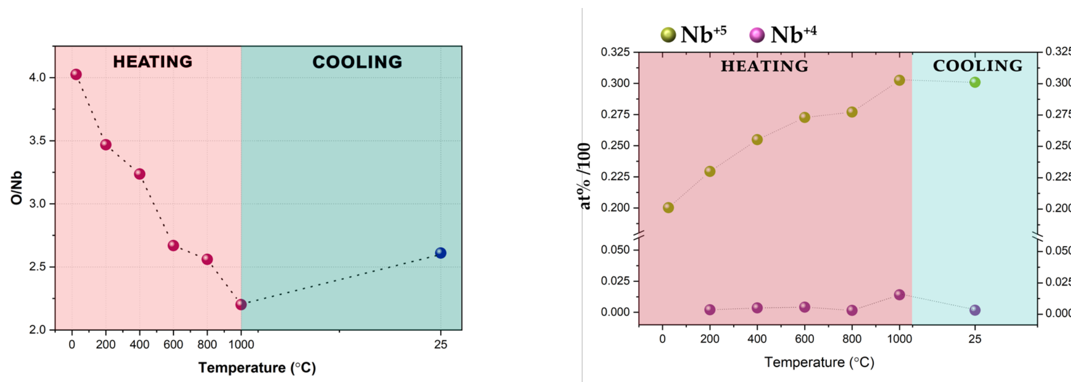

Figure 4.17 The chemical composition as a function of reduction temperature in Nb_2O_5, the O/Nb and valences ratios.

4.1.4 LC-AFM measurements

One of the fundamental processes in the resistive switching devices based on functional oxides is electronic transport. To better understand the process, local - conductivity force microscopy (LC-AFM) was chosen. This technique permits investigation the topography and the conductivity using a conducting tip (in the presented studies, two different Pt-Ir coated and diamond tips were used) in the contact mode (Chap. 3 Sec. 3.4)

The crystal of Nb_2O_5 was measured in the UHV condition at room temperature after cleaving in the air and annealing up to 600° C. The collected images were taken after annealing crystal at 100° C, 600° C at room temperature.

In Figure 4.18 the results obtained at 25° C from H-Nb_2O_5 cleaved in air have been combined. In the area of 500nm x 500nm the topography changes up of 1nm were observed. After applying +5V to the diamond tip, the surface exhibited very high resistance with the current reaching maximal value of about 0.5 pA.

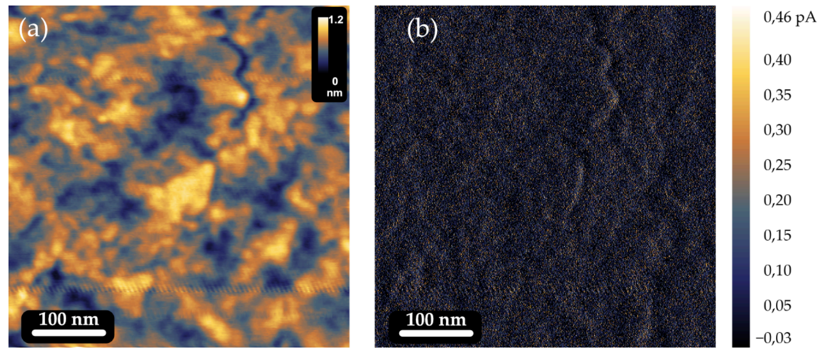

Figure 4.18 Topography and local conductivity of cleaved H-Nb2O5 obtained at room temperature.

The other data were collected from the surface of the crystal stored in UHV after cleaving for 72 h. The data were collected at room temperature (Figure 4.21 right upper corner). The topography map revealed a surface roughness of 0.225 nm. The local conductance map showed conduct points heterogeneously located on the analyzed surface with a local current of the order of 3.87pA. The local I-V curve is shown in Figure 4.21 (right upper corner). This was measured while the tip was in contact with the surface on the fixed point (12). The current at this point had a small value. However, the I/V curve revealed bipolar-like switching. Next (Figure 4.21 right bottom corner and left side of the picture), the crystal was reduced to temperatures of 100° C and 600° C and again the measurements were preformed after cooling down the sample - the data were then recorded at room temperature.

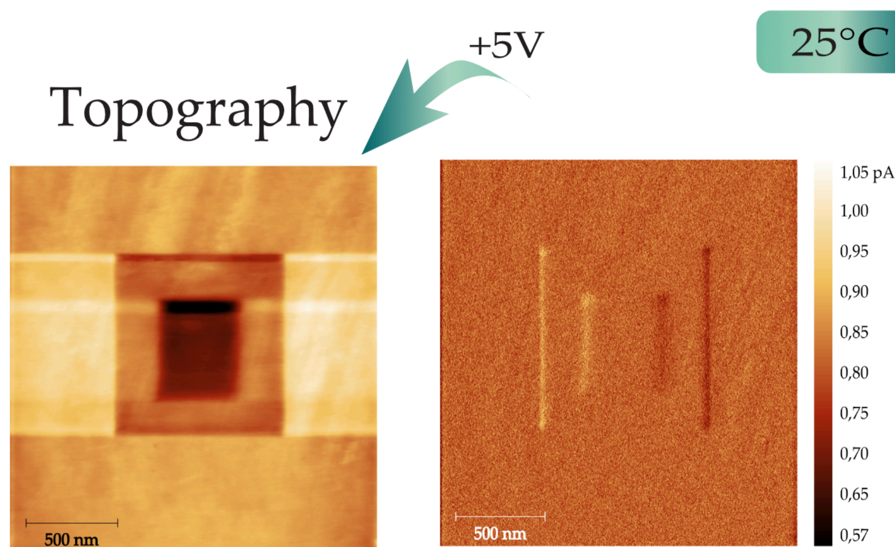

Figure 4.19 The following 1500x1500nm area were collected before the reduction process. The parament changes are observed on the crystal surface. The oxygen ion was extracted from the surface by the tip and the scan area was decomposed.

After reduction at 100 °C the topography map showed areas with the terraces with average steps equal to 2.45nm. The edge of those terraces can also be seen in the current map. The conductive fringes had significantly higher conductivity than surrounding material. After reduction at the last annealing point (600°C) the topography of the crystal also showed places with the terraces and striped pattern. However, at this time, after such treatment voltage bias was applied to the surface in diverse sign (± 1V).

Figure 4.20 shows an LC-AFM scan which proves the possibility of switching to the ON- and OFF- state at the described conditions. This effect can be observed at room temperature, but the applied voltage bias must be higher and be approximately equal to ± 5V (Figure 4.21). The effect of resistive switching on crystal reduced to 600°C is observed to a small extent, although minima current with a maximum of 0.3 nA were recorded. The distribution of the conductive spots is homogenous, but the edges of terraces exhibit different behavior, in contrast to the previous one. The hysteresis recorded in this area showed common behavior to previous one observed at room temperature. It is worth mentioning here that all presented data were collected by diamond tip. After switching the tip to Pt/Ir, the areas of the crystal surface which were not formed by diamond tip were analyzed. Places with terraces were again found. In those areas, the conductive maps looked different than the ones previously measured (Figure 4.21 left side of picture, and Figure 4.22).

The edges of the striped pattern are conductive (Figure 4.21left bottom corner). Also, with the use of the Pt/Ir tip, the switched ON/OFF- state was recorded (Figure 4.20). The forming area is not densely packed, but the current is ten times higher than in the area observed with the diamond tip. Despite the vast change in morphology, the average of local resistance from the current map did not show significant change with the annealing temperature; the conductive mechanism was unchanged. Resistance locally was changed with the temperature (Figure 4.22). The resistance decreases after annealing at 100°C. However, the opposite situation is observed after reduction of the crystal at 600°C. There are areas where resistivity locally is the order of 32 GΩ.

after reduction in 600°C

Topography

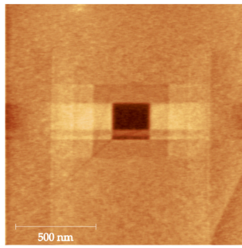

±0.5V

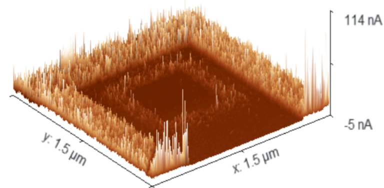

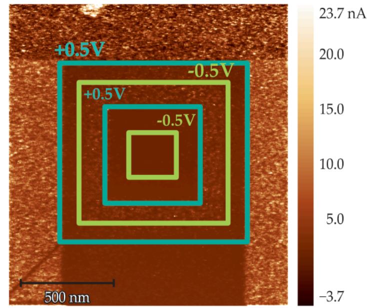

Pt/Ir tip

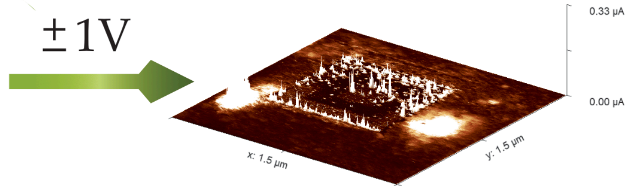

Topography

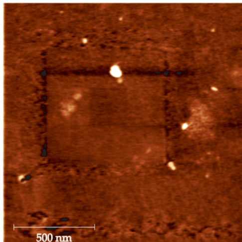

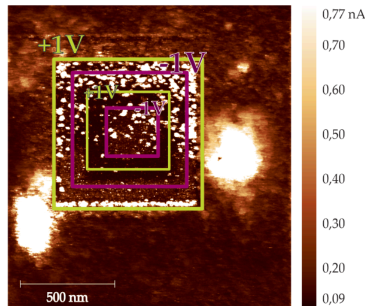

Figure 4.20 The ON/OFF state revealed by different voltage bias applied after crystal reduction at 600 °C. The forming process was obtained for two different tips: diamond (above part of the figure) and Pt/Ir (bottom part of figure).

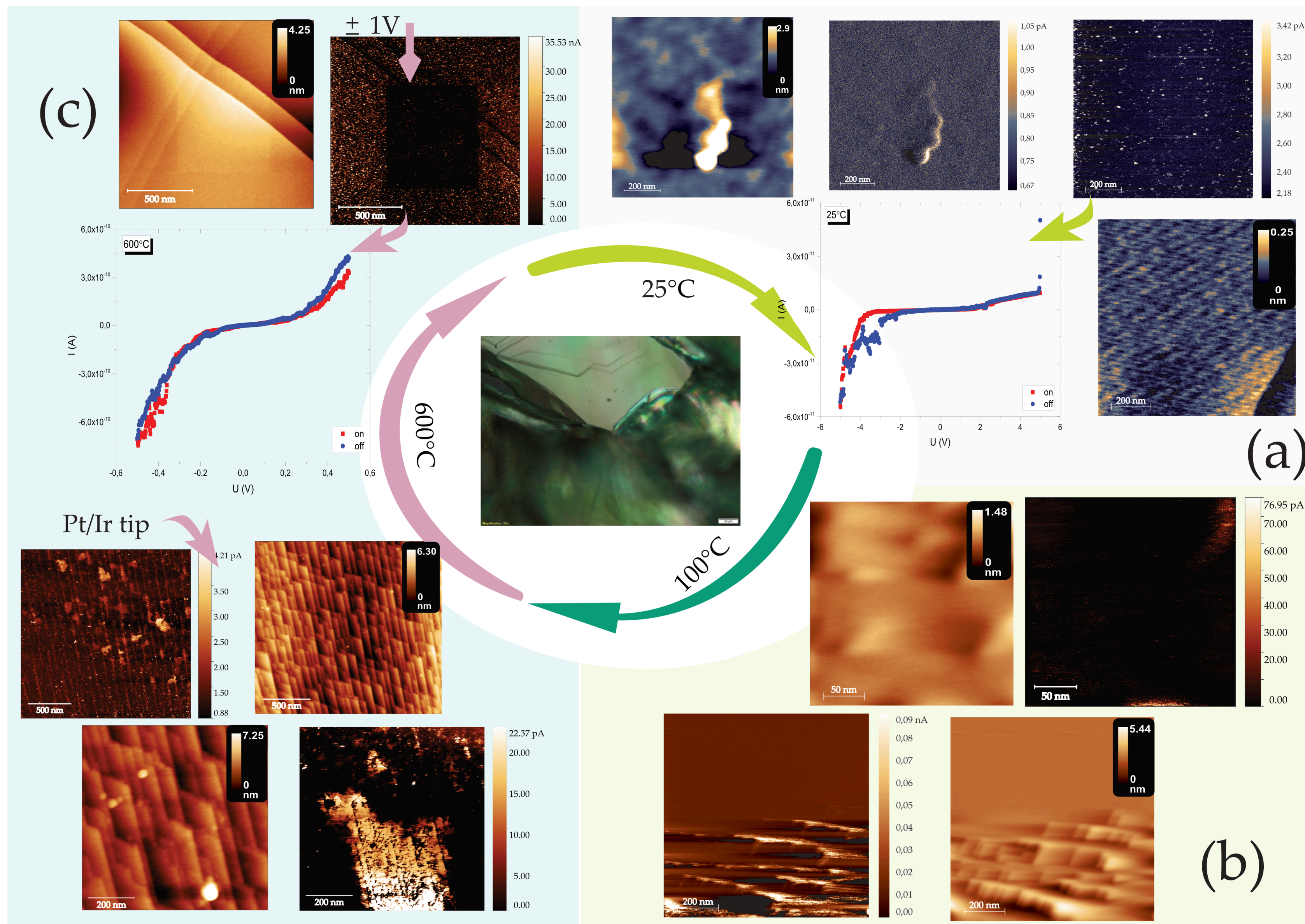

Figure 4.21 The topography and conductive map obtained at (a)25 ℃, (b)100 ℃ and (c) 600 ℃ reduction temperature. A diamond and Pt/Ir tip were used. The I-V curves were collected before and after annealing at room temperature (left and right corner, respectively). The forming process presented in the left corner start in the area of 1000x1000 nm with applying positive potential on the tip, then the area was reduced to 750x750nm and the applied potential was negative. The last area was

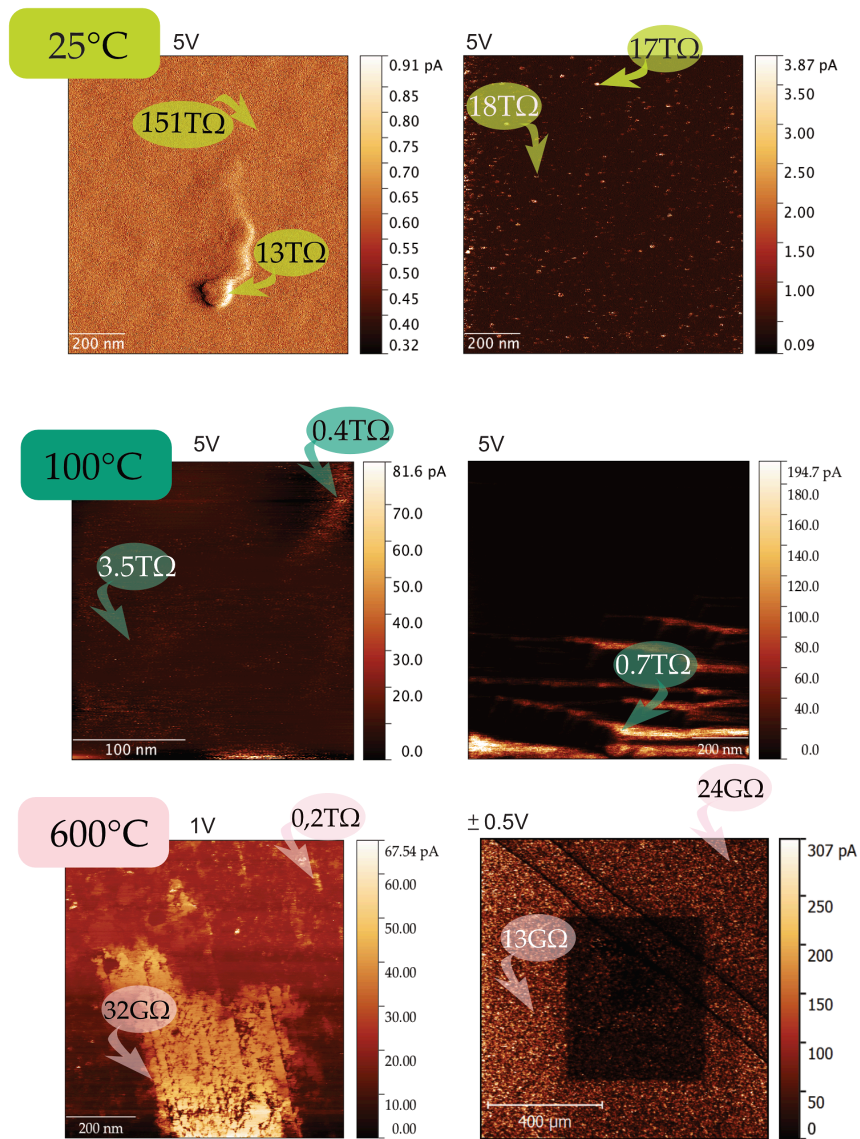

Figure 4.22 Local conductivity map collected before and after annealing at the room temperature for the crystal.

4.2 Niobium and tantalum oxide thin film

Today, the most applicable systems in nanometer scale are thin layers. Hence as mentioned in an earlier part of this dissertation this point focused on niobium and tantalum oxide thin films obtained by RF sputtering technique.

4.2.1 Nb-O thin film basic properties

4.2.1.1 Thickness and layer determination

The first step of the investigation was determining the crystallographic structure of niobium oxide thin films. The X-ray diffraction indicated the amorphous form of the deposited thin film as no diffraction peaks were observed when using the grazing incidence beam mode of diffraction studies. However, the x-ray reflectivity method showed very well-developed Kiessing fringes (Figure 4.23). The analysis of the results was performed with the use of Reflectivity 2000 software written by A. Gibaud and G. Vignaud. The main layer of the Nb-O film is almost 50 nm thick and has a density which can be attributed to NbO_2 (Figure 4.23). The pentoxide layer has a density which can be attributed to a high-temperature phase (H - Nb_2O_5) is placed over the NbO_2 layer and is much thinner (10 nm). The topmost layer has a slightly greater density than that of H - Nb_2O_5 and its assignment to pentoxide are based mostly on the XPS data presented below (Table 7) (188). The observed structure can be understood as a results of thin film growth which was divided into two stages – deposition of pure Nb film and then oxidation of the obtained film. The limited diffusion of oxygen into the film resulted in the formation of NbO_2 in the main part of the sample.

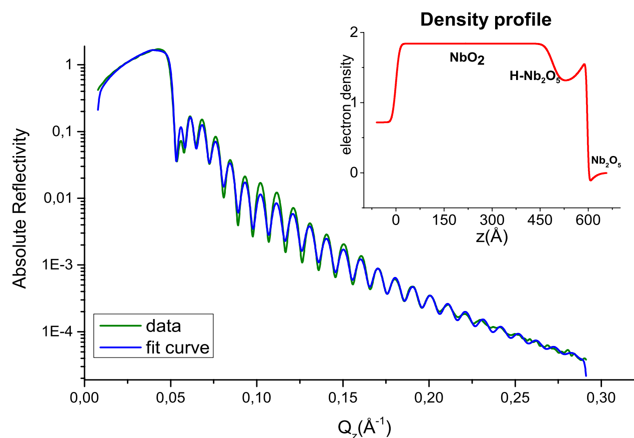

Figure 4.23 Result for XRR data with electron density profile.

	name	Critical wave vector q_c [Å^{-1}]	roughness [Å]	thickness of layers [Å]
substrate	Si	0.0318	8.89	
layer	NbO_2	0.0508	17.98	488.51
layer	H-Nb_2O_5	0.0427	28.21	98.05
layer	Nb_2O_5	0.0502	3.72	10.62

Table 7 Results of X-ray reflectivity for Nb-O thin film

4.2.1.2 Electronic structure and surface composition

The analysis of the Nb3d from the surface of the Nb-O thin film measured at room temperature indicates that niobium exists in Nb^{5+} state (Figure 4.25). The signal from the valence band (VB) region (Figure 4.25 b) also shows a shape characteristic for the Nb_2O_5 compound. The results for the previously measured Nb_2O_5 single crystal cleaved in UHV was chosen as the reference. Comparison of both systems generally shows the same Nb3d doublet and similar shape of the valence band. However, the single crystal exhibit more resolved structure in the binding energy region 6-9 eV and can be related to the long-range crystalline order. Moreover, after the annealing process, the VB spectra are transformed from insulator to being conductor - like in series $Nb_2O_5 \rightarrow NbO_2 \rightarrow NbO$. Similar behavior of the Nb-O thin film surface was reported by Kuznetsov et al. (187). At 150°C the Nb3d doublet started to slightly change. Intensive broadening of the Nb3d line is observed at 300°C. The doublet with binding energies 206.8eV and 209.5eV corresponding to the lower Nb oxidation state appeared. However, these energies are higher than reported for NbO (186). At higher temperatures the situation changed completely. The dominating phase is NbO with binding energy of the Nb $3d_{5/2}$ peak 204.5eV. It is worth to mention that Jung et al. (122) reported that similar energy to this one corresponding to NbO_x was observed after electroforming process (low resistance state). Furthermore, the analysis of Nb3d line at 600° C indicated the presence of NbO_2 and Nb_2O_5 with binding energy of Nb $3d_{5/2}$ peak at 205.9 and 207.9eV, respectively (Figure 4.24). In the thin film form, the O/Nb ratio starts from a value close to 2.5 and decreases with temperature to about 1.5. Similar, to the Nb3d line the O1s line slightly changes with an increase of temperature (Figure 4.25d). Moreover, the shift of the main Nb3d doublet (Figure 4.25a) is shifted from the highest Nb oxidation states towards lower

binding energies. This can be caused by gradual breaking of the Nb-O bands, starting from the weakest ones, which can be attributed to the longest Nb-O distance. The content of the surface oxygen is strongly reduced after thermal treatment. The decreasing oxygen amount caused a relative change in binding energy of Nb photoemission lines due to the Nb^{5+}-O bonds which can be shorter than in the single crystal (Figure 4.26). Comparing the surface behavior after reduction process in both Nb-O systems - single crystal and thin film one can observe a much faster process of migration of oxygen anions in the thin film than in the single crystal.

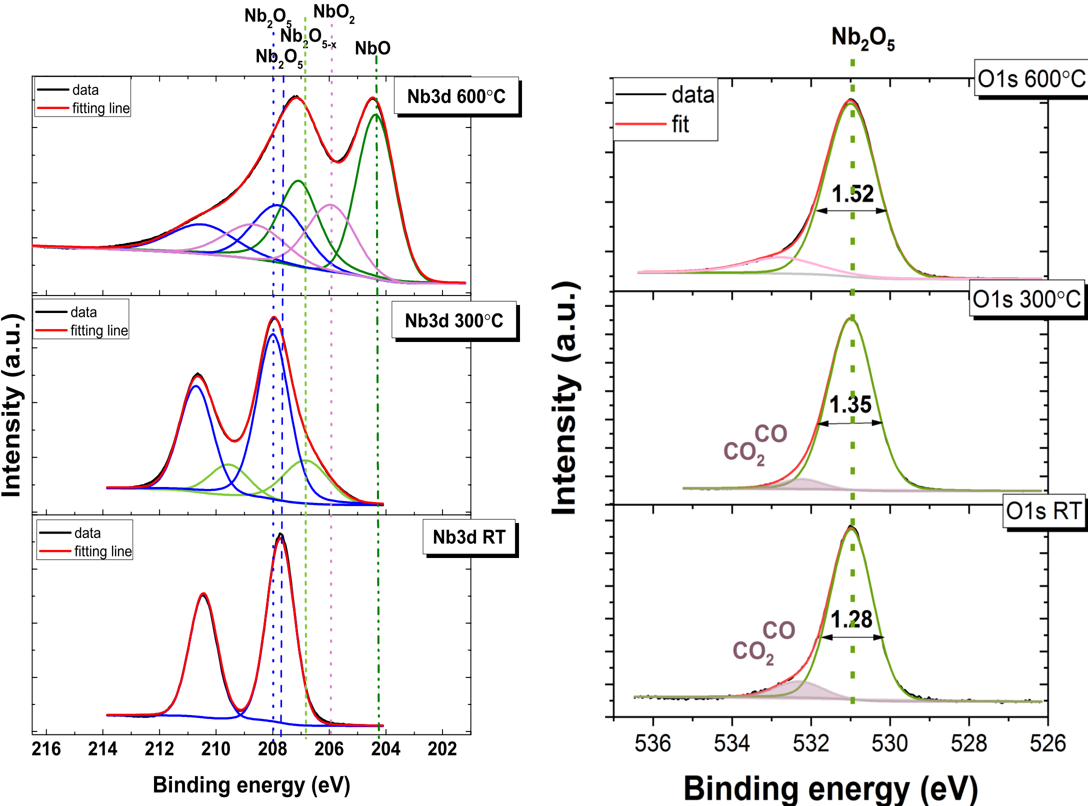

Figure 4.24 Result for fitting the XPS spectra for Nb-O thin film obtained for selected temperature.

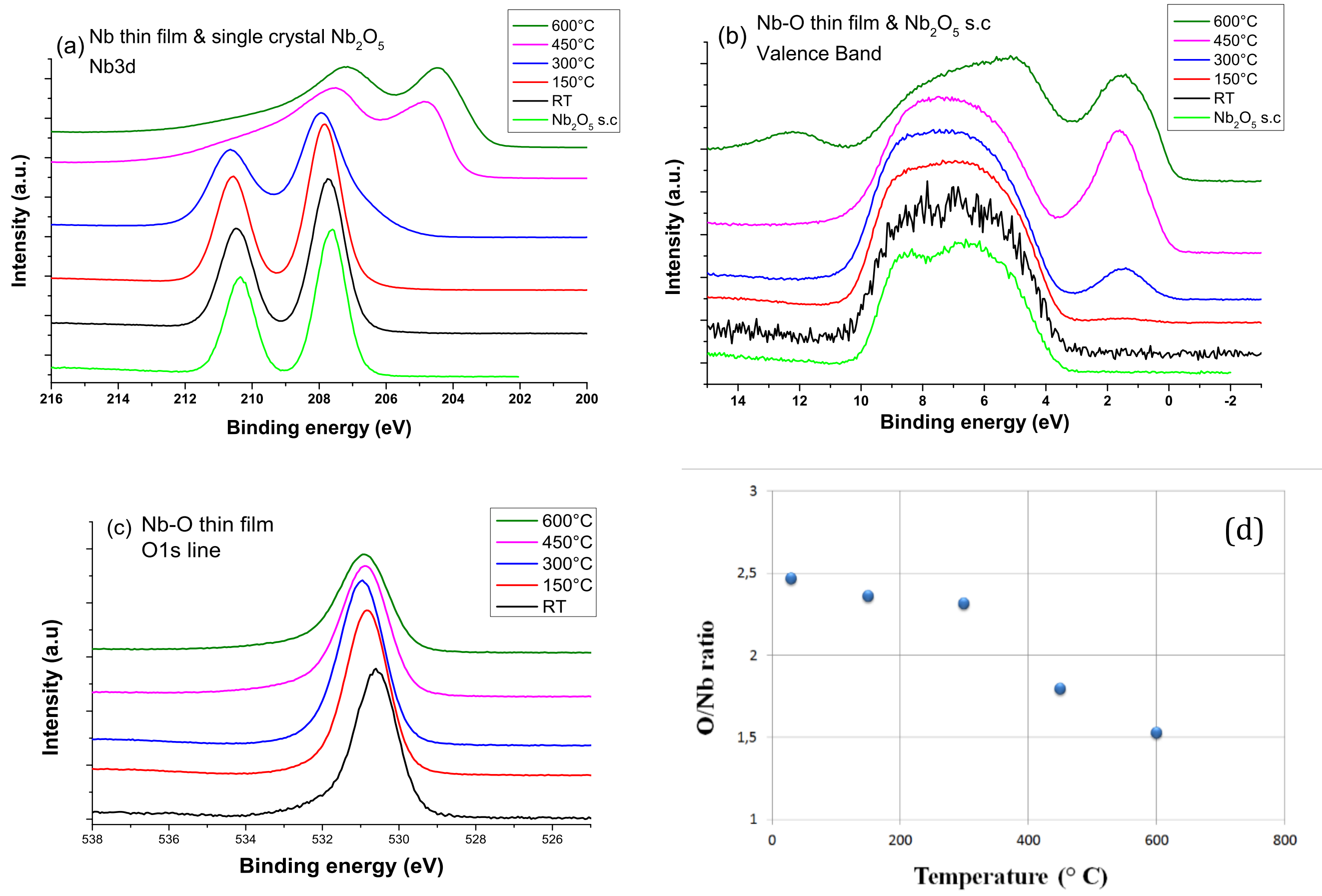

Figure 4.25 Temperature dependence of the photoemission spectra for the Nb-O thin film: (a) Nb3d doublet (b) valence band (c) O1s and (d) oxygen and niobium ratio derived from XPS spetra.

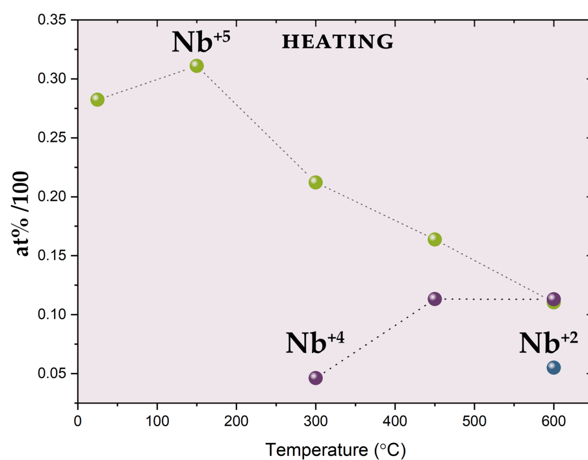

Figure 4.26 Valence ratios as a function of reduction temperature in Nb-O thin film

4.2.1.3 ToF-SIMS

A more complex surface analysis with chemical sensitivity higher than XPS, was realized using a Time-of-flight secondary ion mass spectrometer (TOF-SIMS.5). The analysis was focused on the distribution of selected ion species in the near surface region. To obtain such information the depth profiles were performed using a bismuth gun for the analysis and cesium gun for the depth profile. Applied dual mode was realized by alternating bombardment of the sample surface first by the primary - bismuth ion beam for the analysis and later the cesium beam for the surface sputtering. To obtain depth profile was bombardment repeated several hundred times. The chemical distribution maps were generated by rastering a finely focused primary ion beam across the sample's surface and through collecting a mass spectrum at each pixel (158). From the mass spectrum, particular ions were selected, and for them, the distribution maps at each step of the sputtering cycle were reconstructed. In this work two types of depth profiles are presented; the 3D depth profiles where distribution maps at each cycle of sputtering are directly presented and the linear profiles in which each point represents the total sum of the detected ion at a specified time of sputtering cycle over the analyzed area.

The analysis of the 3D depth profile was focused on both: distributions of elements within one cycle of the profile (2D distribution) as well as on observation of the behavior of particular ions in the sample depth. The main part of the depth profile analysis is based on the observation of distribution of the Nb-based ions in the analyzed sample. However, the issue of contamination has also been discussed in this chapter. This can be seen in measurements performed on both positive and negative polarities showing that the main structure niobium oxide grown on silicon has been preserved. It should be mentioned that measurements performed on the positive polarity give higher sensitivity for detection of Nb and some other elemental species like Na, Al, Si, whereas measurements performed on negative polarity enable more precise analysis of the oxide structure via analysis of $Nb_xO_y^-$ ions. Nevertheless, taking into account the above comments and results obtained in measurements from both polarities, within the Nb-O film region some inhomogeneity has been detected. The inhomogeneities occur during the etching of the surface of the film and indicate that the film consists of several types of oxides placed one above another or more precisely, transform one into another within the depth of the film. The results of the measurements in positive polarity indicate a similar distribution of Nb^+, NbO^+ and $Nb_2O_5^+$ ions in the characterized film. Those ions are generally located directly on the

silicon substrate of a thickness of about 3/4 of the thickness of the layer, then the intensity of the ions decrease and then again, on the surface of the layer an increased amount of these ions can be observed. Different distribution is observed for the Nb^{2+} ion; those ions are observed in the same area as the ones mentioned earlier but only on the bottom (3/4 thickness of the film placed directly on the silicon substrate) part of the layer. This may suggest that this region has a stable oxide structure that represents the position of homogenous Nb_2O_5 oxide. The analysis of 3D distribution maps obtained from measurements in negative polarity gives more information about the inhomogeneity of the oxide layer. The analysis was carried out taking into account some artifacts manifesting as spikes of the intensity of detected ions (well visible straight stripes with an increased concentration occurrence in the proximal area of silicon). $Nb^{-,}$ NbO^-, $Nb_2O_4^-$, NbO_2^- and $Nb_2O_3^-$ all exhibit similar behavior; they are present in the entire volume of the layer, although a clearly increased amount of these ions is visible in the area in which the amount of Nb^+, NbO^+ and $Nb_2O_5^+$ have been reduced in studies in the positive polarity. Sharp edges between those individual regions do not occur, which indicate that the particular layer converts from one to another. There is a slightly different distribution of the NbO_4^-, $Nb_2O_4^-$ and $Nb_2O_5^-$ ions in comparison to the above motioned ions that have been observed. In this case, the NbO_4^-, and $Nb_2O_5^-$ ions are present only on the surface of the analyzed film; it is worth mentioning that in the outermost surface region the Nb^-, $Nb_2O_3^-$ and $Nb_2O_4^-$ ions do not occur. The presence of Nb related ions in the silicon substrate may be results of implantation of those ions during the ionic etching.
Within the 2D structure, analyzed at each step of etching of the film is here presented as the sum of all measuring cycles (See row 2D on Figure 4.28and Figure 4.29) – uniform distribution of ions over 200x200 μm have been observed for $(NbO)^-$ ions.
The 2D distribution (Figure 4.28) for positive polarization show the surface contamination with Al^+, Ca^+, K^+ and Na^+. The observed surface impurities in Figure 4.28 such as e.g. Na^+ ions are placed non-homogenously on the surface of the analyzed sample. The exception from that behavior is the distribution of Ca^+ ions, where the presence of this contamination is clearly observed inside the analyzed film; however, the determination of the direction of the diffusion is not precise – Ca may diffuse through the film from the outermost surface, but also from the surface which lies under the analyzed film.

In the case of measurements performed in the negative polarization the $C_xH_y^-$ ions also associated with impurities were detected on the surface as well as under the film, which may indicate either preliminary contamination of the crystal surface or relatively easy diffusion of such ion through the Nb_2O_5 film (Figure 4.29). Figure 4.29 and Figure 4.30 2D show the linear representation of depth profile of ions derived from Nb_xO_y thin film from measurements performed in positive (Figure 4.28) and negative (Figure 4.29) polarization.

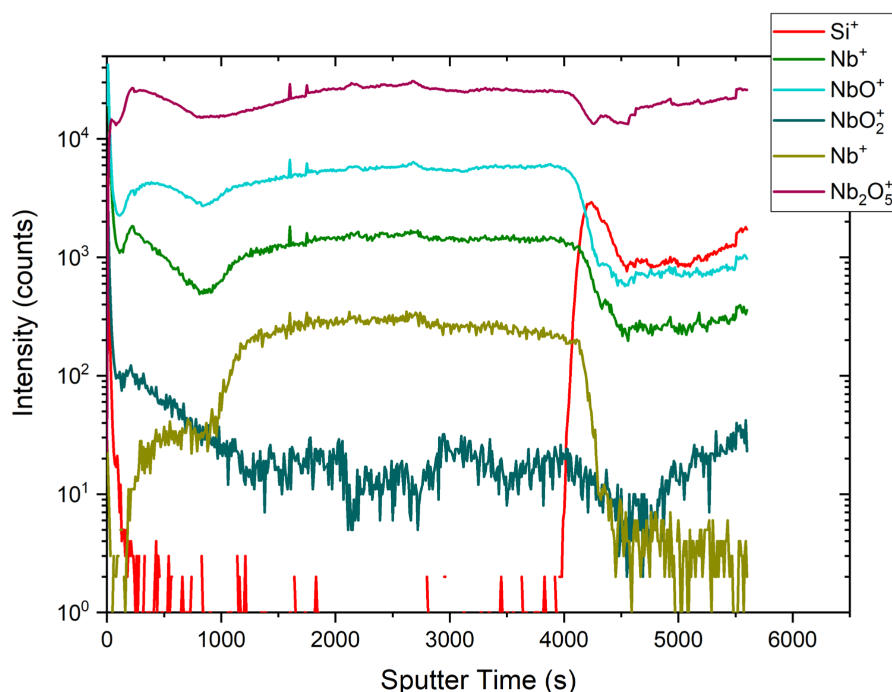

Figure 4.27 Depth profile obtained in positive polarity.

Linear representation of depth profile here presented as a number of detected ions given at the time of surface etching summarize the results discussed for the 3D distribution maps. For example, surface, silicon ions were present in high amount on the surface of the analyzed film. After a few etching steps they were removed and appeared again after the Nb-O film was etched. In the case of (Nb, O) ions, a few different regions must be analyzed. The near surface region (0-1000s of sample etching) is more complex; different (Nb,O) related ions have different distributions, especially in the near surface region: for example the amount of the Nb_2O_5+ ions increases in the first few steps of the etching process, whereas in case of NbO^+ or NbO_2^+ decreases.

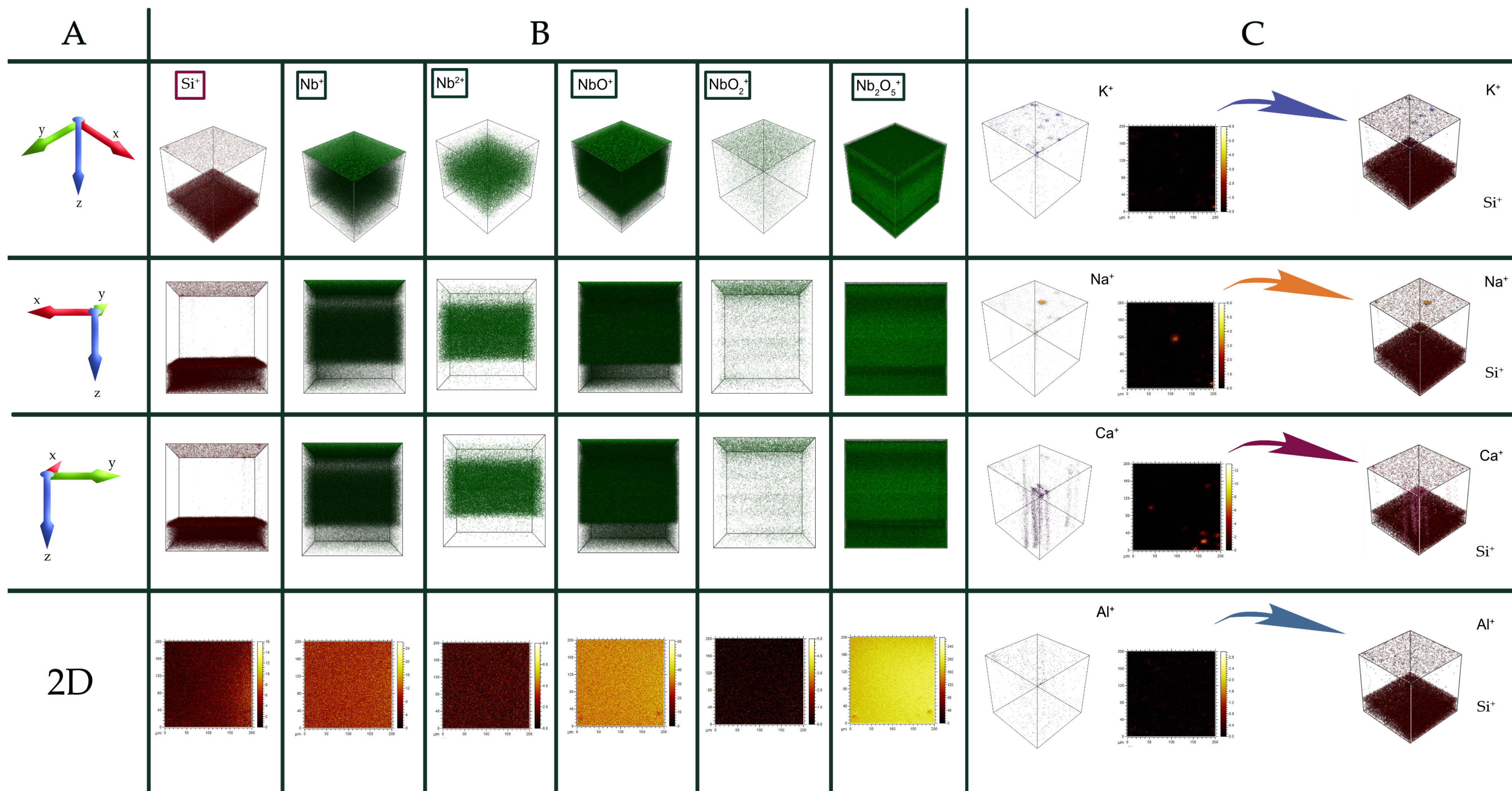

Figure 4.28 Distribution maps for selected ions measured in positive polarity for Nb_2O_5 film grown on Si. The graph represents three main columns: (A) where projection type has been specified, (B) with respective projections of particular ions, (C) 3D overlay of selected ions

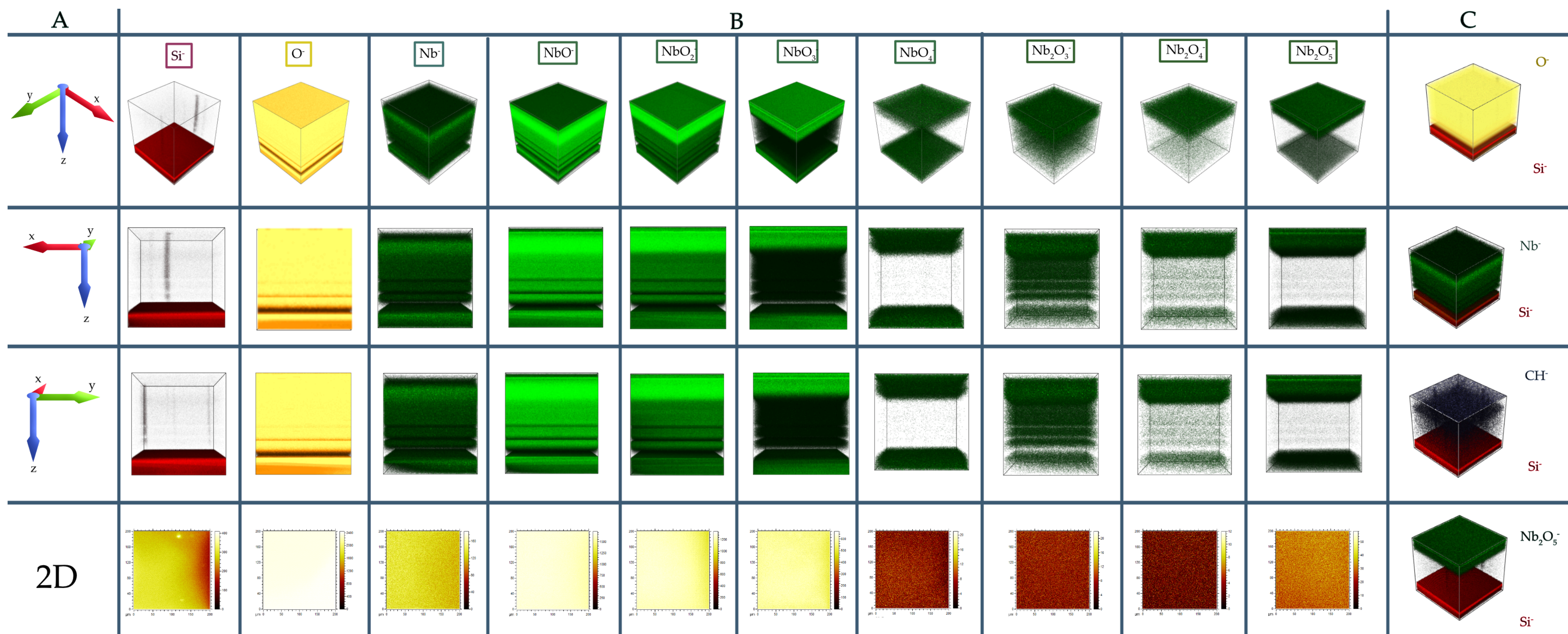

Figure 4.29 Distribution maps for selected ions measured in negative polarity for Nb_2O_5 film grown on Si. The graph represents three main columns: (A) where projection type has been specified, (B) with respective projections of particular ions, (C) 3D overlay of selected ions.

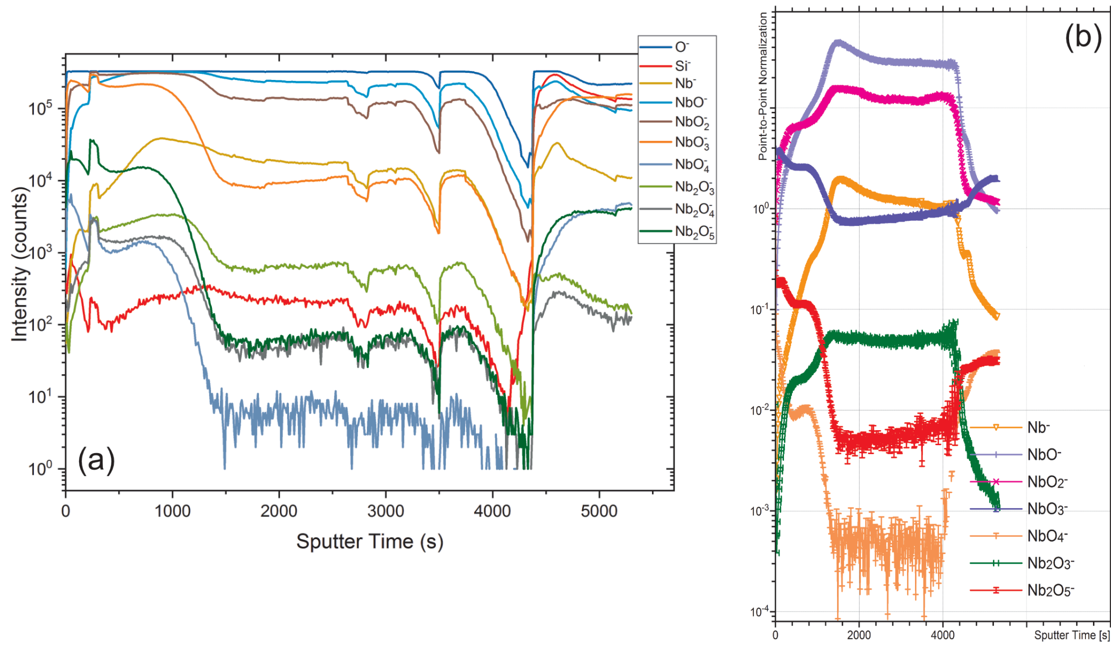

Figure 4.30 Depth profile obtained from measurements in negative polarity; (a) profile as measured, (b) profile after point by point normalization to the O^{2-} line.

The weak maximum is observed for the Nb_2O_5+ ions, then after the ~50'th cycle of sample etching all ions exhibit similar behavior; local minimum and later increase of the value of detected ions and then a later decrease in the number of detected ions. After around 1000s sample etchings, a uniform layer consisting of form Nb, and O appears and is present until it reaches the silicon substrate. In the case of measurements in negative polarity, also three main regions can be detected. The first is related to the near-surface region, the second which is present after around 1000s etchings and the third starts appearing around 1000s etchings and is present in the film until it reaches the silicone substrate. On Figure 4.30a profiles spikes are visible around 400s, 2800s, 3500s and 4500s and are artifacts that can be removed by normalizing the profile of particular ion to the O^{2-} profile (point by point normalization), such calculations were performed on the data and are presented ions in the Figure 4.30b.

Generally, similar to the case of profiles obtained from measurements in positive polarity, it can be concluded that the film has at layered structure and that the layers, although partially distinguishable, rather continuously follow each other. It seems that the different distribution of various Nb_xO_y species observed in the film suggest the presence of different types of Nb oxides. Presence of different types of oxides were also observed in the XRR measurements; the data are in good agreement with each other taking into

account the number of layers and their relative thickness (here roughly related to the sputtering time).

4.2.1.4 LC-AFM measurements

In the Nb-O thin films the conductive distribution path in the nanoscale plays the main role in the resistivity switching phenomena. The LC-AFM topography and the conductivity measurements were obtained using a conducting Pt-Ir-coated tip in contact mode with a highest spatial resolution, due to the confined potential drop below the contact area of the tip. The thin film was studied after heating under ultra-high vacuum conditions at annealing temperatures of 300°C, 450°C and 600°C for 8h in each case.

In Figure 4.31a and Figure 4.31d, the results obtained on Nb-O thin film are presented starting from an annealing temperature of 300°C. The center image shows the topography of the sample and at the top conductive map recorded with bias voltage 0.7 V. After annealing at 300°C the topography map revealed conductive grains (Figure 4.31.a) with a diameter of 30-70 nm.

After annealing at 450°C these inhomogeneous areas (Figure 4.31.b) size rise to 41% (118nm). During the last step of the annealing process at 600°C there is a different change. The size of the conductive grains decrease (Figure 4.31c) from 50 nm to 20 nm. Moreover, the distribution of the grains was more inhomogeneous and after annealing in this process there were more point areas with the highest conductivity of c.a 1.3MΩ, however applied voltage was 0.94V. Also, the RMS roughness (Figure 4.32) increases with annealing temperature.

The presented I-V curves (Figure 4.31.g-i) were collected in the points showing low resistance. The voltage necessary for switching between the low and high resistance state for both films is lower than 1 V (188). All resistance states show a linear behavior. The switching character was bipolar.

The area of 500 x 500 nm was scanned with the same reading voltage of 10mV. Figure 4.32a presents the modified area with writing voltage switched to the ON state. The conductive cluster is formed in the current range from O to 840nA (Figure 4.32a).

Figure 4.31Topography and local conductivity map obtained at 300 ℃, 450 ℃ and 600 ℃. The I-V curve with the conductive area with different current load.

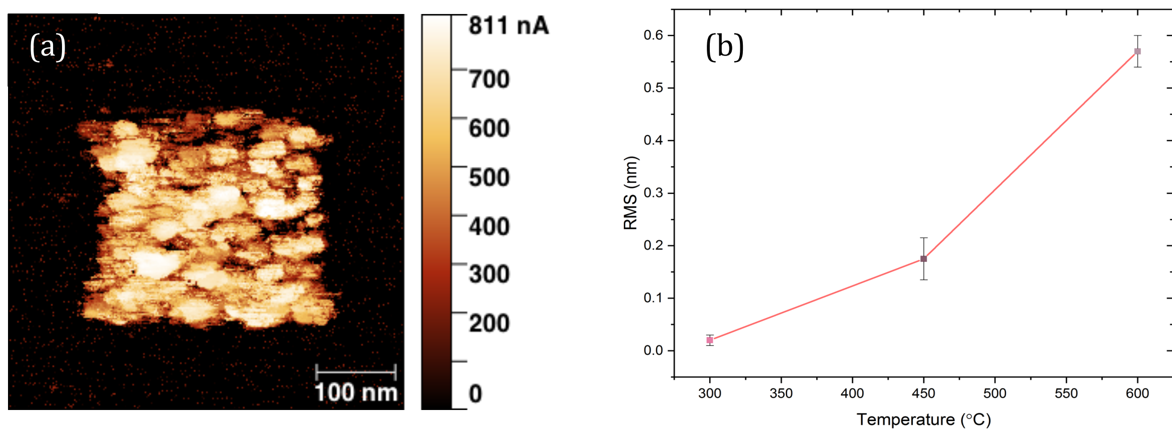

Figure 4.32 The picture presents (a) current map, where in the middel area are presented switched to the low resistance state (b). Roughness (RMS) obteined from the picture measured in the different temperature range.

4.2.2 Tantalum – oxide system

In late 2011 in the pages of Nature, Lee et al. (4) from Samsung Electronics showed new materials to build a ReRAM device. Those materials were tantalum oxides Ta_2O_{5-x} and TaO_{2-x}. Due to similarities in the electronic properties of Nb-O, the Ta-O system was chosen to check fundamental properties of the thin film without any metallic caplayer on the top. It is worth mentioning that the attempt to grow the Ta_2O_5 single crystal using the zone floating technique was not successful. Only a few literature studies (189) have shown that the growth of Ta_2O_5 single crystals is possible. Xu et al. and colleagues (189) obtained the Ta_2O_5 single crystal by zone floating technique and indicated that its crystal structure was tetragonal. However, within this thesis, only thin film is considered as the obtained crystals were not of sufficient quality to enable reasonable studies.

4.2.2.1 Thickness and layer determination

The Ta-O film appeared to be amorphous, similar to the result obtained for Nb-O thin film (20) (Figure 4.33). However, X-ray reflectivity measurements allowed to determine the structure and partly the composition of the thin film. As mentioned in chapter 2 sec. 2.2. this technique not only allows to build the thickness model of the thin film but also to determine electron density distribution with a connection to layers forming the films. All data were collected by Empyrean diffractometer from Panalytical and all calculations were realized with the use of Reflectivite 2000 software and X'Pert Reflectivity program
As Schmelzer mentioned in his dissertation (20) the Ta-O film was grown by partial oxidation of the metallic Ta surface. Hence the simulation of Kiessing fringes show that the metallic Ta buffer layer is covering the silicon substrate (Table 6). Next, the two main layers with two different stoichiometry of Ta_2O_5 were detected. The dominant one had 60.15nm of Ta_2O_5 layer corresponding to α-Ta_2O_5 (190) (191) and 4.77 nm thick Ta_2O_5 film was recognized as β-Ta_2O_5. The nonstoichiometric Ta_xO_y was formed near the surface. Its density is much lower than the Ta_2O_5 phase (Figure 4.34).

.

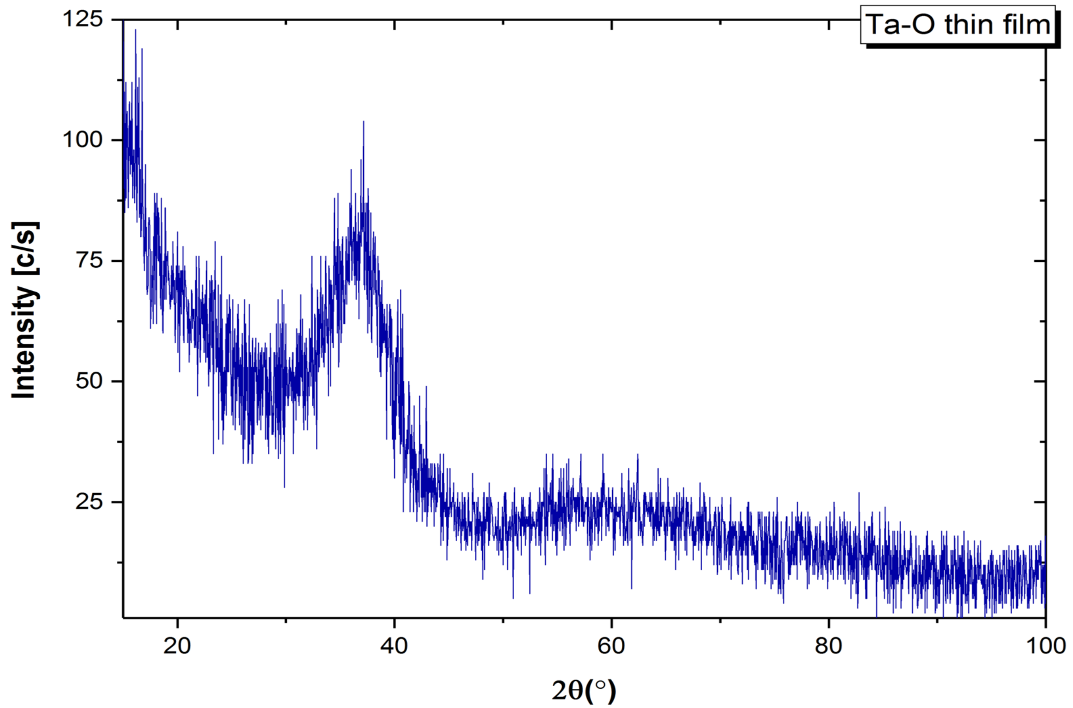

Figure 4.33 Powder diffraction result for Ta-O thin film

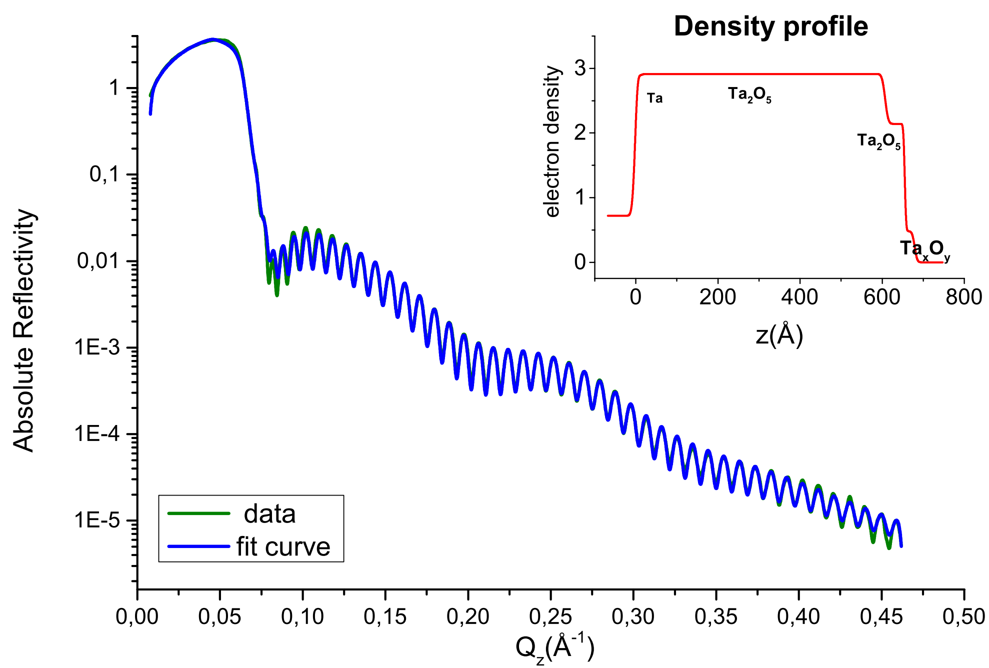

Figure 4.34 Result for XRR data with electron density profile.

	name	Critical wave vector q_c [Å^{-1}]	roughness [Å]	thickness of layers [Å]
substrate	Si	0.0318	6.30	
buffer	Ta	0.0729	4.44	5.76
layer	Ta_2O_5	0.0640	6.06	601.48
	Ta_2O_5	0.0548	2.72	47.73
caplayer	Ta_xO_y	0.0259	4.90	24.17

Table 8 X-ray reflectivity result for Ta-O thin film

4.2.2.2 Electronic structure and surface composition

Lee et al. (4) showed for the first time the vast potential for applications of Ta_2O_{5-x} thin film formed between the Pt electrodes. This material and their work initiated many studies which focused on tantalum oxide as a new, applicable type of material to build devices, especially for resistivity random accesses memories (ReRAM). Hence, as mentioned several times in this thesis, the basis of understanding the resistivity switching phenomena in this type of oxides is their electronic structure. The Ta-O thin film was also thermally reduced in ultra-high vacuum (UHV) up to 900° C. The temperature evolution of Ta4f photoemission line is shown in figure 32. In the spectrum obtained at room temperature the dominating doublet with maxima at 27.0 eV and 27.8eV can be associated to Ta_2O_5. However, a weak contribution of states present between 21-26eV was observed. Those lines are related to a reduced Ta state and can be related to the Ta_xO_y layer determined from the XRR studies. Heating up to 600° C did not show significant changes in reduced Ta state. A doublet which can be ascribed to the metastable state of Ta oxide TaO_x (82) is noticed. In the valence band (Figure 4.36b) region 0-3eV intensity of the in-gap states is increasing. There is no intensity at the Fermi level. The trend begins to change starting from 700° C and the contribution of metallic-like Ta states appears. As mentioned above, the main component of Ta 4f7/2 line is corresponding to Ta_2O. Its binding energy is equal 22.8eV which is slightly higher than that from metallic bulk Ta (21.9eV). With temperature increase up to 900° C the intensity of these lines increases. As suggested by Gnanarajan et al. (82) the Ta $4f_{7/2}$ line with the binding energy of 22.7eV can be attributed to the Ta_2O (Figure 4.35). The presence of reduced Ta states at Ta-O thin film surface is observed also in the valence band (Figure 4.36b).

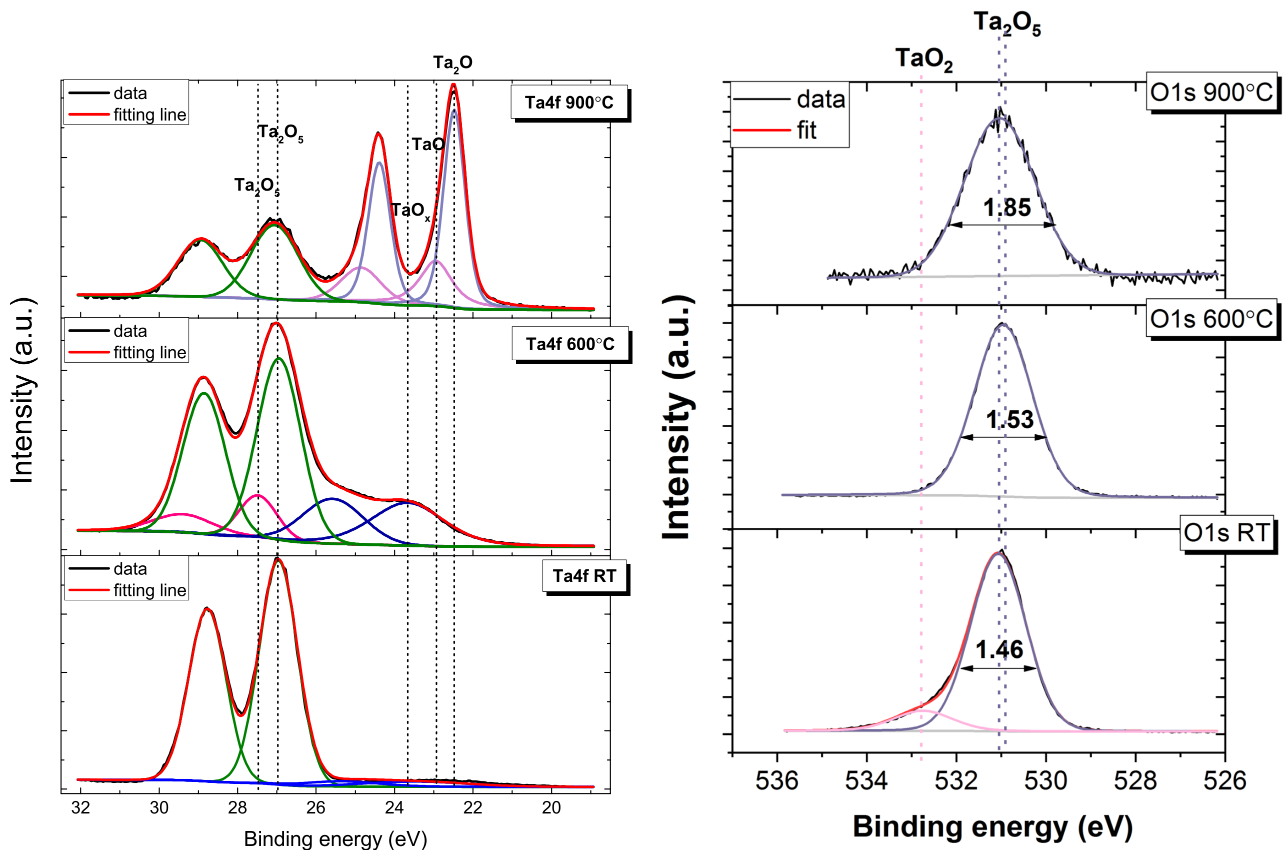

Figure 4.35 Result for Ta4f and O1s line derived from Ta-O thin film after annealing process up to 900°C

The contribution of the reduced Ta electronic states is observed as a broad structure in the region of the original energy gap, with a maximum at about 2eV. The oxygen line also shows a contribution of a different chemical state at an energy of 532.75eV which has a larger value than that reported for pentoxide (530.9 eV) but is near to the binding energy of TaO_2 (186) (Figure 4.35).

A dramatic increase of the reduced tantalum oxide is observed after annealing at 900° C. It is also visible in the valence band region. The certain intensity at the Fermi level is detected which is not related to metallic Ta. The oxygen line is hardly change during annealing. The broadening of the O 1s line is related to the presence of various Ta-O bonding in the reduced film. The O/Ta ratio (Figure 4.36d) determined from the intensities of photoemission lines is close to 2.2 at room temperature at 400° C and quickly drops down to 1.7 at 700° C. An interesting fact is the stabilization of the O/Ta ratio for temperatures higher than 700 °C, in the region where the strongly reduced oxide Ta_2O is forming. Thus, one could expect a greater decrease of oxygen content. This may

be related to two possible reasons. First is the partial oxygen pressure in the XPS analytical chamber which is relatively high during heating and second is crystallization of stoichiometric pentoxide in the layer situated beneath the Ta_2O surface layer (Figure 4.37)

Generally, thermal reduction of the Ta-O film leads to the formation of at least two layer structure of which one can be highly conductive and the second formed by a stable pentoxide.

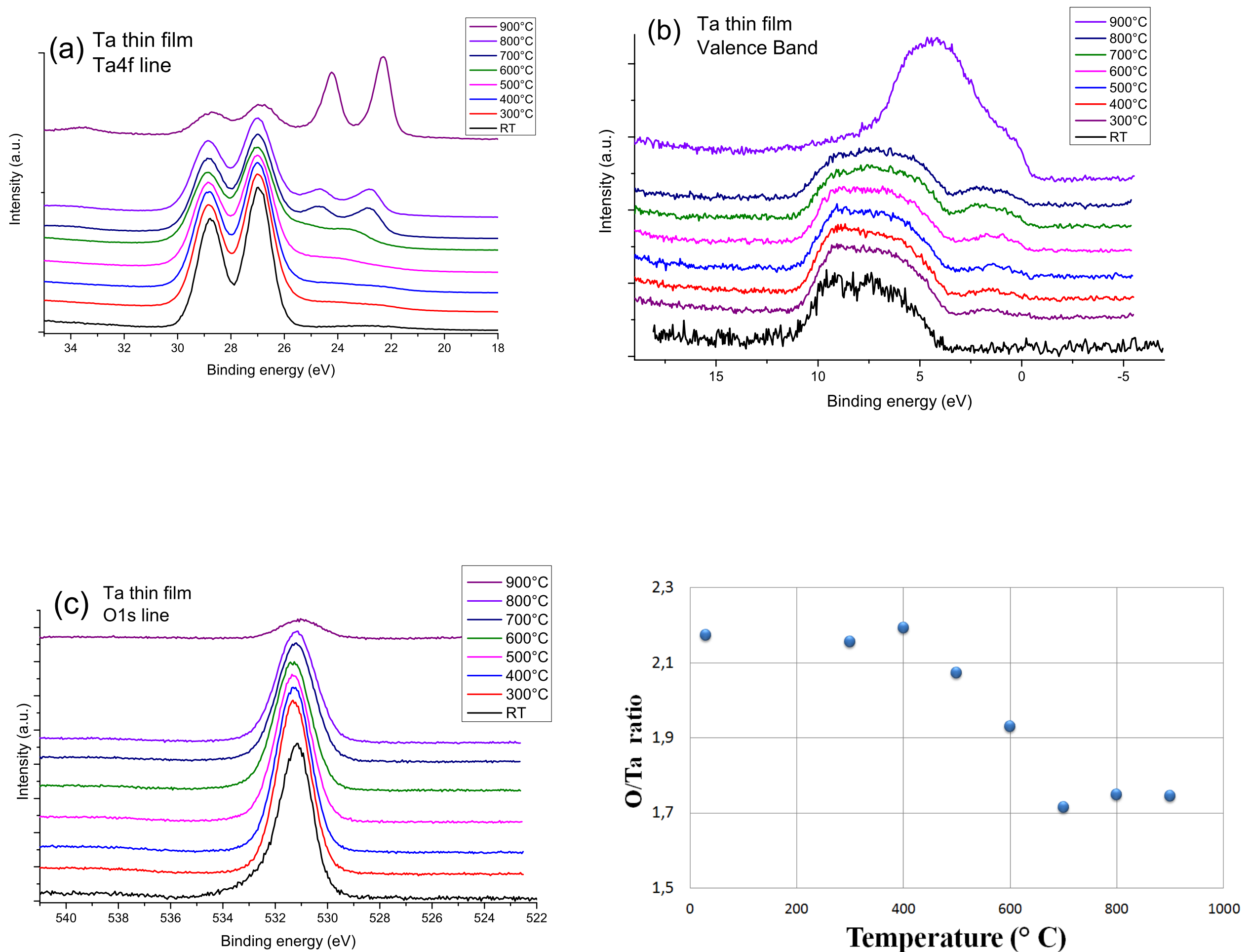

Figure 4.36 Temperature dependence of the photoemission spectra for the Ta-O thin film: (a) Ta4f doublet (b) valence band (c) O1s and (d) oxygen and tantalum ratio derived from XPS spectra

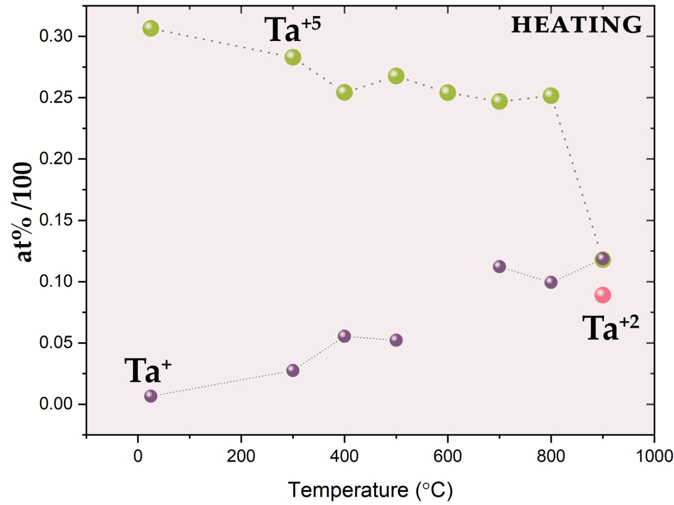

Figure 4.37 Valence ratio as a function of reduction of the Ta-O thin film

4.2.2.3 ToF-SIMS

As in section 4.2.1.3, for precise analysis of the arrangement of ions in the TaxOy thin film the measurements were performed using a Time of Flight Secondary Ion Mass Spectrometer (TOF-SIMS). The assumption is the same as previously; if in the film volume there are present different types of oxides present as a result of measurements in the depth profile mode it can be expected that different secondary ions will be generated from various oxides, and/or that the depth profiles will be different depending on the considered oxide.

The measurements were performed in dual mode using alternation of the bismuth ion beam and the cesium beam as described in the measurement of Nb_2O_5 film. Similarly, the measurements were taken from the 200μm x 200 μm area. The analysis has been divided into two parts; the first is related to the constituent elements of the Ta_xO_y film grown on silicone and the second present contamination. As in the case of the Nb_2O_5 film the analysis is based on analysis of 3D distribution maps and linear depth profiles.

Analysis of the distribution of individual ions in the Ta_xO_y film indicates an inhomogeneous oxide structure similar as in the case of the Nb_2O_5 film. However, some differences can be observed. The 3D representations of distribution of selected ions are collected in Figure 4.38 and Figure 4.39.

As in the case of measurements obtained for Nb_2O_5 performed in positive polarity, for the Ta_xO_y film the distribution of positive ions (see Figure 4.38) indicates a somewhat similar

and simple structure. The Ta^+, TaO^+ and TaO^{2+} ions are uniformly located within the entire volume of the film. Similar, in the case of Nb^{2+} ions here, Ta^{2+} ions are uniform in almost the entire volume, however, do not exist in the near surface area. Whereas $Ta_2O_5^+$ are present on the surface, but the amount of those ions is relatively small.

Measurements made in negative polarity (Figure 4.38) reveal additional information about the oxide structure of the Ta_xO_y film.

Ta^-, TaO^- and TaO_2^- ions have similar, generally uniform distribution within the volume of the film, however, some small deviations from heterogeneity can be seen on the sample surface and at the interface between the silicon substrate and the Ta_xO_y film. Different behavior is exhibited by TaO_3^- and $Ta_2O_4^-$; those ions have been detected in the near-surface region in a the relatively high amount and in a lower amount in the entire film volume. As mentioned before, the distribution of TaO_2^- and $Ta_2O_5^-$ is quite similar, however some additional features were observed within the film volume. Increased intensity of those ions in small regions of sizes of a few micrometers was detected. Such feature extends through the depth of the film creating some kind of channels which are most likely related to inhomogeneity within the 2D structure, which can be directly observed in Figure 4.39 where 2D images are combined. It is worth mentioning, that those regions occur only for those ions, for other ions, the 2D structure indicated homogeneity or inhomogeneity but manifested as the lack of ions in considered areas.

The origin of the presence of such regions is not known, however the similarity of those features to distribution of the silicon substrate may indicate discontinuity of the layer. The distribution of other ions related to surface impurities such as $C_xH_y^-$, K^+, Ca^+, Al^+ and Na^+ can also confirm such a possibility – however since measurements performed in positive and negative polarities were obtained from at different region, a direct correlation cannot be concluded. The last type of inhomogeneous distribution is exhibited by $Ta_2O_3^-$ ions; the ions are present almost throughout the entire volume of the film with the exception of the outermost surface, similar as in the case of distribution of Ta^{2+} ions.

The linear depth profiles (Figure 4.40 and Figure 4.41) summarize the results of studies of the distribution of different ion species in the Ta_xO_y film. Similar to the case of the Nb_2O_5 film, the Ta_xO_y film showed a different distribution of selected ions.

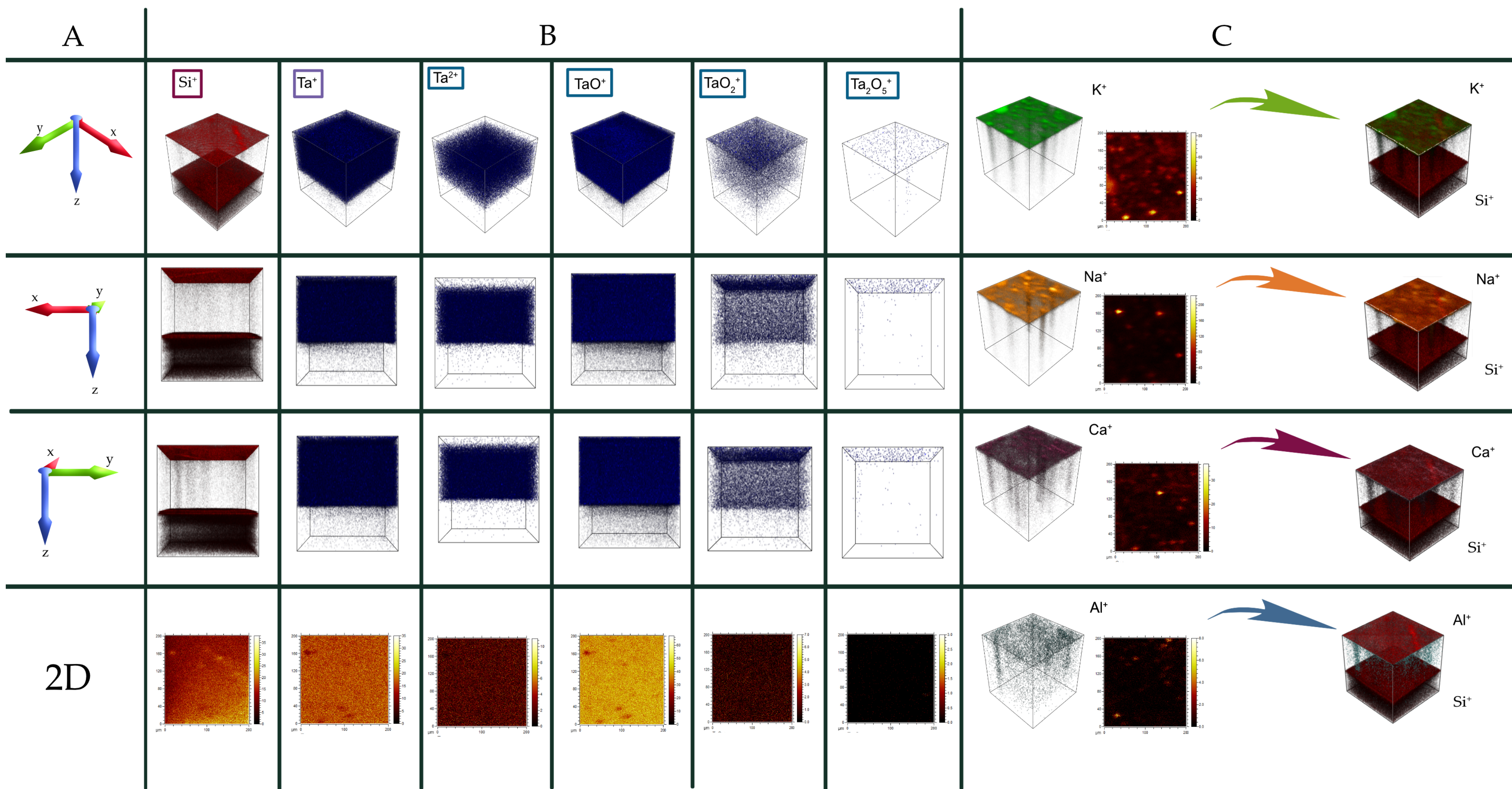

Figure 4.38 Distribution maps for selected ions measured in positive polarity for Ta_2O_5 film grown on Si. The graph represents three main columns: (A) where projection type has been specified, (B) with respective projections of particular ions, (C) 3D overlay of selected ions

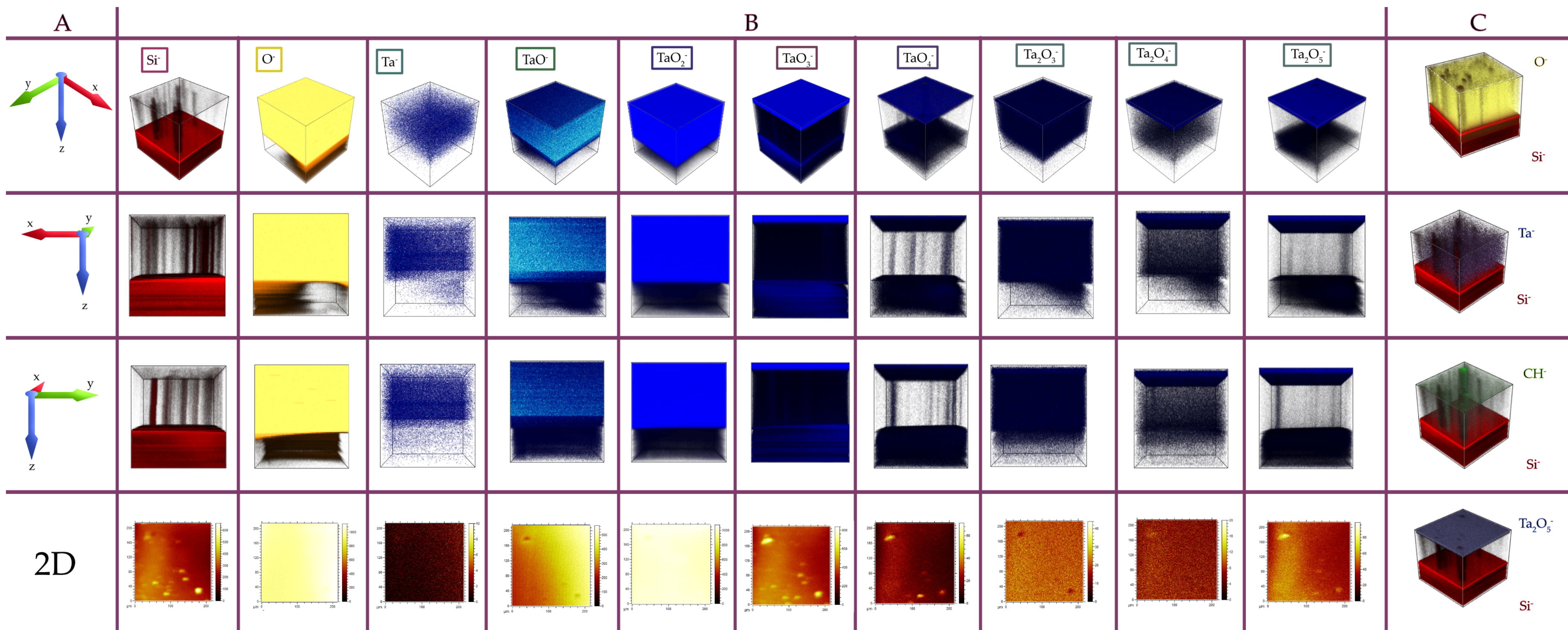

Figure 4.39 Distribution maps for selected ions measured in negative polarity for Ta_2O_5 film grown on Si. The graph represents three main columns: (A) where projection type has been specified, (B) with respective projections of particular ions, (C) 3D overlay of selected ions.

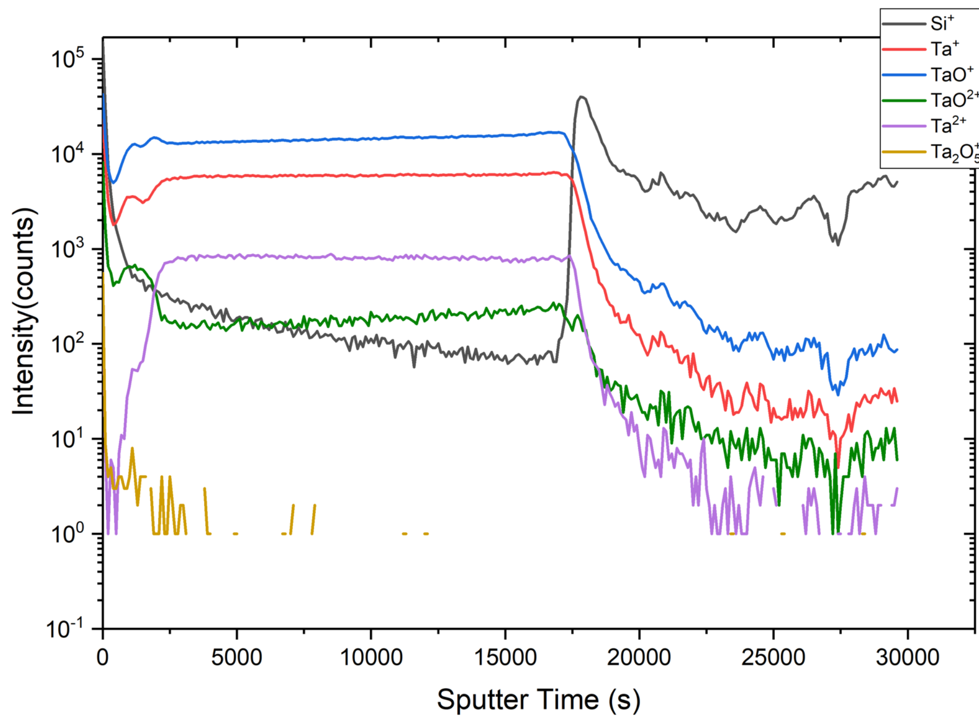

Figure 4.40 Profile obtained from positive polarity for Ta-O thin film

Analysis of the shape of the particular profiles leads to the conclusion that the film consists of one stable layer of oxide – this region appears after the 2500s of sample etching and exists in such form until it reaches silicone.

The sharp changes of the profiles of particular ions at the borders of the regions indicate that there is a well-defined interface; in the case of the silicone interface it is evident that an interface at around 2500s is atypical. The meaning 'atypical' relating to expectation of continuous changes of the oxide structure; here the changes are rather abrupt, the presence of such an interface may indicate the oxygen diffusion limit in the considered Ta_xO_y film. The region near the surface has a more complex structure and can be roughly divided into several sublayers; the presence of local extrema suggests the presence of some chemical interfaces however rather weakly defined in this 0-2000 s region.

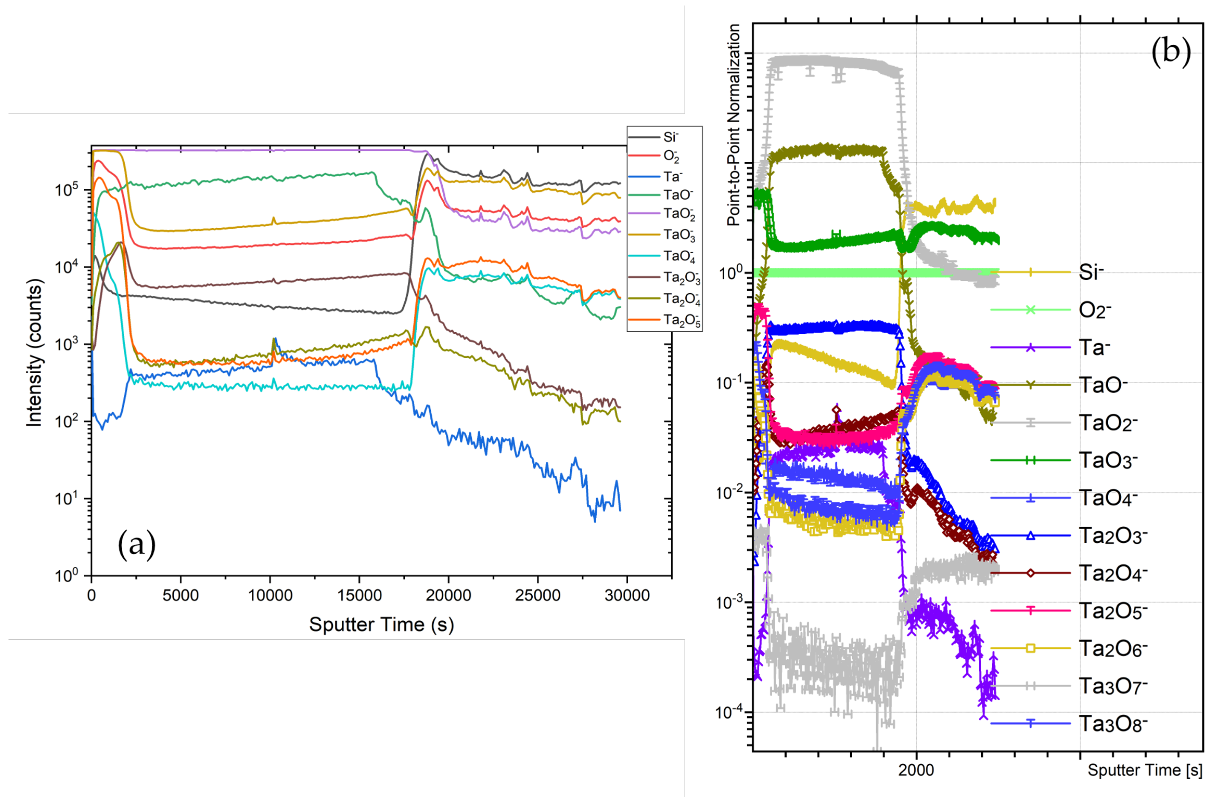

Figure 4.41 Depth profile obtained from *measurements in negative polarity; (a) profile as measured, (b) profile after point by point normalization to the O^{2-} line.*

4.2.2.4 LC-AFM measurements

The thin film was measured in an ultra-high vacuum before and after reduction at temperatures up to 220 °C (Figure 4.42). The measurements were performed at room temperature. The LC-AFM topography and the conductivity were also obtained by using a conducting Pt-Ir-coated tip in contact mode with highest spatial resolution due to the confined potential drop below the contact area of the tip.

The presented results are obtained after reduction of the surface of the film at 220°C for 8 hours. The RMS of the surface increased up to 180° C and then a slight decrease of this factor was observed. The current map shows the effect of switching to the low resistance state, in the middle part of the image an area with increased value of current in the range 0.03 to 1243.4 nA at the bias voltage of 0.05 V is observed. The origin of RS is close to that obtained for Nb-O film. The negatively polarized tip repels oxygen ions which travel further to the surface. The I-V curve obtained at one of the low resistance points showed bipolar character.

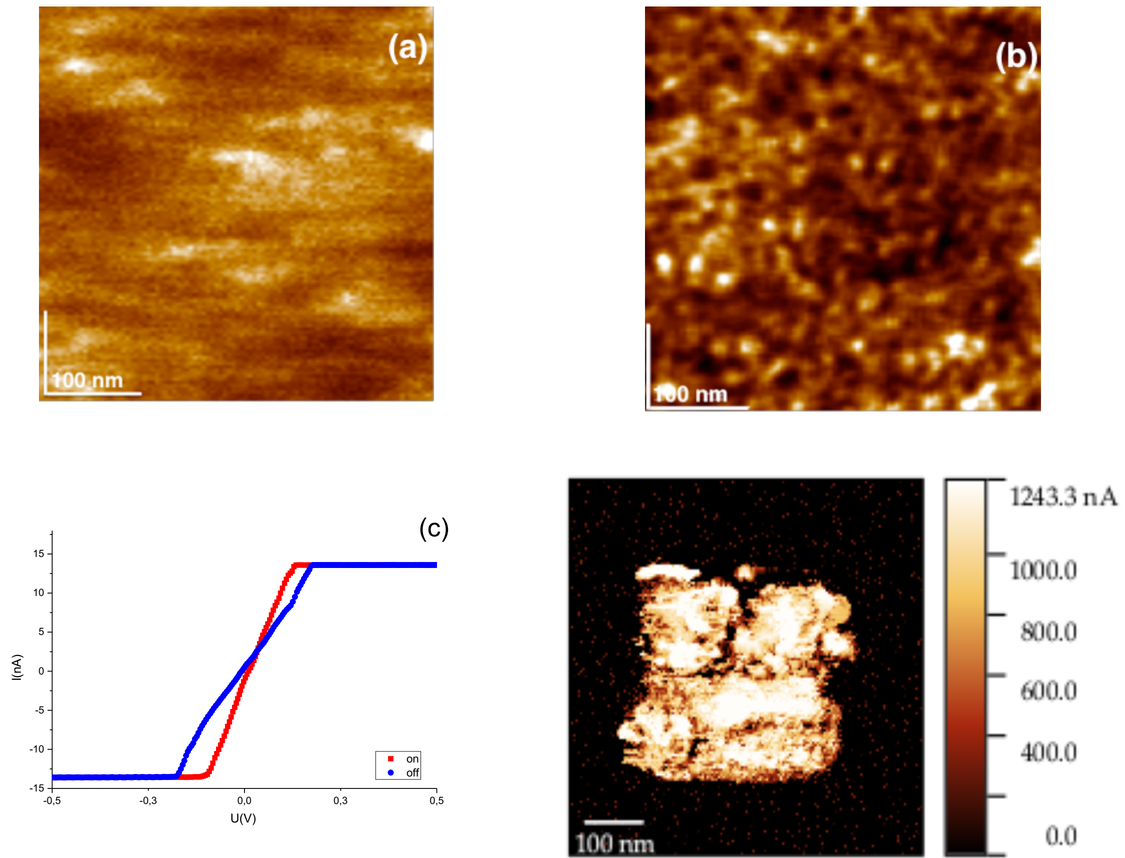

Figure 4.42 AFM topography and local conductivity (LC) maps of the Ta-O film reduced at 220 ℃ for 8 hours; a) AFM contact mode topography with the range up to 1.76 nm; b) LC map obtained with the bias voltage of 2 V, current range was 1.8 to 31.7 nA; c) I-V curve obtained at one of the low resistance points; d) Current map showing in the middle the area switched to the low resistance state, current range 0.03 to 1243.4 nA at the bias voltage of 0.05 V.

5. Conclusions

The main aim of this Ph.D. work was to compare selected physicochemical properties of single crystals Nb_2O_5 with corresponding properties of niobium and tantalum oxides thin films. In particlar, this research work focused on crystal structure, chemical composition of both materials, lattice dynamic and electronic transport phenomena on the nanoscale. Experiments were performed on stoichiometric crystals and thin films under oxidating and reducing condition (25°C -1000°C and 25°C -900°C, respectively).

The Nb_2O_5 single crystal with dimensions of about 0.5cm in diameter and 4.5cm in length was obtained by the zone floating technique. The thin films were obtained by radio frequency sputtering technique where metallic Nb and Ta was deposited on metallic Si substrate and subsequently oxidaized at 300°C in 10^{-4} mbar O_2.

The thesis is divided into two parts: the first focuses on Nb_2O_5 single crystal. The crystal had good quality, and its lattice parameters were measured by X-ray diffraction technique. The type of lattice was monoclinic (P2/m) and described in literature as H-Nb_2O_5 with lattice parameters similar to those in literature. Temperature dependent XRD analysis performed on the powdered sample showed that at oxidation and reducion conditions the crystal structure is stable up to 1000° C. Only anomalous behavior of one unit cell parameter was found.

The electronic structure was analyzed by XPS (in-situ and operando) for core lines and valence band regions. It revealed for the stochiometric crystal the Nb3d doublet showing typical shape and binding energy for the oxidation state 5+ (typical for Nb_2O_5) during annealing in UHV conditions up to 800° C. No in-gap electronic states were detected within the energygap. The reduction started at temperatures between 800°C and 1000° C leading to the partial lowering of the oxidation state from 5+ to 4+. It was clearly identified as an additional component of the Nb3d core line. The analysis of the electronic structure show that the change of the Nb3d line is accompanied by continuum of occupied state in the band gap, which can be classified as a transition of insulating state to metalic state.

XPS measurements also presented that the surface of cleaved crystal was contaminated with physi- and chemisorbants. The physisorbants (OH, H_2O) and chemisorbants (CO,CO_2) were removed at required temperatures of about 800° C.

The studies of lattice dynamics of Nb_2O_5 single crystal by Raman spectroscopy were performed in the air. The results were spectacular and different from those by XRD. The transformation of the origin monoclinic H-Nb_2O_5 into pseudo hexagonal TT- Nb_2O_5 phase was found as a result of analysis of the various possible vibrations within the Nb centered polyhedra. The reason for the discrepancy between the results of a powder diffraction and measurements on single crystal seems to be related to the presence of large number of defects in the pulverized sample (grain size of ca.10μm) which block the structural transformations. Such effect must be taken into account in the temperature dependent structural analysis.

Measurements of the crystal with the use of LC-AFM showed no condcutivity for the as-grown crystal and its inhomogenous increase upon annealing in UHV conditions up to 600 °C. The I-V characteristics found in the better conductive regions (switchable reading area) were related to the changes in the local topography and morphology. This may be an indicator of resistive switching and is connected to local solid-state electrolysis.

The second part of this dissertation focused on Nb-O and Ta-O thin film investigation. It is important to note that I was not able to compare the results to single crystal of Ta_2O_5 in my dissertation as it was not possible to grow a pure single crystal without additional doping.

The XRD analysis of Nb-O and Ta-O shows that the films are amorphous. Their surface roughness was about 0.2 nm and 0.4 nm for Nb-O thin film and Ta-O thin film, respectively. Using XRR measurement and modelling I was able to reveal their hierarchical structure which was partly confirmed by the ToF SIMS depth profiling. In both cases, the full oxidation state of Nb and Ta was found in the layers of the films close to surface although XRR indicates pentoxide with smilar density of electrons even within the bulk of the film of Ta-O system. Additionally, the depth profiling study showed that both amorphous films had impurities like Na, K, Ca and Al with distribution being cluster-like and column-like.

The XPS results showed that for thermal reduction in vacuum of the Nb-O film at temperature as low as 300° C was enough to start the process of Nb valence changes, while for the Ta-O system a strong reduction started at about 600° C. Analyses of Nb and Ta core levels and formation of electronic states within the energy gap confirmed the significant reduction of Nb and Ta electronic state. Also, the LC-AFM studies of the films revealed that the reduction process caused the significant variation of the local

conductivity due to the formation of NbO and Ta_2O on the surface after annealing in-situ at temperatures up to 600 °C. A bipolar type of resistance switching was found for both types of the films.

A much stronger effect of conductivity increase upon thermal reduction in vacuum was observed in both films than in the single crystal of Nb_2O_5. However, the Nb-O film showed the same type of resistivity switching like the Nb_2O_5 crystal.

The results presented in this thesis give a new insight to the problem of chemical and structural instability of niobium and tantalum metal oxides and are related to that property of electrical conductivity which can be locally switched in a controlled way. The detailed studies of physicochemical properties, i.e., electronic structure, crystalline structure, network dynamics in niobium and tantalum pentaoxide, give a broader look at redox processes. Research in nanoscale is particularly important due to the application of thin layers in microelectronics. The thin films seem to be more promising than single crystalline material. The amorphous form of thin films caused the reduction process to be is much easier, and show it is a better candidate to memristor systems. However, further studies of single crystals are necessary to precisely characterize the phenomena in nanoscale. Such studies are necessary to obtain more information on the complex relations between crystallographic details and electronic structure for Nb-O and Ta-O systems. For example, further morphological characterization by HRTEM, EELS, and nanoEDX or other microscopic technique may give broader information about the defects of the crystal and fuller understanding of the mechanism of resistive switching. Following global trends to investigation of Nb-O or Ta-O thin films capped by metals like Pt or Au would be necessary to open the vast applications of these materials to future electronic devices.

Bibliography

1. Hickmott TW. Low-Frequency Negative Resistance in Thin Anodic Oxide Films. J Appl Phys. AIP Publishing; 1962 Sep 1;33(9):2669–82.
2. Beck A, Bednorz JG, Gerber C, Rossel C, Widmer D. Reproducible switching effect in thin oxide films for memory applications. Appl Phys Lett. 2000 Jul 3;77(1):139–41.
3. Szot K, Speier W, Bihlmayer G, Waser R. Switching the electrical resistance of individual dislocations in single-crystalline SrTiO3. Nat Mater. 2006 Mar 26;5(4):312–20.
4. Lee M-J. A fast, high-endurance and scalable non-volatile memory device made from asymmetric Ta2O5-x/TaO2-x bilayer structures. Nature Publishing Group. Nature Publishing Group; 2011 Jul 10;10(8):625–30.
5. Prakash A, Jana D, Maikap S. TaOx-based resistive switching memories: prospective and challenges. Nanoscale Res Lett. Nanoscale Research Letters; 2013 Oct 9;8(1):1–1.
6. E. Cha , J. Woo, D. Lee, J.Song, Y.Koo, J. Lee, Ch. Park, M. Yang and H.Hwang Nanoscale (~10nm) 3D Vertical ReRAM and NbO_2 Threshold Selector with TiN Electrode.2015 IEEE International Elecronic Device Conference Sesion 10 2013 Oct 17;:1–4.
7. Kim S, LIU X, Park J, Jung S, Lee W. Ultrathin (<10nm) Nb_2O5/NbO2 hybrid memory with both memory and selector characteristics for high density 3D vertically stackable RRAM applications. 2012 Symposium on VLSI Technology Digest of Technical Papers. 2012;:155–6.
8. Hickmott TW, Hiatt WR. Electrode effects and bistable switching of amorphous Nb2O5 diodes. Solid-State Electronics. 1970;13(7):1033–47.
9. Sakamoto T, Lister K, Banno N, Hasegawa T, Terabe K, Aono M. Electronic transport in Ta_2O_5 resistive switch. Appl Phys Lett. 2007 Aug 27;91(9):092110–4.
10. Lee K, Kim J, Mok I-S, Na H, Ko D-H, Sohn H, et al. RESET-first unipolar resistance switching behavior in annealed Nb2O5 films. Thin Solid Films. Elsevier B.V; 2014 May 2;558(C):423–9.
11. Wojtyniak M. The Resistivity Switching of Iron Doped Strontium Titanate Single Crystals and Thin Films. 2014. pp. 1–165.
12. Rodenbucher C. Resistive switching phenomena of extended defectsin Nb-doped SrTiO. 2014. pp. 1–223.
13. Dhanaraj G, Byrappa K, Prasad V, Dudley M. Springer Handbook of Crystal Growth. Dhanaraj G, Byrappa K, Prasad V, Dudley M, editors. Berlin, Heidelberg: Springer Science & Business Media; 2010. 1 p.
14. Miracrys. **16** years of serving high-end industries with high-quality products www.miracrys.com/CCinit.php.
15. Ko EI, Weissman JG. Structures of niobium pentoxide and their implications on chemical behavior. Catalysis Today. 1990;8(1):27–36.
16. Jurisch M, Eichler S, Bruder M. 9 - Vertical Bridgman Growth of Binary Compound Semiconductors. Second Edition. Handbook of Crystal Growth. Elsevier B.V; 2014. 42 p.
17. Dabkowska H.A., Dabkowski A.B. (2010) Crystal Growth of Oxides by Optical Floating Zone Technique. In: Dhanaraj G., Byrappa K., Prasad V., Dudley M. (eds) Springer Handbook of Crystal Growth. Springer Handbooks. Springer, Berlin, Heidelberg
18. Dąbkowska HA, Dabkowski AB, Hermann R, Priede J, Gerbeth G. 8 - Floating Zone

Growth of Oxides and Metallic Alloys. Second Edition. Handbook of Crystal Growth. Elsevier B.V; 2014. 49 p.

19. Bunshah RF. Handbook of Deposition Technologies for Films and Coatings. William Andrew; 1994. 1 p.
20. Schmelzer S. Ultra Thin Oxide Films for Dielectric and ResistiveMemory Applications. 2013. pp. 1–143.
21. Usha KS, Sivakumar R, Sanjeeviraja C, Sathe V, Ganesan V, Wang TY. Improved electrochromic performance of a radio frequency magnetron sputtered NiO thin film with high optical switching speed. RSC Adv. Royal Society of Chemistry; 2016 Aug 22;6:79668–80.
22. Wisniak J. Charles Hatchett: The discoverer of niobium. Educación Química. 2015 Oct;26(4):346–55.
23. Griffith WP, Morris PJT. Charles Hatchett FRS (1765-1847), chemist and discoverer of niobium. Notes and Records of the Royal Society. 2003 Sep 22;57(3):299–316.
24. Bach D. EELS of Nb oxides and Nb-based capacitorsEELS of Nb oxides and Nb-based capacitors. 2009. pp. 1–210.
25. Franchy R, Bartke TU, Gassmann P. The interaction of oxygen with Nb (110) at 300, 80 and 20 K. Journal of Solid State Chemistry. 1996 Oct;366(1):60–70.
26. Graham J, Thornber MR. The Crystal Chemistry of Complex Niobium and Tantalum Oxides l. Structural Classification of MO_2 Phases. American Mineralogist. 1974;59:1026–39.
27. Niebuhr J. Die niederen Oxide des Niobs. Journal of Solid State Chemistry. 1966 Sep;11(3):191–203.
28. Rao C, Rama Rao G, Subba Rao GV. Semiconductor-Metal Transitions in NbO_2 and $Nb_{1-x}V_xO_2$. Journal of Solid State Chemistry.
29. Rao CNR, Rao GVS. Transition metal oxides. 0AD. 135 p.
30. Hulm JK, Jones CK, Hein RA, Gibson JW. Superconductivity in the TiO and NbO systems. J Low Temp Phys. Kluwer Academic Publishers-Plenum Publishers; 1972 May;7(3-4):291–307.
31. Okaz AM, Keesom PH. Specific heat and magnetization of the superconducting monoxides: NbO and TiO. Phys Rev B. American Physical Society; 1975 Dec 1;12(11):4917–28.
32. Delheusy M. X-ray investigation of Nb/O interfaces. 2008. pp. 1–191.
33. Becker R, Hartwig H, Köppe H, Vanecek H, Velić P, Warncke R, et al. Gmelin Handbuch der Anorganischen Chemie. Warncke R, editor. Berlin, Heidelberg: Springer Science & Business Media; 2013. 1 p.
34. ADLER D. Mechanisms for Metal-Nonmental Transitions in Transition-Metal Oxides and Sulfides. Rev Mod Phys. American Physical Society; 1968 Oct 1;40(4):714–36.
35. Halbritter J. On the oxidation and on the superconductivity of niobium. Applied Physics A. Springer-Verlag; 1987;43(1):1–28.
36. Nowak I, Ziolek M. Niobium Compounds: Preparation, Characterization, and Application in Heterogeneous Catalysis. Chem Rev. 1999 Dec;99(12):3603–24.
37. Kato K. Structure refinement of H-Nb_2O_5. Acta Crystallogr B Struct Crystallogr Cryst Chem. International Union of Crystallography; 1976 Mar 15;32(3):764–7.
38. Shindo I, Komatsu H. Growth of H-Nb_2O_5 Single crystals by the floating zone method. J Cryst Growth. 1975 Dec 31;34(1):152–3.
39. Ko EI, Weissman JG. Structures of niobium pentoxide and their implications on chemical behavior. Catalysis Today. 1989 Dec 31;8(1):27–36.
40. Zibrov IP, Filonenko VP, Sundberg M, Werner PE. Structures and phase transitions of B-Ta_2O_5 and Z-Ta_2O_5: two high-pressure forms of Ta_2O_5. Acta Cryst (2000) B56, 659-665 .
41. Kurmaev EZ, Moewes A, Bureev OG, Nekrasov IA, Cherkashenko VM, Korotin MA, et al. Electronic structure of niobium oxides. Journal of Alloys and Compounds. 2002.

42. Reznichenko LA, Akhnazarova VV, Shilkina LA, Razumovskaya ON, Dudkina SI. Invar effect in n-Nb_2O_5, α_{ht}-Nb_2O_5, and L-Nb_2O_5. Crystallogr Rep. 2009 May 17;54(3):483–91.
43. Soerensen OT. Nonstoichiometric Oxides. Academic Press 1981.
44. Iijima S. Direct observation of lattice defects in H-Nb2O5 by high resolution electron microscopy. Acta Cryst (1973) A29, 18-24 .
45. Norin R, Carlsson M, Elgquist B. NOTE ON CRYSTAL STRUCTURES OF NB11O27 NB25O62 AND H-NB2O5. Vol. 20. Acta Chemica …; 1966. 2 p.
46. Tamura S. High-pressure phase research on Nb2O5. J Mater Sci. Kluwer Academic Publishers; 1972;7(3):298–302.
47. Kato K, Tamura S. Die Kristallstructure von T-Nb_2O_5. Acta Crystallogr B Struct Crystallogr Cryst Chem. 1975;31:673.
48. Tamura S, Kato K, Goto M. Single crystals of T-Nb2O5 obtained by slow cooling method under high pressures. Zeitschrift für anorganische und allgemeine Chemie. WILEY-VCH Verlag; 1974 Dec 1;410(3):313–5.
49. Rohrer FE, Larsson AK. Twinning and defects in N-Nb2O5. Acta Cryst (2000) B56, 780-784 .
50. Nico C, Monteiro T, Graça MPF. Niobium oxides and niobates physical properties: Review and prospects. JOURNAL OF PROGRESS IN MATERIALS SCIENCE. Elsevier Ltd; 2016 Jul 1;80(C):1–37.
51. Grundner M, Halbritter J. XPS and AES studies on oxide growth and oxide coatings on niobium. J Appl Phys. 1980;51(1):397–10.
52. ANDERSSON S, Wadsley AD. Crystallographic Shear and Diffusion Paths in Certain Higher Oxides of Niobium, Tungsten, Molybdenum and Titanium. Nature. Nature Publishing Group; 1966 Aug 1;211(5049):581–3.
53. McConnell AA, Aderson JS, A CRSAP, 1976. Raman spectra of niobium oxides. Journal of Solid State Chemistry . 1976 Jan;32(5):1067–76.
54. Schäfer H, Gruehn R, Schulte F. Die Modifikationen des Niobpentoxids. Angew Chem. Wiley-Blackwell; 1966 Jan 7;78(1):28–41.
55. Erbudak M, Gubarov VA, Kurmaev EZ. The electronic structure of NbO: Theory and experiment. Journal of Physics and Chemistry of Solids. 1978.
56. Weibin Z, Weidong W, Xueming W, Xinlu C, Dawei Y, Changle S, et al. The investigation of NbO 2and Nb 2O 5electronic structure by XPS, UPS and first principles methods. Surf Interface Anal. 2013 Feb 28;45(8):1206–10.
57. Pérez-Walton S, Valencia-Balvín C, Dalpian GM, Osorio-Guillén JM. Electronic, dielectric, and optical properties of the B phase of niobium pentoxide and tantalum pentoxide by first-principles calculations. Phys Status Solidi B. 2013 Apr 17;250(8):1644–50.
58. Weeks M. The discovery of the elements. VII. Columbium, tantalum, and vanadium. ACS Publications.
59. Knepper RA. Thermomechanical behavior and microstructure evolution of tantalum thin films during the beta-alpha phase transformation. 2007.
60. Janish MT, Kotula PG, Boyce BL, Carter CB. Observations of fcc and hcp tantalum. J Mater Sci. 2015;50:3706–15.
61. Khanuja M, Sharma H, Mehta BR, Shivaprasad SM. XPS depth-profile of the suboxide distribution at the native oxide/Ta interface. Journal of Electron Spectroscopy and Related Phenomena. 2009 Jan;169(1):41–5.
62. Lee SL, Cipollo M, Windover D, Rickard C. Analysis of magnetron-sputtered tantalum coatings versus electrochemically deposited tantalum from molten salt. Surface & Coatings Technology. 1999 Nov;120-121:44–52.
63. Robin A. Corrosion behavior of niobium, tantalum and their alloys in boiling sulfuric acid solutions. International Journal of Refractory Metals and Hard Materials. 1997 Jan;15(5-6):317–23.

64. Robin A, Rosa JL. Corrosion behavior of niobium, tantalum and their alloys in hot hydrochloric and phosphoric acid solutions. International Journal of Refractory Metals and Hard Materials. 2000 Jan;18(1):13–21.
65. Garg SP, Krishnamurthy N, Awasthi A, Venkatraman M. The O-Ta (Oxygen-Tantalum) system. JPE. Springer-Verlag; 1996;17(1):63–77.
66. Muraoka Y, Fujimoto Y, Kameoka M, Matsuura Y, Sunagawa M, Terashima K, et al. Preparation of TaO2 thin films using NbO2 template layers by a pulsed laser deposition technique. Thin Solid Films. Elsevier B.V; 2016 Jan 29;599(C):125–32.
67. Le Gallic M, Roussel H, Rapenne L, Audier M, Barnes J-P. Particular structural defects in Ta2O5 from crystallisation of amorphous thin films in O2â€"H2O atmosphere. Acta Mater. Acta Materialia Inc; 2015 Aug 1;94(C):181–92.
68. Andreoni W, Pignedoli CA. Ta2O5 polymorphs: Structural motifs and dielectric constant from first principles . Appl Phys Lett. 2010;96(6):062901–4.
69. Pérez-Walton S, Valencia-Balvín C, Padilha ACM, Dalpian GM, Osorio-Guillén JM. A search for the ground state structure and the phase stability of tantalum pentoxide. J Phys: Condens Matter. 2016 Jan 26;28(3):035801–1.
70. Stephenson NC, Roth RS. Structural systematics in the binary system Ta2O5-WO3. V. The structure of the low-temperature form of tantalum oxide L-Ta2O5. Acta Cryst (1971) B27, 1037-1044
71. Terao N. Structure des Oxydes de Niobium: Transformation de Structure du Nb2O5-γ en Nb2O5-α et la Formation du NbO2. Jpn J Appl Phys. IOP Publishing; 1965 Jan 1;4(1):8–15.
72. Laves F, Petter W, Wulf H. Die Kristallstruktur von ?-Nb2O5. Naturwissenschaften. 1964;51(24):633–4.
73. Hummel HU, Fackler R, Remmert P. Tantaloxide durch Gasphasenhydrolyse, Druckhydrolyse und Transportreaktion aus 2H-TaS2: Synthesen von TT-Ta2O5 und T-Ta2O5 und Kristallstruktur von T-Ta2O5. Chemische Berichte. WILEY-VCH Verlag; 1992 Mar 1;125(3):551–6.
74. Fukumoto A, Miwa K. Prediction of hexagonal Ta2O5structure by first-principles calculations. Phys Rev B. 1997 May 1;55(17):11155–60.
75. Lee S-H, Kim J, Kim S-J, Kim S, Park G-S. Hidden Structural Order in Orthorhombic Ta2O5. Phys Rev Lett. 2013 Jun 5;110(23):235502–5.
76. Ramprasad R. First principles study of oxygen vacancy defects in tantalum pentoxide. J Appl Phys. 2003;94(9):5609–5.
77. Aleshina LA, Loginova SV. Rietveld analysis of X-ray diffraction pattern from β-Ta2O5 oxide. Crystallogr Rep. Nauka/Interperiodica; 2002;47(3):415–9.
78. Terao N. Structure des Oxides de Tantale. Jpn J Appl Phys. IOP Publishing; 1967 Jan;6(1):21–34.
79. Rahaman SZ, Maikap S, Tien T-C, Lee H-Y, Chen W-S, Chen FT, et al. Excellent resistive memory characteristics and switching mechanism using a Ti nanolayer at the Cu/TaOx interface. Journal of Biological Material Research. ??? 2012 Jun 26;7(1):1–1.
80. Yoo HK, Lee SB, Lee JS, Chang SH, Yoon MJ, Kim YS, et al. Conversion from unipolar to bipolar resistance switching by inserting Ta[sub 2]O[sub 5] layer in Pt/TaO[sub x]/Pt cells. Appl Phys Lett. 2011;98(18):183507–4.
81. Xiao B, Watanabe S. Oxygen vacancy effects on an amorphous-TaOx-based resistance switch: a first principles study. Nanoscale. Royal Society of Chemistry; 2014 Aug 6;6:10169–78.
82. Gnanarajan S, Lam SKH. Evolution of epitaxial Ta[sub 2]O[sub 5] and Ta[sub 2]O films during thermal oxidation of epitaxial tantalum films on sapphire substrates. J Vac Sci Technol A. 2008;26(3):494–5.

83. Ivanov MV, Perevalov TV, Aliev VS, Gritsenko VA, Kaichev VV. Electronic structure of δ-Ta2O5 with oxygen vacancy: ab initio calculations and comparison with experiment. J Appl Phys. 2011;110(2):024115–6.
84. Perevalov TV, Shaposhnikov AV. Ab initio simulation of the electronic structure of Ta2O5 crystal modifications. J Exp Theor Phys. 2013 Jul 26;116(6):995–1001.
85. Zacherle T, Schmidt PC, Martin M. Atomic and Electronic Structure of Oxides. In: Daniele Ielmini, Waser R, editors. Resistive Switching From Fundamentals of Nanoionic Redox Processes to Memristive Device Applications. Weinheim, Germany: Wiley-VCH Verlag GmbH & Co. KGaA; 2016. pp. 49–94.
86. Zhu L, Zhou J, Guo Z, Sun Z. Realization of a reversible switching in TaO2 polymorphs via Peierls distortion for resistance random access memory. Appl Phys Lett. 2015 Mar 2;106(9):091903.
87. Kofstad P. Defects and transport properties of metal oxides. Oxid Met. Kluwer Academic Publishers-Plenum Publishers; 1995;44(1-2):3–27.
88. Gregori G. Defect Structure of Metal Oxides. In: Ielmini D, Waser R, editors. Resistive Switching [Internet]. first. Weinheim, Germany: Wiley-VCH Verlag GmbH & Co. KGaA; 2016. pp. 95–124. (From Fundamentals of Nanoionic Redox Processes to Memristive Device Applications).
89. He X, Li X, Gao X, Yu W, Yang R, Liu X, et al. Reversible resistance switching properties in Ti-doped polycrystalline Ta2O5 thin films. Applied Physics A. 2012 Mar 29;108(1):177–83.
90. Guo Y, Robertson J. Comparison of oxygen vacancy defects in crystalline and amorphous Ta_2O_5. Microelectronic Engineering. Elsevier B.V; 2015 Nov 1;147(C):254–9.
91. Roth RS, Waring JL, Brower WS. Effect of Oxide Additions on the Polymorphism of Tantalum Pentoxide II. IIStabilizationll of the High Temperature Structure Type. Journal of RESEARCH of the National Bureau of Standards - APhysics and Chemistry. 1970;74A(4):477–83.
92. Kofstad P. Studies of electrical conductivity of Nb_2O_5 as a function of oxygen pressure at 600–1200°C. Journal of Physics and Chemistry of Solids. 1962;23(11):1571–8.
93. Nimmo KM, Anderson JS. Reduction and non-stoicheiometry of niobium pentoxide. J Chem Soc, Dalton Trans. 1972;(21):2328–12.
94. Anderson JS, Browne JM, Cheetham AK, Dreele Von R. Point defects and extended defects in niobium oxides. Nature. 1973;243(5402):81–3.
95. Hutchison JL, Anderson JS. The direct correlation between lattice fringes and atomic positions in defect structures in N-niobium oxide. Phys Status Solidi A. WILEY-VCH Verlag; 1972 Jan 16;9(1):207–13.
96. Michaelis A. Valve Metal, Si and Ceramic Oxides as Dielectric Films for Passive and Active Electronic Devices. Electrochemical Surface Modification Thin Films, Functionalization and Characterization. Weinheim, Germany: Advances in Electrochemical Sciences and Engineering; Chapter 1, 2008. pp. 1–106..
97. Iijima S, Kimura S, Goto M. High-resolution microscopy of nonstoichiometric $Nb_{22}O_{54}$ crystals: point defects and structural defects. Acta Crystallogr Sect A Cryst Phys Diffr Theor Gen Crystallogr. International Union of Crystallography; 1974 Mar 1;30(2):251–7.
98. Collaboration: Authors and editors of the volumes III/17G-41D. Nb_2O_5: defect and transport properties. In: Non-Tetrahedrally Bonded Binary Compounds II. Berlin/Heidelberg: Springer-Verlag; 2000. pp. 1–13. (Landolt-Börnstein - Group III Condensed Matter; vol. 41D).
99. Roberson JA, Rapp RA. Electrical properties of NbO and NbO_2. Journal of Physics and Chemistry of Solids. 1969;30(5):1119–24.
100. Belanger G, Destry J, Perluzzo G, Raccah PM. Electron Transport in Single Crystals of Niobium Dioxide. Canadian Journal of Physics. 1974 Nov 15;52(22):2272–80.

101. Slesazeck S, Mähne H, Wylezich H, Wachowiak A, Radhakrishnan J, Ascoli A, et al. Physical model of threshold switching in NbO_2 based memristors. RSC Adv. Royal Society of Chemistry; 2015 Nov 27;5:102318–22.
102. Stroud JE, Tripp WC, WIMMER JM. Defect Structure of Ta2O5. J American Ceramic Society. Wiley/Blackwell (10.1111); 1974 Apr 1;57(4):172–5.
103. Landolt-Börnstein, Condensed Matter: Ta2O5: transport properties and non-stoichiometry. 2001 May 20;41D(III):1–8.
104. Li H, Gao B, Chen Z, Zhao Y, Huang P, Ye H, et al. A learnable parallel processing architecture towards unity of memory and computing. Sci Rep. Nature Publishing Group; 2015 Aug 7;:1–8.
105. Waser R, Dittmann R, Staikov G, Szot K. Redox-Based Resistive Switching Memories - Nanoionic Mechanisms, Prospects, and Challenges. Maier J, Kern K, editors. Adv Mater. 2009 Jul 13;21(25-26):2632–63.
106. Rogala M, Klusek Z, Rodenbücher C, Waser R, Szot K. Quasi-two-dimensional conducting layer on TiO_2 (110) introduced by sputtering as a template for resistive switching. Appl Phys Lett. 2013;102(13):131604–5.
107. Szot K, Rogala M, Speier W, Klusek Z, Besmehn A, Waser R. TiO 2—a prototypical memristive material. Nanotechnology. 2011 May 16;22(25):254001–22.
108. Sawa A. Resistive switching in transition metal oxides. Materials Today. Elsevier Ltd; 2008 Jun 15;11(6):28–36.
109. Lee AR, Baek GH, Kim TY, Ko WB, Yang SM, Kim J, et al. Memory window engineering of Ta2O5−x oxide-based resistive switches via incorporation of various insulating frames. Sci Rep. Nature Publishing Group; 2016 Jul 15;:1–9.
110. Koza JA, He Z, Miller AS, Switzer JA. Resistance Switching in Electrodeposited VO_2 Thin Films. Chem Mater. 2011 Sep 27;23(18):4105–8.
111. Yan X, Li Y, Zhao J, Xia Y, Zhang M, Liu Z. Resistive switching model change induced by electroforming in α-Fe_2O_3 films. Physics Letters A. Elsevier B.V; 2015 Oct 9;379(38):2392–5.
112. Szot K, Dittmann R, Speier W, Waser R. Nanoscale resistive switching in $SrTiO_3$ thin films. Phys Status Solidi RRL. 2007 Mar;1(2):R86–8.
113. Lee JS, Lee S, Noh TW. Resistive switching phenomena: A review of statistical physics approaches. Appl Phys Rev. 2015 Aug 31;2(3):031303–58.
114. Heo Y, Kan D, Shimakawa Y, Seidel J. Resistive switching properties of epitaxial $BaTiO_3$; thin films tuned by after-growth oxygen cooling pressure. Physical Chemistry Chemical Physics. Royal Society of Chemistry; 2015 Dec 15;18:197–204.
115. Xu Z-T, Jin K-J, Gu L, Jin Y-L, Ge C, Wang C, et al. Evidence for a Crucial Role Played by Oxygen Vacancies in LaMnO3 Resistive Switching Memories. Small. 2012 Feb 20;8(8):1279–84.
116. Waser R, Daniele Ielmini, Akinaga H, Shima H, Wong HSP, Yang JJ, et al. Introduction to Nanoionic Elements for Information Technology. In: Ielmini D, Waser R, editors. Resistive Switching. First Edition. 2016. pp. 1–30.
117. Ielmini D, Waser R. Resistive Switching. Ielmini D, Waser R, editors. Weinheim, Germany: John Wiley & Sons; 2015. 1 p.
118. Chang T-C, Chang K-C, Tsai T-M, Chu T-J, Sze SM. Resistance random access memory. Materials Today. Elsevier Ltd; 2016 Jun 1;19(5):254–64.
119. Jung K, Kim Y, Jung W, Im H, Park B, Hong J, et al. Electrically induced conducting nanochannels in an amorphous resistive switching niobium oxide film. Appl Phys Lett. 2010;97(23):233509–3.
120. Bae J, Hwang I, Jeong Y, Kang S-O, Hong S, Son J, et al. Coexistence of bi-stable memory and mono-stable threshold resistance switching phenomena in amorphous NbO_x films. Appl Phys Lett. 2012;100(6):062902–5.
121. Kim J, Jung K, Kim Y, Jo Y, Cho S, Woo H, et al. Switching Power Universality in Unipolar Resistive Switching Memories. Sci Rep. Nature Publishing Group; 2016 Mar 23;:1–10.

122. Jung K, Kim Y, Im H, Kim H, Park B. Leakage Transport in the High-resistance State of a Resistive-switching NbO_x Thin Film Prepared by Pulsed Laser Deposition. J Korean Phys Soc. 2011 Oct 14;59(4):2778.

123. Chen L, Sun Q-Q, Gu J-J, Xu Y, Ding S-J, Zhang DW. Bipolar resistive switching characteristics of atomic layer deposited Nb2O5 thin films for nonvolatile memory application. Current Applied Physics. Elsevier B.V; 2011 May 1;11(3):849–52.

124. Hanzig F, Mähne H, Veselý J, Wylezich H, Slesazeck S, Leuteritz A, et al. Effect of the stoichiometry of niobium oxide on the resistive switching of Nb2O5 based metal-insulator-metal stacks. Journal of Electron Spectroscopy and Related Phenomena. Elsevier B.V; 2015 Apr 27;:1–26.

125. Persano A, Quaranta F, Martucci MC, Cretì P, Siciliano P, Cola A. Transport and charging mechanisms in Ta2O5 thin films for capacitive RF MEMS switches application. J Appl Phys. 2010 Jun;107(11):114502–7.

126. Persano A, Quaranta F, Cola A, Taurino A, De Angelis G, Marcelli R, et al. Ta2O5 Thin Films for Capacitive RF MEMS Switches. Journal of Sensors. 2010;2010(9):1–5.

127. Tsuruoka T, Terabe K, Hasegawa T, Aono M. Forming and switching mechanisms of a cation-migration-based oxide resistive memory. Nanotechnology. 2010 Sep 24;21(42):425205–9.

128. Tsuruoka T, Hasegawa T, Terabe K, Aono M. Conductance quantization and synaptic behavior in a Ta2O5-based atomic switch. Nanotechnology. 2012 Oct 11;23(43):435705–7.

129. Jiang H, Stewart DA. Enhanced oxygen vacancy diffusion in Ta_2O_5 resistive memory devices due to infinitely adaptive crystal structure. J Appl Phys. 2016 Apr 6;119(13):134502–7.

130. Yang Y, Sheridan P, Lu W. Complementary resistive switching in tantalum oxide-based resistive memory devices. Appl Phys Lett. 2012;100(20):203112–5.

131. Breuer T, Nielen L, Roesgen B, Waser R, Rana V, Linn E. Realization of Minimum and Maximum Gate Function in Ta_2O_5-based Memristive Devices. Sci Rep. Nature Publishing Group; 2016 Mar 25;:1–9.

132. Kavehei O, Linn E, Nielen L, Tappertzhofen S, Skafidas E, Valov I, et al. An associative capacitive network based on nanoscale complementary resistive switches for memory-intensive computing. Nanoscale. 2013;5(11):5119–10.

133. Cristea D, Crisan A, Cretu N, Borges J, Lopes C, Cunha L, et al. Structure dependent resistivity and dielectric characteristics of tantalum oxynitride thin films produced by magnetron sputtering. Applied Surface Science. Elsevier B.V; 2015 Nov 1;354:298–305.

134. Jeong DS, Thomas R, Katiyar RS, Scott JF, Kohlstedt H, Petraru A, et al. Emerging memories: resistive switching mechanisms and current status. Rep Prog Phys. 2012 Jun 28;75(7):076502–32.

135. Jeon H, Park J, Jang W, Kim H, Kang C, Song H, et al. Resistive switching of a TaO_x/TaON double layer via ionic control of carrier tunneling. Appl Phys Lett. 2014 Apr 14;104(15):151603–6.

136. Na S-C, Kim J-J, Chul Chun M, Hee Jin D, Ahn S-E, Soo Kang B. Mechanism of the reset process in bipolar-resistance-switching Ta/TaO_x/Pt capacitors based on observation of the capacitance and resistance. Appl Phys Lett. 2014 Mar 24;104(12):123503–5.

137. Pan Y, Cai Y, Liu Y, Fang Y, Yu M, Tan S, et al. Microscopic origin of read current noise in TaOx-based resistive switching memory by ultra-low temperature measurement. Appl Phys Lett. 2016 Apr 11;108(15):153504–6.

138. Yang JJ, Zhang MX, Strachan JP, Miao F, Pickett MD, Kelley RD, et al. High switching endurance in TaOx memristive devices. Appl Phys Lett. 2010 Dec 6;97(23):232102.

139. Zhou Q, Zhai J. Resistive switching characteristics of Pt/TaO_x/HfN_x structure and its performance improvement. AIP Advances. 2013;3(3):032102–13.

140. Gu T, Tada T, Watanabe S. Conductive Path Formation in the Ta_2O_5 Atomic Switch: First-Principles Analyses. ACS Nano. 2010 Nov 23;4(11):6477–82.
141. Ohno T, Samukawa S. Ta 2O 5-based redox memory formed by neutral beam oxidation. Jpn J Appl Phys. 2016 Apr 7;55(6S1):06GJ01–4.
142. Zhu L, Zhou J, Guo Z, Sun Z. An overview of materials issues in resistive random access memory. Journal of Materiomics. Elsevier Ltd; 2015 Dec 1;1(4):285–95.
143. Chen C, Song C, Yang J, Zeng F, Pan F. Oxygen migration induced resistive switching effect and its thermal stability in W/TaO_x/Pt structure. Appl Phys Lett. 2012;100(25):253509–5.
144. Kurnia F, Hadiyawarman, Jung CU, Jung R, Liu C. Composition dependence of unipolar resistance switching in TaOx thin films. Phys Status Solidi RRL. 2011 Jun 14;5(7):253–5.
145. Dong-Wook K, Dongjae C, Sungjoo L, Jaewook J, Ilsin A. Bipolar resistive switching characteristics of Cu/TaO_x/Pt structures. J Korean Phys Soc. 2010 Mar 15;56(3):846–5.
146. Park G-S, Kim YB, Park SY, Li X-S, Heo S, Lee M-J, et al. In situ observation of filamentary conducting channels in an asymmetric Ta_2O_{5-x}/TaO_{2-x} bilayer structure. Nature Communications. 2012 Dec 31;4:2382–2.
147. Kim J, Mok I-S, Kim Y, Lee K, Ko D-H, Sohn H. Effect of chemical bonding states in TaO_X base layers on rectifying bipolar resistive switching characteristics. J Vac Sci Technol B. 2013 May;31(3):032206–6.
148. Moulder JF, Strickle WF, Sobol PE, Bomben KD. Handbook of X-ray Photoelectron Spectroscopy. Chastain J, King RC Jr, editors. Physical Electronic, Inc; 1995. 1 p.
149. Balin K. Reaction of Europium and Some Transition Metals Deposited as Ultrathin Films. 2011.
150. Daillant J, Gibaud A. X-ray and Neutron Reflectivity. Daillant J, Gibaud A, editors. Vol. 770. Berlin, Heidelberg: Springer; 2008. 1 p.
151. Py M. Study of interfaces and nanometric structures by ToF-SIMS : upon a spatially resolved quantitative analysis. Université de Grenoble; 2011.
152. Kasap S, Capper P. Springer Handbook of Electronic and Photonic Materials. Springer; 2017. 1 p.
153. Gibaud A. Specular Reflectivity from Smooth and Rough Surfaces. In: Daillant J, Gibaud A, editors. X-ray and Neutron Reflectivity. Berlin, Heidelberg: Springer, Berlin, Heidelberg; 1999. pp. 87–120. (Lecture Notes in Physics Monographs; vol. 58).
154. Yasaka M. X-ray thin-film measurement techniques. The Rigaku Journal. John Wiley & Sons; 2000;26(2):1–9.
155. Hrouzek M. Modélisation, estimation et contrôle de Microscope á Force Atomique. 2007.
156. Butler HJ, Ashton L, Bird B, Cinque G, Curtis K, Dorney J, et al. Using Raman spectroscopy to characterize biological materials. Nature Protocols. Nature Publishing Group; 2016 Mar 10;11(4):664–87.
157. Benninghoven A, Hagenhoff B, Werner HW. Secondary Ion Mass Spectrometry. Wiley; 1997. 1 p.
158. Wilson RG, Stevie FA, Magee CW. Secondary ion mass spectrometry. Wiley-Interscience; 1989. 1 p.
159. Kim Y-P, Shon HK, Shin SK, Lee TG. Probing nanoparticles and nanoparticle-conjugated biomolecules using time-of-flight secondary ion mass spectrometry. Mass Spec Rev. John Wiley & Sons, Ltd; 2014 Jun 2;34(2):237–47.
160. Qi S, Zuo R, Liu Y, Wang Y. Synthesis and photocatalytic activity of electrospun niobium oxide nanofibers. Materials Research Bulletin. Elsevier Ltd; 2013 Mar 1;48(3):1213–7.

161. Pilarek B, Pelczarska AJ, Szczygieł I. Characterization of niobium(v) oxide received from different sources. Journal of Thermal Analysis and Calorimetry. Springer Netherlands; 2017 Mar 18;:1–7.
162. Bish DL, Howard SA. Quantitative Phase Analysis Using the Rietveld Method. Journal of Applied Crystallography. International Union of Crystallography (IUCr); 1988 Apr 1;21(2):86–91.
163. Lüdtke TC. Metastable transition metal oxides, oxide nitrides, and nitrides. 2017. pp. 1–232.
164. Kroumova E, Aroyo MI, Perez-Mato JM, Kirov A, Capillas C, Ivantchev S, et al. Bilbao Crystallographic Server : Useful Databases and Tools for Phase-Transition Studies. Phase Transitions. 2003 Jan;76(1-2):155–70.
165. McConnell AA, Aderson JS, Rao CNR. Raman spectra of niobium oxides. Spectrochemica Acta. 1976 Jan;32A(5):1067–76.
166. Hardcastle FD, Wachs IE. Determination of niobium-oxygen bond distances and bond orders by Raman spectroscopy. Solid State Ionics. 1991 Apr;45(3-4):201–13.
167. Jehng J-M, Wachs IE. The molecular structures and reactivity of supported niobium oxide catalysts. Catalysis Today. 1990 Oct;8(1):37–55.
168. Bhide V, Husson E, Gasperin M. Etude de niobates de structure GTB par absorption infra-rouge et diffusion raman. Materials Research Bulletin. 1980 Sep;15(9):1339–44.
169. Aronne A, Sigaev VN, Champagnon B, Fanelli E, Califano V, Usmanova LZ, et al. The origin of nanostructuring in potassium niobiosilicate glasses by Raman and FTIR spectroscopy. Journal of Non-Crystalline Solids. 2005 Nov;351(46-48):3610–8.
170. Balachandran U, Eror NG. Raman spectrum of the high temperature form of Nb_2O_5. J Mater Sci Lett. Kluwer Academic Publishers; 1982 Sep;1(9):374–6.
171. Pauling LC. The Nature of the Chemical Bond and the Structure of Molecules and Crystals and Intr. to Modern Structural Chemistry. Cornell University Press, Ithaca, New York; 1960.
172. Kato K, IUCr. Structure refinement of H-Nb_2O_5. Acta Crystallogr B Struct Crystallogr Cryst Chem. International Union of Crystallography; 1976 Mar 15;32(3):764–7.
173. Ozdanova J, Ticha H, Tichy L. Raman studies and some physical properties of selected (PbO)x(Nb2O5)y(TeO2)1−x−y glasses. Optical Materials. Elsevier B.V; 2010 Jul 1;32(9):950–5.
174. Chemistry GBJOSS, 1973. Vibrational spectra of yttrium niobate and tantalate. Journal of Solid State Chemistry. 1973 Jun;7(2):169–71.
175. Jehng J-M, Wachs IE. Structural chemistry and Raman spectra of niobium oxides. Chem Mater. 1991 Jan;3(1):100–7.
176. Gatehouse BM, Wadsley AD. The crystal structure of the high temperature form of niobium pentoxide. Acta Cryst (1964) Q17, 1545-1554 .
177. Herval LKS, Dreifus von D, Rabelo AC, Rodrigues AD, Pereira EC, Gobato YG, et al. The role of defects on the structural and magnetic properties of Nb_2O_5. Journal of Alloys and Compounds. Elsevier B.V; 2015 Dec 25;653(C):358–62.
178. Balkanski M, Wallis RF, Haro E. Anharmonic effects in light scattering due to optical phonons in silicon. Phys Rev B. American Physical Society; 1983 Aug 15;28(4):1928–34.
179. Ikeya T, Senna M. Change in the structure of niobium pentoxide due to mechanical and thermal treatments. Journal of Non-Crystalline Solids. 1988 Nov;105(3):243–50.
180. Xie S, Iglesia E, Bell AT. Effects of Temperature on the Raman Spectra and Dispersed Oxides. J Phys Chem B. 2001 Jun;105(22):5144–52.
181. Pittman RM, Bell AT, 1993. Raman studies of the structure of niobium oxide/titanium oxide (Nb_2O_5/ TiO_2). Journal of Physical Chemistry. 1993;97:12178–85.

182. Aleshina LA, Malinenko VP, Phouphanov AD. The short-range order of anodic amorphous oxide films of Ta and Nb. Journal of Non-Crystalline Solids. 1986 Nov;87(3):350–60.
183. Kalampounias AG, Papatheodorou GN, Yannopoulos SN. A temperature dependence Raman study of the 0.1Nb2O5–0.9TeO2 glass-forming system. Journal of Physics and Chemistry of Solids. 2006 Apr;67(4):725–31.
184. Yannopoulos SN, Kalampounias AG, Chrissanthopoulos A, Papatheodorou GN. Temperature induced changes on the structure and the dynamics of the "tetrahedral" glasses and melts of ZnCl2 and ZnBr2. J Chem Phys. 2003 Feb 15;118(7):3197–214.
185. NIST Standard Reference Database 20, Version 4.1 Available from: https://srdata.nist.gov/xps/Default.aspx
186. Naumkin AV, Kraut-Vass A, Powell CJ, Gaarenstroom SW. NIST X-ray Photoelectron Spectroscopy Database. 2012.
187. Kuznetsov MV, Razinkin AS, Shalaeva EV. Photoelectron spectroscopy and diffraction of surface nanoscale NbO/Nb(110) structures. J Struct Chem. Springer US; 2009;50(3):514–21.
188. Nowak A, Persson J, Schmelzer B, Szade J, Szot K. Low temperature reduction in Ta–O and Nb–O thin films. J Phys D: Appl Phys. 2014 Mar 10;47(13):135301–10.
189. Xu H, Jiang Y, Fan X, Wang Y, Liu G. Growth and dielectric properties of Ta_2O_5 single crystal by the floating zone method. Cryst Res Technol. 2012 Jun 20.
190. Terao N. Structures des Oxydes de Niobium. Jpn J Appl Phys. IOP Publishing; 1963 Mar 1;2(3):156–74.
191. Terao N. Structure des Oxides de Tantale. Jpn J Appl Phys. IOP Publishing; 1967 Jan 1;6(1):21–34.
192. Kofstad P. On The Defect Structure of Ta_2O_5. J Electrochem Soc. The Electrochemical Society; 1962 Sep 1;109(9):776–81.